EVIDENCE FOR $e^+e^- \to \gamma\eta_c(1S)$ AT CENTER-OF-MASS ENERGIES BETWEEN 4.01 AND 4.60 GEV AT BESIII

Manuel Lara

Submitted to the faculty of the University Graduate School
in partial fulfillment of the requirements
for the degree
Doctor of Philosophy
in the Department of Physics,
Indiana University
July 2016

Accepted by the Graduate Faculty, Indiana University, in partial fulfillment of the requirements for the degree of Doctor of Philosophy.

Doctoral Committee

Matthew Shepherd, Ph.D

Ryan Mitchell, Ph.D

Adam Szczepaniak, Ph.D

Chen-Yu Liu, Ph.D

June 30, 2016

Manuel Lara

Evidence for $e^+e^- \to \gamma\eta_c(1S)$ at center-of-mass energies between 4.01 and 4.60 GeV at BESIII

This dissertation shows the first evidence of the process $e^+e^- \to \gamma\eta_c(1S)$ using data collected by the BESIII experiment operating at BEPCII. This process can be used as a probe to study the nature of recently discovered charmonium-like Y states between 4.0 and 4.6 GeV, including the $Y(4260)$ and $Y(4360)$. Data collected at six center-of-mass energies are analyzed, namely: 4.01, 4.23, 4.26, 4.36, 4.42, and 4.60 GeV, corresponding to a total integrated luminosity of 4.6 fb^{-1}. We measure the Born cross section, $\sigma_E(e^+e^- \to \gamma\eta_c(1S))$, at each energy using a combination of twelve $\eta_c(1S)$ decay channels. Because the significance of the signal is marginal at each energy ($\leq 3.0\sigma$), we also combine all six energies under various assumptions for the energy-dependence of the cross section. If a $Y(4260)$ is assumed, we measure $\sigma_{4.26}(e^+e^- \to \gamma\eta_c(1S)) = 2.11 \pm 0.49(\text{stat.}) \pm 0.33(\text{syst.})$ pb with a significance of 4.2σ. With our current statistics we are unable to distinguish the $Y(4260)$ process from others.

Matthew Shepherd, Ph.D

Ryan Mitchell, Ph.D

Adam Szczepaniak, Ph.D

Chen-Yu Liu, Ph.D

Contents

List of Tables

List of Figures

Chapter 1

Motivation

The field of charmonium spectroscopy is concerned with discovering or predicting mass states composed of charm-anticharm ($c\bar{c}$) quark pairs. The rest mass energy of the charm quark is about 1000 times that of the ubiquitous up or down quarks which make up the familiar proton and neutron. The discovery of the spin triplet $c\bar{c}$ meson called the J/ψ by Samuel Ting and Burton Richter in 1974 was a monumental moment in particle physics. That year the first radial excitation of the J/ψ, or $\psi(2S)$, was discovered by Burton Richter's SLAC group. These discoveries contributed to the eventual acceptance of quarks as real particles as opposed to some mathematical construct. Despite over thirty years of study the field of charmonium is still rich with many surprises.

Tens of unexpected particles have been discovered with properties unlike conventional charmonia at similar energies. Collectively these resonances are known as the "XYZ" [29]. Some may represent a new class of exotic particles composed of four quarks. Further efforts by both theorists and experimentalists in addition to more data is expected to shed further light on the nature of the XYZ. [1].

In collisions of e^+e^- their annihilation proceeds via an intermediate virtual photon with well-constrained quantum numbers $J^{PC} = 1^{--}$. The resulting resonance must have an odd spatial parity or, by the relation $P = (-1)^{L+1}$, have 0 or even orbital angular momentum. The mass spectrum of predicted and unpredicted charmonium states are shown in Figure 1.1. The yellow boxes represent charmonium states predicted by theory and confirmed by experiment. The grey boxes represent the charmonium states predicted but not yet discovered. The red boxes are discovered charmonium-like states whose nature is still unknown. Above 4 GeV only the $\psi(4040)$, $\psi(4160)$, and $\psi(4415)$ states were both predicted and discovered.

In addition to the conventional vector charmonium states at center-of-mass energies between 4.0-4.6 GeV, recent measurements at e^+e^- collider facilities [20, 50] report observations of charmonium-like states that appear supernumerary. The $Y(4260)$ was the first vector charmonium-like state discovered. By analyzing events where an electron or positron radiate a photon and annihilate at center of mass energies around 4260 MeV the BaBar experiment observed an enhancement in $\pi\pi J/\psi$ [20], see Figure 1.2. The $Y(4260)$ was soon confirmed by the Belle experiment using the same

---

[1] XYZ refers to a wide range of detected particles that were not predicted. The meaning of the labels are as follows: Y - vector states with $J^{PC} = 1^{--}$, Z - charged quarkonium-like states, X - particles that don't follow a Y or Z label. It should be noted that the Particle Data Group lists all XYZ particles simply as X.

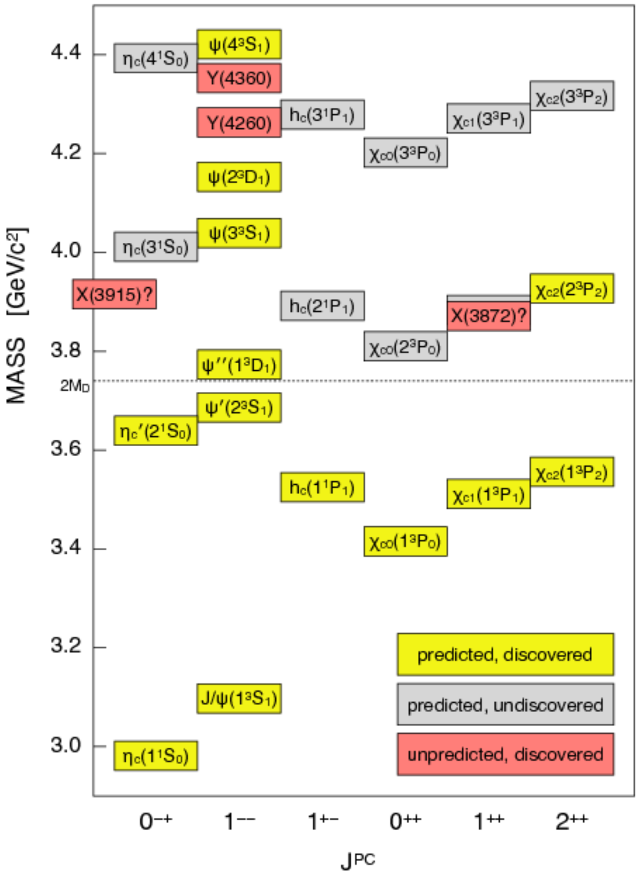

Figure 1.1: The mass spectrum of predicted and unpredicted charmonium states. The yellow boxes represent charmonium states predicted by theory and confirmed by experiment. The grey boxes represent the charmonium states predicted but not yet discovered. The red boxes are discovered charmonium-like states whose nature is still unknown. The DD open-charm threshold at 3.73 GeV is also shown. The figure is taken from a presentation by R. Mitchell [54].

initial state radiation (ISR) technique employed by BaBar [50]. Another enhancement around 4360 MeV in $\pi\pi\psi(2S)$ decays was also discovered by BaBar and confirmed by Belle [21, 60], see Figure 1.3. Other decay channels of $Y(4260)$ or $Y(4360)$ are lacking, which make it difficult to constrain the range of theories proposed to explain their nature.

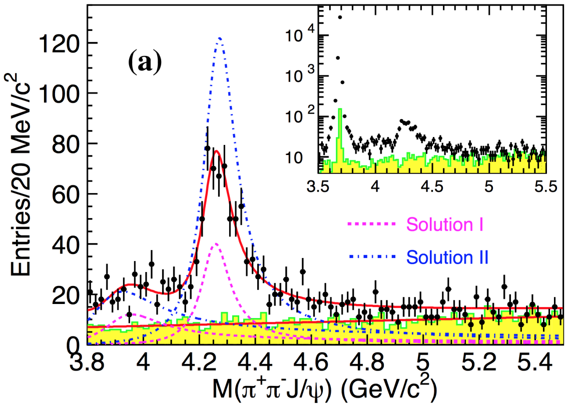

Figure 1.2: From [50], the $\pi^+\pi^-J/\psi$ invariant mass at energies between 3.8-5.6 GeV reported by the Belle collaboration.

Radiative transitions of quarkonium allow for a distinct experimental signature due to the monochromatic transition photon. In addition, it offers a sensitive way to probe the internal dynamics. Radiative transitions involving a flip in the spin of the quarkonium constituent quarks are suppressed by the inverse-square of the quark mass and are called M1 transitions. In the case of a vector meson ($J^{PC} = 1^{--}$), the quark spins are aligned with no relative angular momentum. Therefore, final states with

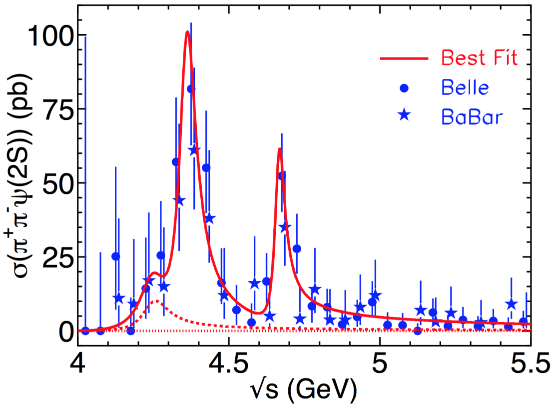

Figure 1.3: From [51], the $\pi^+\pi^-\psi(2S)$ cross section at energies between 4.0-5.5 GeV as measured by the BaBar and Belle Collaborations in stars and solid circles, respectively. The solid curve is the best fit to both experiments data with three coherent Breit-Wigners: the $Y(4260)$, $Y(4360)$, and $Y(4660)$. The dashed curve is the $Y(4260)$ signal shape.

quark spins anti-aligned are suppressed. This explains why conventional ψ states like $\psi(2S)$ decay to $\gamma\chi_{c0}(1P)$ about 30 times more often than $\gamma\eta_c(1S)$. In stark contrast, interpretations of the $Y(4260)$ as a meson coupled with a constituent gluon or hybrid meson predict $\gamma\eta_c(1S)$ decay rates to be enhanced relative to $\gamma\chi_{c0}(1P)$ by a factor of 2 [38]. Unfortunately, only a weak $e^+e^- \to \gamma\chi_{c0}$ signal was measured between 4.0-4.6 GeV [14] and at 4.23 GeV the significance of the χ_{c0} signal was 0σ.

We report evidence for $e^+e^- \to \gamma\eta_c(1S)$ using data collected by the BESIII collaboration at center-of-mass energies: 4.01, 4.23, 4.26, 4.36, 4.42, and 4.60 GeV. We reconstruct $\eta_c(1S)$ in twelve decay channels: $\pi^+\pi^+\pi^-\pi^-\pi^0\pi^0$, $\pi^+\pi^-\pi^0\pi^0$, $\pi^+\pi^+\pi^-\pi^-\eta$, $K^+K^-\pi^+\pi^-\pi^0$, $\pi^+\pi^+\pi^+\pi^-\pi^-\pi^-$, $\pi^+\pi^+\pi^-\pi^-$, $\pi^+\pi^-\eta$, $K^\pm K_S\pi^\mp\pi^+\pi^-$, $K^\pm K_S\pi^\mp$, $K^+K^-\pi^0$, $K^+K^-\pi^+\pi^-$, and $K^+K^-\pi^+\pi^+\pi^-\pi^-$. These are the strongest well-established decay modes of the $\eta_c(1S)$ reported by the Particle Data Group (PDG) [56]. While we do not find evidence for this process at any individual energy, the significance is consistently above 3σ when we combine all of our datasets according to the assumption that the energy-dependence of the cross section follows a $Y(4260)$, $Y(4360)$, or a constant. With our current statistics, we cannot make firm conclusions about the energy-dependence of the cross section. However, we note that the cross section is better explained by a $Y(4260)$ than by conventional charmonium states: $\psi(4040)$, $\psi(4160)$, and $\psi(4420)$, where the states are described by a Breit-Wigner with a mass and width fixed to the world average values given in the PDG [56].

In this dissertation we present an analysis of $e^+e^- \to \gamma\eta_c(1S)$ which is decomposed into 10 chapters. In Chapter 2, an introduction of the Standard Model is presented with focus on Quantum Chromodynamics (QCD) and Quantum Electrodynamics (QED). In addition, an overview of charmonium spectroscopy and the role radiative transitions play in understanding the quark dynamics of quarkonium follows. We also discuss properties and interpretations of the $Y(4260)$ and $Y(4360)$. The chapter ends by examining contributions from conventional and non-resonant processes to the production of $\gamma\eta_c(1S)$ in electron positron annihilation.

Chapter 3 introduces the BEPCII accelerator, which is capable of colliding electrons and positrons at center-of-mass energies between 2.8-4.6 GeV. The BESIII collaboration performed a scan from electron-positron annihilation at energies between 4.01-4.60 GeV. The design and construction of the BESIII spectrometer with focus on tracking, particle identification, and calorimetry is discussed. In addition, an overview of the BESIII trigger and data acquisition is also presented.

Chapter 4 presents an overview of the BESIII Offline Software System (BOSS), which enables the reconstruction of charged and neutral particles. A discussion of the MC packages specific to this analysis is also included.

Chapter 5 provides a discussion of statistical techniques with emphasis on data modeling, likelihood fitting, figure of merit and hypothesis testing.

Chapter 6 discusses more broadly the derivation of the cross section in e^+e^- collisions from theoretical and experimental perspectives.

The analysis, results, and study of systematic errors of this work are presented in Chapters 7-9. Ch. 7 details the data processing steps taken to select candidate $e^+e^- \to \gamma\eta_c(1S)$ events in a channel-dependent manner. This is achieved with the modeling of signal and background MC as discussed in the chapter. The background ISR processes are also discussed at the end of the chapter. The results of the analysis are presented in Ch. 8. A study of the systematic error associated with this measurement is discussed in Ch. 9.

Chapter 10 ends by concluding that while we observe evidence for $e^+e^- \to \gamma\eta_c(1S)$ at 4.23 and 4.26 GeV we are unable to distinguish among the possible production mechanisms and therefore cannot claim unambiguous evidence of $Y(4260)$ to $\gamma\eta_c(1S)$.

Chapter 2

Theoretical Background

The fundamental building blocks of matter in the universe are fermions, point-like particles with half integer spin. Four fundamental forces govern the interaction between fermions via mediator particles known as gauge bosons. The Standard Model is a theoretical framework that unifies all particle interactions with three of the four forces, namely: the electromagnetic force, the weak force, and the strong force. While the Standard Model is known to be an incomplete theory of all forces, its predictions have been consistently validated. A notable validation of the theory is the discovery of the Higgs boson [2, 32], the first spin 0 fundamental particle that gives mass to all matter.

In the framework of the Standard Model the electromagnetic, weak, and strong forces are mediated by particles with integer spin. Their interactions are described by a gauge theory. The electromagnetic force is mediated by a photon; the weak force is mediated by the $W^{\pm}$ and Z^0; and the strong force is mediated by eight gluons.

Fermions can be further classified into color and non-color species called quarks and leptons, respectively. An important property of the strong force is that the potential energy between color charged particles increases linearly with distance; the implication being that color particles generate enough energy at sufficient distance to produce other color particles. Color confinement is the phenomenon that a color charged particle (such as a quark) cannot exist in isolation, and therefore cannot be directly observable. In this way quarks clump together to form hadrons. The most common subset of hadrons are mesons and baryons which are made up of quark pairs or triplets, respectively. Gluons, being the mediator of color, also cannot be directly observed.

2.1 Standard Model

In the Standard Model (SM) there are six quarks and leptons each grouped into three pairs called generations [58], see Table 2.1. All stable matter belongs to the first generation with each subsequent generation heavier than the previous, with the possible exception of the neutrinos. For every particle there is an anti-particle with the same mass but opposite electric charge and handedness denoted with a bar. A proton, for instance, is composed of up (u) up (u) and down (d) quarks denoted uud, while an anti-proton is composed of anti-up ($\bar{u}$) anti-up ($\bar{u}$) and anti-down ($\bar{d}$) quarks denoted $\bar{u}\bar{u}\bar{d}$. The electron, muon and tau all carry the same unit of electron charge while quarks carry fractional electron charge.

2.1.1 Classification

The six quarks can be combined in pairs or triplets to make mesons or baryons, respectively. More generally, any particles composed of quarks are called hadrons. It is these hadrons that are ultimately measured by a detector. The multitude of meson and baryon states can be classified according to a set of quantum numbers. In this section we limit our discussion to mesons.

A particularly useful set of quantum numbers to describe properties of a particle are J^{PC}. The total angular momentum (J) is the vector sum of angular momentum (L) and total spin (S). If a meson is composed of identical quarks ($q\bar{q}$) then the interchange of the quarks is known as spatial parity (P). The spatial parity is the product of the constituent quark parities and $(-1)^L$. The intrinsic parities of a quark and anti-quark are opposite, therefore, $P = (-(-1)^L)$. In addition to the spatial parity quantum number a $q\bar{q}$ meson can also undergo charge parity, C. Flipping the charge of flavor neutral mesons like $c\bar{c}$ does not change the particle species making charge conjugation a valid quantum number. For such flavor neutral states the charge parity is $C = (-1)^{L+S}$. Nomenclature borrowed from atomic physics alternatively describes mesons in terms of the radial energy level of the system (n), the orbital angular momentum (L), and the total spin (S). In spectroscopic notation this would be expressed as $n^{2S+1}L_J$.

Each quark, except u and d, carry a flavor based on their type. A charm quark, for instance, carries charm (C) flavor. Similarly, there are quarks with flavors: strangeness (S), bottomness (B'), and topness (T). These flavors assign to each hadron an integer value whose convention is that flavor charge and the electric charge of a quarks have the same sign. In this way any flavor of a charged meson has the same sign as its charge. Hypercharge (Y) is a quantum number related to the strong interaction and is defined as

$$Y = S + C + B' + T + B$$

where B is the baryon number defined as $\frac{1}{3}(n_q - n_{\bar{q}})$, where n_q is the number of quarks and $n_{\bar{q}}$ is the number of antiquarks. The close mass of the u and d quarks hint at a symmetry called isospin. From the perspective of isospin, the u and d quarks are the same particle in two states. Through a rotation in isospin a u quark can be turned into a d quark. The isospin of the u and d is 1/2 with different projections onto the z-axis (I_z). Isospin is an approximate symmetry due to the degenerate mass of the u and d quarks. In strong interactions flavor is conserved but violated in weak interactions.

If we restrict ourselves to the four lightest quarks (u, d, s, and c) Figure 2.1 reveals a rich map of possible pseudoscalar ($J^P = 0^-$) and vector ($J^P = 1^-$) meson states. The three planes are separated by the charm (C) quantum number so that the middle plane is made up of particles with $C = 0$. This includes $c\bar{c}$ mesons which contain "hidden" charm. The flavor neutral mesons composed of $q\bar{q}$ quarks pairs can be seen huddled in the center of the middle plane of Figure 2.1.

Fermions	Name	Symbol	Spin	EM charge	Color charge	Mass (MeV/c^2)
Lepton	Electron	e	1/2	-1	0	0.511
	Muons	μ	1/2	-1	0	105.7
	Tau	τ	1/2	-1	0	1,777
	Electron Neutrino	ν_e	1/2	0	0	< 0.0000022
	Muon Neutrino	ν_μ	1/2	0	0	< 0.170
	Tau Neutrino	ν_τ	1/2	0	0	< 15.5
Quarks	up	u	1/2	+2/3	RGB	1.5-3.3
	charm	c	1/2	+2/3	RGB	1,160-1,340
	top	t	1/2	+2/3	RGB	169,100-173,300
	down	d	1/2	-1/3	RGB	3.5-6.0
	strange	s	1/2	-1/3	RGB	70-130
	bottom	b	1/2	-1/3	RGB	4,130-4,370

Table 2.1: Properties of quarks and leptons.

2.1.2 Quantum Chromodynamics

Quantum Chromodynamics (QCD) is a subset of the Standard Model that deals exclusively with the strong force. In QCD, color is transferred between quarks via gluons. Quarks carry color charge denoted RGB for red, green, or blue, while anti-quarks carry color charge $\bar{\mathrm{R}}\bar{\mathrm{G}}\bar{\mathrm{B}}$ for anti-red, anti-green, or anti-blue. Gluons are

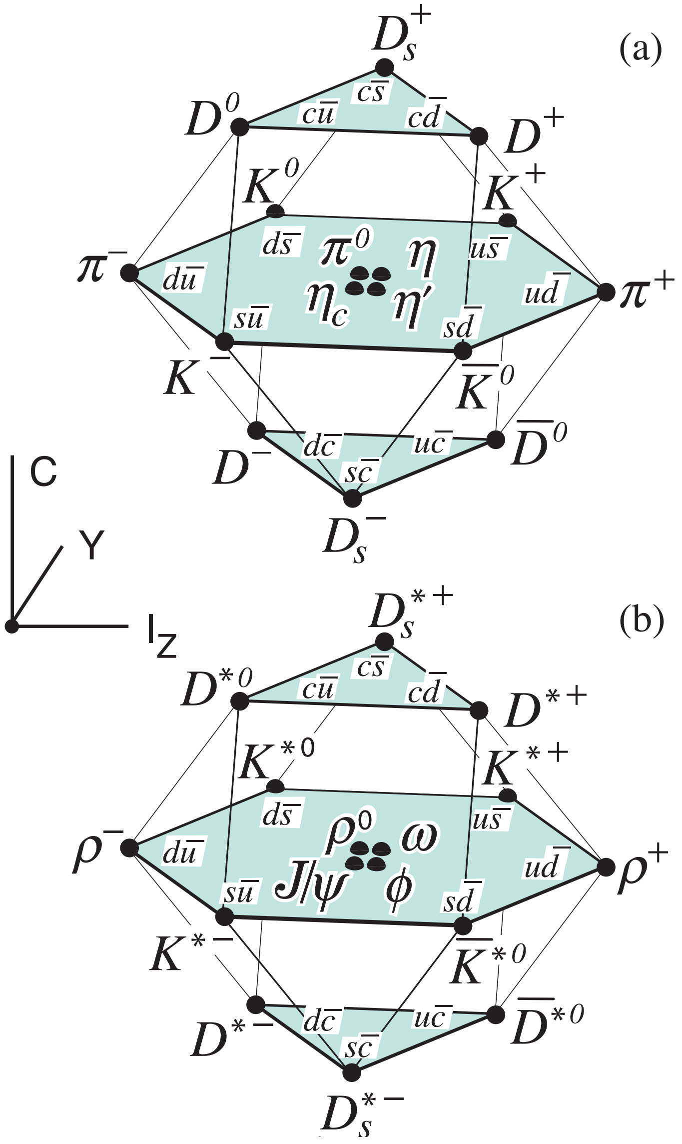

Figure 2.1: From [56], diagram of pseudoscalar (a) and vector (b) meson states composed of u, d, s, and c quarks.

massless mediator bosons that come in eight combinations of color and anti-color. The strength of the color charge in an interaction is summarized by a number known as a coupling constant. A weakly coupled interaction, such as the electric charge in Quantum Electrodynamics (QED), has a value much smaller than 1, or $\alpha_{\mathrm{QED}} \ll 1$, which enables a perturbative expansion of QED. In contrast, the QCD coupling $\alpha_s(Q)$ strongly depends on the energy used to probe an interaction which we denote as Q. The QCD coupling can be approximated as

$$\alpha_s(Q) = \frac{2\pi}{\beta_0 \ln(Q^2/\Lambda^2_{\mathrm{QCD}})} \tag{2.1}$$

where Λ_{QCD} is the energy at which the coupling constant becomes large and the physics becomes nonperturbative, $\beta_0 = 11 - \frac{2}{3}n_f$ with n_f being the number of quark flavors at or below the interaction energy μ. At high energies $Q^2 \gg \Lambda^2$ the running coupling $\alpha_s \to 0$, a discovery that was awarded the 2004 Nobel Prize in Physics. The QCD scale is measured to be about 217 MeV [41] which can also be seen in Figure 2.2.

2.1.3 Quantum Electrodynamics

Quantum Electrodynamics (QED) is among the most precise and stringent theories in physics. In electromagnetic interactions the photon mediates the force between electric charges. The photon, unlike gluons, is massless and does not self-interact

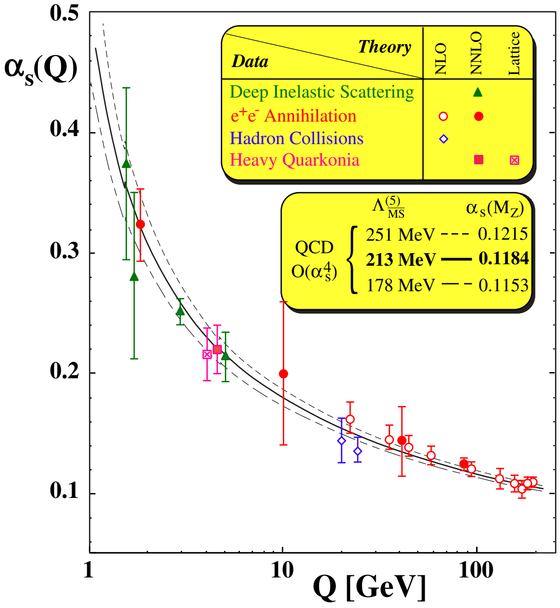

Figure 2.2: From [46], the running coupling constant as a function of momentum transfer Q^2 determined from different processes.

making the application of perturbative expansion feasible. A notable application of QED is the calculation of the scattering cross section $\sigma(e^+e^- \rightarrow e^+e^-)$, which is used to precisely determine the luminosity of an e^+e^- collider.

In experimental physics, a common approach to producing quarkonium is to collide electrons and positrons. When an electron and positron annihilate an intermediate virtual photon with quantum numbers 1^{--} will sometimes produce a quark anti-quark bound state with some energy dependent probability. One way to study quarkonium with different quantum numbers is to look for radiative transitions. A radiative transition involves an initial state hadron with quantum numbers $J_i^{P_iC_i}$ emitting a photon and transitioning to a final state hadron with quantum numbers $J_f^{P_fC_f}$.

In radiative decays an electromagnetic transition (EM) matrix takes an initial state (i) to a final state (f). While the EM amplitudes can be computed from first principles in lattice QCD, these calculations are still in their infancy [39]. Currently only potential models predictions are accurate enough to be compared to data. This approach allows the spatial dependence of EM amplitude to be described by functions of the quark position (r) between the initial and final state wave functions and the transition photon energy (k). To lowest order the transition matrix is an electric dipole or E1 transition with transition element $\langle f|r|i\rangle$ or in a magnetic dipole transitions M1 with a transition matrix $\langle f|j_0(kr/2)|i\rangle$, where $j_0(x) = \sin(x)/x$. In E1 transitions the spins do not flip ($\Delta S = 0$) so the angular momentum must necessarily change by one unit ($\Delta l = 1$). In M1 transitions the spin states flip ($\Delta S = 1$) and the angular momentum stays constant ($\Delta l = 0$). A multipole expansion of the transition matrix show that E1 transitions are favored relative to M1 transitions by $1/m_q^2$.

2.2 Charmonium

The bound state of a charm and anti-charm quark ($c\bar{c}$) is known as charmonium. The mass of the charm quark is heavy enough to slow their velocity (v) with respect to the speed of light (c) such that ($(v/c)^2 \approx 0.3$). This allows for a nonrelativitic treatment of their decays. Additionally, the strong coupling constant is of order 0.1 for charmonia which allows for their treatment in perturbative QCD. The heavy mass of the charm quark and the small coupling at charmonia energies make it an exciting place to test models and calculations of QCD.

2.2.1 Spectroscopy

Analogous to the hydrogen atom, different configurations of charm quark spins, angular momentum and radial excitation will lead to a spectrum of states. The potential between the charm and anti-charm quarks is modeled by a color Coulomb term at short distance, a linear confining term at large distances, and spin interaction terms. The mass spectrum can be approximated by ignoring relativistic effects. Figure 2.3 shows select electromagnetic and hadronic decays for known or candidate charmonium

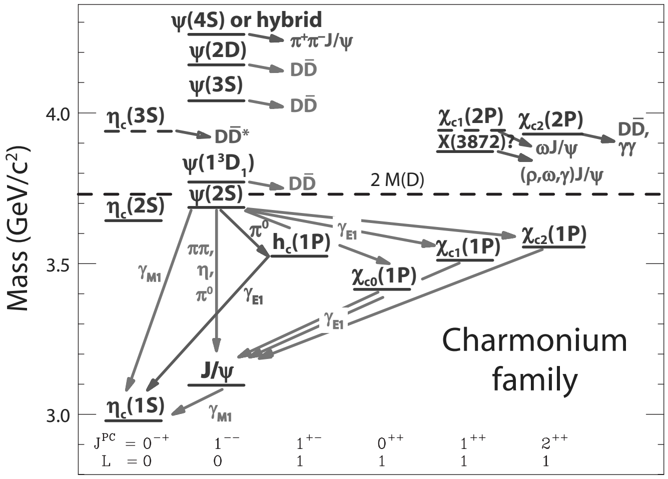

Figure 2.3: From [39], the known or candidate states of the charmonium family shown with select electromagnetic and hadronic decays.

states. The threshold for D meson pair production is shown as a dashed horizontal line.

The discovery of the first charmonium meson, J/ψ, was achieved simultaneously by experiments in Brookhaven [23], in collisions of protons on a stationary target, and SLAC [24], in electron-positron reactions. In the Brookhaven experiment the J/ψ was discovered in decays to $\mu^+\mu^-$. Detectors in high energy physics are designed to measure candidate charged and neutral particle momenta and energies. With knowledge of the initial center-of-mass energy and an application of conservation of energy and momentum the mass of the decaying particle is calculated. The width of this distribution is related, by the Heisenberg uncertainty principle, to its lifetime.

The current world average of the J/ψ width is 92 keV, which makes it the longest lived charmonium resonance with a lifetime of $\tau = \hbar/\Delta E = 7.2 \times 10^{-21} s$. The mass shape of most resonances with mass M and decay width Γ can be described by the Breit-Wigner distribution:

$$BW(m) \propto \frac{1}{(m-M)^2 + (\Gamma/2)^2} \tag{2.2}$$

The lifetime of the J/ψ is approximately 1000 times greater than the typical hadron. Two factors are responsible for the long lifetime of the J/ψ. First, flavor is conserved in strong interactions, so any hadronic reaction of $c\bar{c}$ must involve a mesons with net zero charm. The only other light charmonium resonance is the $\eta_c(1S)$ which is a ground state $c\bar{c}$ meson in a spin singlet state. Second, the J/ψ mass is too small to allow for decays involving a $D(c\bar{u})$ and $\bar{D}(\bar{c}u)$ mesons.

2.2.2 Radiative decays

A radiative transition takes an initial state meson into a final state meson by emitting a photon which carries with it $J^{PC} = 1^{--}$. The radiative transition of a resonance produced by e^+e^- annihilation offers the experimenter a way to probe final state configurations of the J^{PC} quantum numbers other than 1^{--}.

The M1 transition, $J/\psi \to \gamma\eta_c(1S)$, proceeds with a transition photon energy

(ω) of about 114 MeV. An illustration of this processes is shown in Figure 2.4. The transition photon spectrum can be written according to Eqn 2.3 [39]

$$\frac{d\Gamma}{d\omega} = \frac{4}{3}\alpha\frac{e_c^2}{m_c^2}\omega^3|M|^2 BW(\omega) \tag{2.3}$$

Where $M =< \eta_c(1S)|j_0(\omega r/2)|J/\psi >$ is the matrix element of the transition, $j_0(x) = \sin(x)/x$, e_c and m_c are the charm quark charge (in electron charge units) and mass, respectively. The Breit-Wigner, $BW(\omega)$, takes into account the with of $\eta_c(1S)$. In the limit $\omega \to 0$ the transition matrix tends to unity. As the photon energy increases the matrix element slowly decreases.

The CLEO experiment found the transition photon line shape in $J/\psi \to \gamma\eta_c(1S)$ to be asymmetric, which resulted in a poor fit to the $\eta_c(1S)$ mass distribution with only a Breit-Wigner. CLEO modified the the fit shape with an ω^3 term, which improved the fit around the $\eta_c(1S)$ peak, but also introduces a diverging tail at higher photon energies [55]. The tail was suppressed with a photon energy-dependent exponential, $\exp(-\frac{w^2}{8\beta^2})$, where $\beta = 65$ MeV. This damping term was motivated as the overlap of two ground state wave functions. As pointed out by [18], this argument only holds for potentials of harmonic oscillators. The KEDR damping factor in Eqn 2.4 does not pose any physical motivation and still adequately fits the data. KEDR showed no significant difference in their and CLEO's damping factor. In the analysis of $e^+e^- \to \gamma\eta_c(1S)$, the difference in $\eta_c(1S)$ signal yields with and without an energy-dependent electromagnetic transition with the KEDR damping factor is studied and taken as a systematic uncertainty, see Chapter 9.9.

$$\frac{d\Gamma}{d\omega} \propto \omega^3 \frac{\omega_0^2}{\omega\omega_0 + (\omega - \omega_0)^2} BW(\omega), \text{where } \omega_0 = \frac{M_{J/\psi}^2 - M_{\eta_c(1S)}^2}{2M_{J/\psi}} \tag{2.4}$$

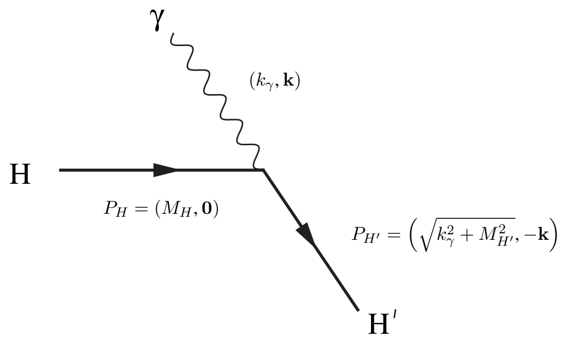

Figure 2.4: From [30], Kinematics of the radiative transition of quarkonium $H \to \gamma H'$ in the rest frame of H. The masses of the initial and final state quarkonium are M_H and $M_{H'}$, respectively. The momentum of the emitted photon is $k_\gamma = |k| = (M_H^2 - M_{H'}^2)/(2M_H)$.

2.2.3 Decays of $\eta_c(1S)$

The $\eta_c(1S)$ is the ground state $c\bar{c}$ spin singlet. The lifetime is on the order of 10^{-24} s. The $\eta_c(1S)$ decays into light meson combinations of pions, kaons, and ηs. At the moment only about 50% of all the $\eta_c(1S)$ decay modes have been measured over more than twenty decay channels [56]. The channels reconstructed in this analysis make up about 43.4% of the $\eta_c(1S)$ branching fraction. They are shown below: $\pi^+\pi^+\pi^-\pi^-\pi^0\pi^0$, $\pi^+\pi^-\pi^0\pi^0$, $\pi^+\pi^+\pi^-\pi^-\eta$, $K^+K^-\pi^+\pi^-\pi^0$, $\pi^+\pi^+\pi^+\pi^-\pi^-\pi^-$, $\pi^+\pi^+\pi^-\pi^-$, $\pi^+\pi^-\eta$, $K^\pm K_S\pi^\mp\pi^+\pi^-$, $K^\pm K_S\pi^\mp$, $K^+K^-\pi^0$, $K^+K^-\pi^+\pi^-$, and $K^+K^-\pi^+\pi^+\pi^-\pi^-$.

2.3 Charmonium-like vector states

A class of particles called ‘XYZ’ have opened up new opportunities in the study of QCD at the charmonium and bottomonium energy regimes. While each particle in the XYZ family are fascinating, this dissertation is concerned with the $Y(4260)$ and $Y(4360)$ states. The $Y(4260)$ and $Y(4360)$ are vector states, which make them directly accessible in electron positron annihilation experiments. The $Y(4260)$ was discovered in $\pi\pi\psi(1S)$ [20] and the $Y(4360)$ was discovered in $\pi\pi\psi(2S)$ with only upper limits placed on decays to $D\bar{D}$ [21, 60]. A number of things make the two Y states interesting and strongly suggest a non-conventional makeup. First, R scans of $\sigma(e^+e^- \to \text{hadrons})/\sigma(e^+e^- \to \mu^+\mu^-)$ show dip around the 4.26 GeV implying no resonance [6], see Figure 2.5. Second, a suppression of D^* meson pairs is also observed around 4260 MeV in scans of e^+e^- annihilation implying no resonance [34]. Third, the Y states are far outside the predicted masses of any conventional charmonia vector meson [43]. Lastly, there exists even more bizarre states called Z_c found in decays of the $Y(4260)$ and $Y(4360)$ in $\pi^{\pm}\psi(1S/2S)$, which can only be explained in terms of a tetra-quark or some other exotic quark makeup that yield net charge [3, 59]. These properties make cooperation between experimentalist and theorist all the more important. An overview of the many interpretations of the $Y(4260)$ and $Y(4360)$ will be presented in the following sections.

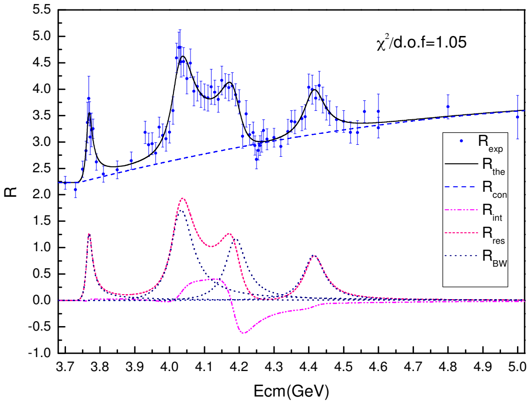

Figure 2.5: From [6], the fit to the R values for the high mass charmonium structure. The R values are shown with dots and error bars. The solid curve shows the best fit.

2.3.1 $Y(4260)$

Any theory of the $Y(4260)$ state must explain its large decay rates to the single charmonium state (J/ψ) along with some light mesons. A number of theories have been put forward to explain such a signature and some offer predictions that can be tested in the laboratory. More work is needed to understand the $Y(4260)$ but the following interpretations do give interesting possibilities.

One of the most striking facts about the $Y(4260)$ is its suppression of $D\bar{D}$ decays. This is particularly surprising considering that $Y(4260)$ is only $\approx$ 300 MeV above $DD\pi$ threshold. It is possible that the $Y(4260)$ is a molecular combination of a D meson pair. The favorite molecular combinations supported by QCD sum rules are $D^*\bar{D}_0 - \bar{D}^*D_0$ and $D\bar{D}_1 - \bar{D}D_1$. As Ref. [59] points out, the $\bar{D}D_1(2420)$ is the first open charm channel with relative S-wave to couple to $J^{PC} = 1^{--}$. Furthermore, the width of D_0 and $D_1(2430)$ are as large as 300 MeV and can, therefore, not explain the narrow width of the $Y(4260)$. A molecular combination does offer an explanation of the anomalous Z_c states as the consequence of low momentum $\bar{D}D^*$ pairs since $\bar{D}D_1$ and $\bar{D}D^*$ intermediate states can be simultaneously close to their mass shells. The Feynamn diagrams for $\bar{D}D_1(2420)$ molecular states are shown in Figure 2.6.

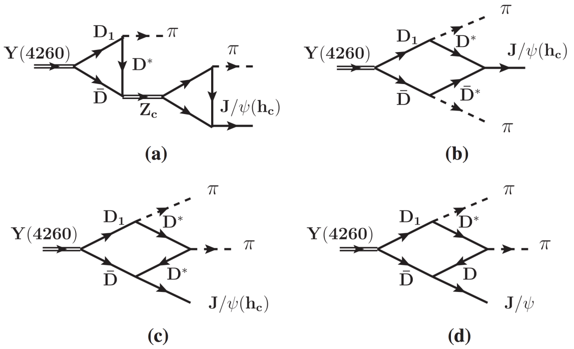

Figure 2.6: From [59], diagrams for $Y(4260) \rightarrow \bar{D}D_1 + c.c \rightarrow J/\psi\pi\pi$ and $h_c\pi\pi$ considered.

A four quark interpretation of the $Y(4260)$ has many interesting predictions, some of which can be tested at BESIII. A tetraquark is the bound state of a diquark with an anti-diquark or $([cs]_{S=0}[\bar{c}\bar{s}]_{S=0})_{P-wave}$ in the interpretation put forward in [53]. Such a tetraquark is predicted to have a mass of 4330 ± 70 MeV which is within the mass range of the $Y(4260)$ and $Y(4360)$. An important signature of this theory is that decays to $D_S\bar{D}_S$ are much greater than $D\bar{D}$ decays. The major drawback of this model is the proliferation of new, yet unobserved states, near the $\phi\psi(1S)$ and $f_0(980)\psi(1S)$ thresholds.

In the hybrid model of the $Y(4260)$ the charm and anti-charm quarks are coupled to a valence gluon. The constituent gluon is expected to add $700 \sim 1000$ MeV/c^2 to the corresponding charmonia mass [43]. Additionally, the quantum numbers of the constituent gluon with respect to the $c\bar{c}$ quarks augment the spatial parity and charge parity of the state by the following:

$$P = (-1)^{l_{c\bar{c}}+l_g}, C = (-1)^{l_{c\bar{c}}+S_{c\bar{c}}+1} \tag{2.5}$$

where $l_{c\bar{c}}$ is relative angular momentum between the $c\bar{c}$, l_g is the relative angular momentum of the gluon with respect to the $c\bar{c}$, and $S_{c\bar{c}}$ is the total quark spin. The total angular momentum of the hybrid charmonia system is $L = l_{c\bar{c}}+J_g$, where $J_g = 1$, is the total gluon angular momentum.

P	C	J	l_g	$l_{c\bar{c}}$	J_g	$S_{c\bar{c}}$	L
-	-	1	0	1	1	1	0
-	-	1	0	1	1	1	1
-	-	1	0	1	1	1	2
-	-	1	1	0	1	0	1

Table 2.2: The lowest $J^{PC} = 1^{--}$ hybrid states with their quantum numbers.

For the lowest $J^{PC} = 1^{--}$ hybrid states, equation 2.5 implies $l_{c\bar{c}} = S_{c\bar{c}}$ and $l_{c\bar{c}} + l_g$ odd. This gives the two possibilities, see Table 2.2

$$l_{c\bar{c}} = S_{c\bar{c}} = 0, l_g = 1 \tag{2.6}$$

and

$$l_{c\bar{c}} = S_{c\bar{c}} = 1, l_g = 0 \tag{2.7}$$

In the framework of lattice QCD (LQCD) Dudek et al [38] have calculated the partial width of an assumed hybrid charmonia state with a mass at 4.26 GeV decaying to $\gamma\eta_c(1S)$ and $\gamma\chi_{c0}$. Their calculation suggest that a hybrid charmonia around 4.26 GeV will preferentially decay to $\gamma\eta_c(1S)$ over $\gamma\chi_{c0}$ by about a factor of 2. This result suggests the $Y(4260)$ $c\bar{c}$ quarks are in a spin singlet configuration with a constituent gluon coupled to the $c\bar{c}$ in a P-wave. In this analysis only the $\gamma\eta_c(1S)$ channel is measured.

The hadrocharmonium scheme for the $Y(4260)$ consists of a core $c\bar{c}$ state loosely coupled to a shell of light quarks and gluons [29]. The decay to J/ψ in such a scheme is a natural consequence of the inner $c\bar{c}$ state staying bound and shedding its outer shell. The theory predicts that in the heavy quark limit of the inner core, decays to open charm are suppressed by $\exp(-\sqrt{\Lambda_{QCD}/m})$. It is unclear, though, whether the charm quark mass is heavy enough for such an assumption. Regardless, a few key properties are predicted by the theory such as decays to a J/ψ in a bound state with light nuclei or other baryons, and a suppression of $\pi\pi\psi(2S)$ with respect to $\pi\pi J/\psi$. The latter seems to be true but measurements of decays to baryon + J/ψ are lacking.

2.3.2 $Y(4360)$

The $Y(4360)$ shares many peculiar properties as the $Y(4260)$, namely: it did not show up in inclusive hadronic cross section (R) measurements; it does not seem to decay to any sort of D meson pairs; and is far in mass from any predicted 1^{--} charmonium.

In mass scans of $\pi\pi\psi(2S)$ a resonance near 4.36 GeV was measured by BaBar and Belle [22, 60]. While the two experiments find over 5σ evidence for a resonance, the masses and width are inconsistent with each other by 37 ± 26 MeV/c^2 and 98 ± 36 MeV/c^2, respectively. A combined fit to data from both experiments was done by Ref. [51] to better measure the $Y(4360)$ mass and width. The current world average $Y(4360)$ mass and width are 4354 MeV and 78 MeV, respectively.

If $Y(4360)$ were a conventional meson then based on its J^{PC} quantum numbers it could only be an S-wave or D-wave state. Since 1S, 2S, 1D, 3S, 2D, and 4S are already well established [31], the only other assignments are 3D, 4D, 5S, or 6S. Based on the predicted mass of these states from quark potential models a natural assignment for the $Y(4360)$ is 3^3D_1 [35]. A treatment of canonical decays of a $Y(4360)$ under the 3^3D_1 assignment has been theoretically undertaken by Ref [35]. Such calculations do provide a baseline for conventional processes that can be compared to measurements. For the moment, direct comparisons between theoretical partial width calculations and Born cross sections measured at electron-positron annihilation experiments is not possible due to the lack of experimental knowledge of the $e^+e^- \rightarrow Y(4360)$ coupling. The same applies to the $e^+e^- \rightarrow Y(4260)$ coupling.

The lightest charmonium hybrid ($c\bar{c}g$) predicted by Lattice QCD is about 4.1 GeV [26]. While the $Y(4360)$ is close in mass to this prediction, the favored $c\bar{c}g$ state is the $Y(4260)$.

Other interpretations such as a tetraquark or D meson molecular also hold for $Y(4360)$ as they did for $Y(4260)$. Careful study and a thorough analysis on the theoretical and experimental sides are needed to clear up the nature of the $Y(4360)$.

2.4 $e^+e^- \to \gamma\eta_c(1S)$ conventional processes between 4.0-4.6 GeV

The sensitivity of our measurements, $\sigma_E(e^+e^- \to \gamma\eta_c(1S))$, at six center-of-mass energies are marginal ($\leq 3\sigma$), which make interpreting the $\gamma\eta_c(1S)$ production mechanism an experimentally challenging task. To aide in our interpretation we can estimate the contribution to the cross section from conventional processes. In Chapter 2.4.2, we present nonrelativistic QCD (NRQCD) calculations of the nonresonant cross section of $e^+e^- \to \gamma\eta_c(1S)$. In Chapter 2.4.2, contributions to the measured cross section from the three conventional charmonium states between 4.0-4.6 GeV are discussed.

2.4.1 NRQCD

To distinguish whether $\gamma\eta_c(1S)$ is produced by some intermediate particle such as a $Y(4260)$ or $Y(4360)$ it is important to have a baseline of nonresonant behavior. In Ref. [61], G. Xu et al calculate the $e^+e^- \to \gamma^* \to \gamma\eta_c(1S)$ cross section as a function of e^+e^- center of mass energy in powers of $\alpha_s(v/c)^2$ to Leading Order (LO) and Next Leading Order (NLO). Additionally, calculations that take into account phase space contributions of α_s and $(v/c)^2$ are included which give additional systematic uncertainties to the calculations. As explained by the authors, phase space contributions are significant at BESIII energy region, but are complicated to calculate due to non-perturbative effects. Figure 2.7 shows the calculated $e^+e^- \to \gamma\eta_c(1S)$ production cross section for center of mass energies between 4-5 GeV.

2.4.2 Quark Model

Other contributions to the $e^+e^- \to \gamma\eta_c(1S)$ cross section include production via conventional charmonium resonances between 4.0-4.6 GeV. The three charmonium of interest are the 3^2S_1 $\psi(4040)$, the 2^3D_1 $\psi(4160)$, and the 4^3S_1 $\psi(4415)$ states. The quantitative features of these charmonium decays to $\gamma\eta_c(1S)$ can be extracted by modeling $c\bar{c}$ bound state non-relativistically with a potential that accounts for a one color exchange at short distance, a linear confining term at large distances, and spin interaction terms between quarks.

Based on calculations of the partial width $\Gamma(\psi(4040) \to \gamma\eta_c(1S)) = 9$ keV in Ref. [27], and the world average full width $\Gamma(\psi(4040)) = 80$ MeV, we can determine that $\psi(4040) \to \gamma\eta_c(1S)$ make up 0.01% of all $\psi(4040)$ decays. If we assume the $\psi(4040)$ can be modeled by a Breit-Wigner then an energy-dependent cross section $\sigma_E(e^+e^- \to \psi(4040) \to \gamma\eta_c(1S))$ can be estimated and compared to the measurements in this analysis, see Figure 8.3.

Unfortunately, similar calculations of the partial widths for $\psi(4160)$ or $\psi(4415)$ to $\gamma\eta_c(1S)$ are lacking so we cannot estimate the expected size of theses processes. Instead, as explained further in Chapter 10, we can let the size of these processes float to best fit the data. The resulting best fit lineshape can then be compare to the

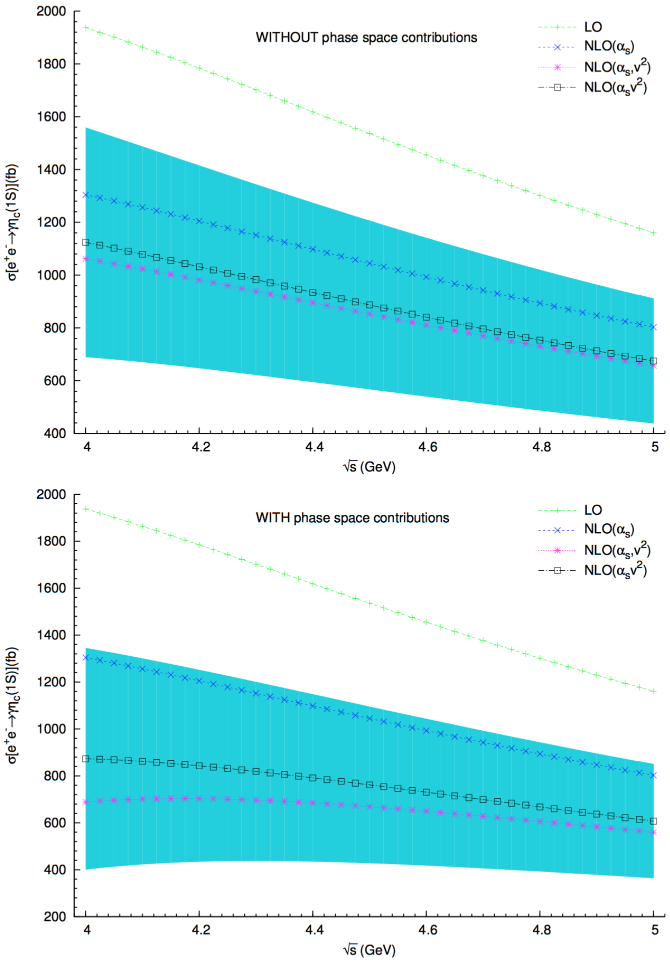

Figure 2.7: From [61], the nonresonant $e^+e^- \to \gamma\eta_c(1S)$ cross section calculated for energies between 4.0-5.0 GeV with (bottom) and without (top) phase space contributions.

measurements in this analysis.

Chapter 3

Experimental Apparatus

The aftermath of two colliding beams of particles is littered with a multitude of particle species hurled out from the collision point. With detectors serving as the eyes of such collisions sophisticated software is used to piece together the fragments to make a coherent picture of the interaction. This technique allows the high energy physicist to peer into strong, weak, and electromagnetic forces enabling the study of particle physics. The fragments generated from such interactions are bounded by the initial energy and quantum numbers, beyond that any particle that can be created will be. With the right energy a short lived resonance will sometimes pop into existence and quickly decay into a particular channel of other particles which themselves may be unstable further cascading to relatively long lived particles like leptons, pions, kaons, or photons. By reconstructing these fragments information about the original parent particle can be deduced.

As explained in Chapter 2, QCD is the fundamental theory of quark-gluon interactions. Since the gluon, the QCD force carrier, carries net color charge the gluon can self interact making the theory non-perturbative at large distances or energies below 1 GeV. This quirk of the gluon normally necessitates effective or phenomenological theories in order to do calculations at low and high energy quark energies. The BEPCII accelerator is designed to probe QCD at medium energies between 2-4.6 GeV. A high luminosity medium energy accelerator like BEPCII can reveal the interplay of perturbative and non-perturbative effects on hadronization as well as test phenomenological models or lattice QCD. In one year of running at the BEPCII design luminosity over a billion J/ψ events, over a billion $\psi(2S)$ and millions of $D\bar{D}$ and $\tau^+\tau^-$ decays can be accumulated, see Figure 3.1 [7]. Such high statistics allows for precision studies of J/ψ and $\psi(2S)$ and can lead to the discovery of rare decays. Better precision and new decays will undoubtedly lead to a better understanding of QCD.

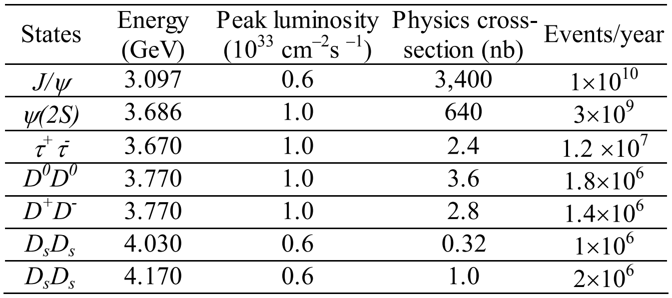

States	Energy (GeV)	Peak luminosity (10^{33} cm^{-2}s^{-1})	Physics cross-section (nb)	Events/year
J/ψ	3.097	0.6	3,400	1×10^{10}
$\psi(2S)$	3.686	1.0	640	3×10^{9}
$\tau^+\tau^-$	3.670	1.0	2.4	1.2×10^{7}
D^0D^0	3.770	1.0	3.6	1.8×10^{6}
D^+D^-	3.770	1.0	2.8	1.4×10^{6}
D_sD_s	4.030	0.6	0.32	1×10^{6}
D_sD_s	4.170	0.6	1.0	2×10^{6}

Figure 3.1: From [7], yields for different production processes studied at BESIII.

In total, about 30 thousand electronic signals make up the BESIII detector. It is designed to track, identify, and measure particles in its volume. A typical electron-positron interaction does not involve annihilation, instead, the electron and positron are more likely to scatter off each other. The scattering cross section of such interaction is precisely known making it an ideal process to measure the luminosity with. At BESIII the uncertainty on the luminosity measurement is about 1%, and is used as a systematic uncertainty in this analysis. A much rarer event involves the annihilation of e^+e^- pairs.

In e^+e^- annihilation a virtual photon with quantum number 1^{--} is briefly created with energy equal to the center of mass energy of the collision. The typical final states of such annihilations are showers of photons, leptons, pions, and kaons. These events must be separated from background processes. Prominent background processes include beam-gas interactions and cosmic radiation. In beam-gas interactions the electron or positron beam, just before colliding, interact with left over gas in the beam pipe. This nuclear interaction will either scatter the beam, reducing the luminosity, or interact with the nucleus creating a spray of hadrons. At BEPCII beam-gas interactions were studied and a 5×10^{-10} Torr pressure in the beam pipe near the collision was determined to sufficiently suppress such backgrounds [7]. Cosmic backgrounds can also contaminate the signal at BESIII. Cosmic ray muons will first interact with the outermost layer of the detector making such backgrounds easy to reject with a trigger system. The BESIII trigger is described in Section 3.6.

3.1 BEPCII

The Beijing Electron Positron Collider (BEPCII) is a particle accelerator designed to accelerate the e^+e^- to inject into an electron storage ring, see Figure 3.3. BEPCII is the successor to the BEPC accelerator which was in operation for 12 years [40].

On major improvement of BEPCII over BEPC is in the number of collisions per unit area per unit time or luminosity. The luminosity of an e^+e^- collider is expressed as [63]

$$L(cm^{-2}s^{-1}) = 2.17 \times 10^{34}(1+r)\xi_y \frac{E(GeV)k_b I_b(A)}{\beta_y^*(cm)} \tag{3.1}$$

where the beam aspect ratio at the interaction point is $r = \sigma_y^*/\sigma_x^*$, the vertical beam-beam parameter is ξ_y, the vertical beam envelope at the interaction point is β_y^*, the bunch number in each beam is k_b, and the beam current is I_b. The BEPCII accelerator is designed to improve the luminosity by a factor of 100 relative to BEPC. This required many hardware changes to the existing facility, which included replacing four normal conducting RF cavities in the storage ring with two superconducting RF cavities to shorten the bunch length; an improved electron to positron converter; and a special pair of superconducting insertion magnets near the IP to squeeze the beam envelope of the electrons and positrons just before colliding.

The beam parameters of BEPCII are summarized in Figure 3.2.

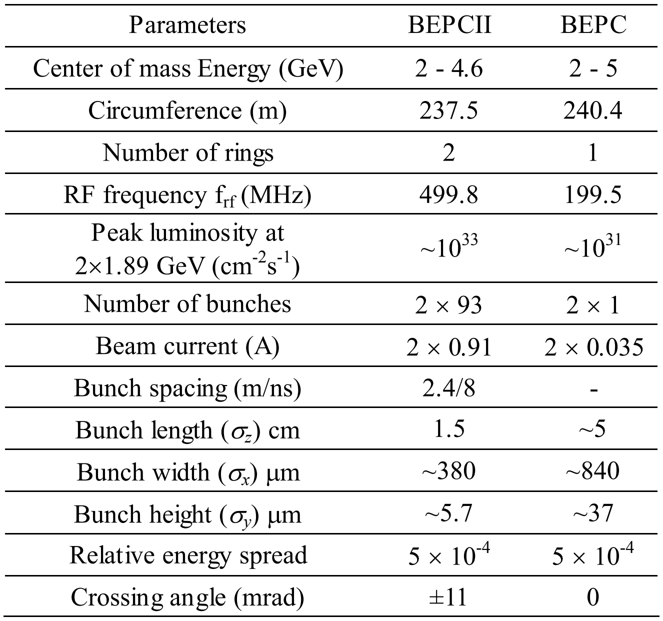

Parameters	BEPCII	BEPC
Center of mass Energy (GeV)	2 - 4.6	2 - 5
Circumference (m)	237.5	240.4
Number of rings	2	1
RF frequency f_{rf} (MHz)	499.8	199.5
Peak luminosity at 2×1.89 GeV ($cm^{-2}s^{-1}$)	$\sim 10^{33}$	$\sim 10^{31}$
Number of bunches	2 × 93	2 × 1
Beam current (A)	2 × 0.91	2 × 0.035
Bunch spacing (m/ns)	2.4/8	-
Bunch length (σ_z) cm	1.5	~5
Bunch width (σ_x) μm	~380	~840
Bunch height (σ_y) μm	~5.7	~37
Relative energy spread	5×10^{-4}	5×10^{-4}
Crossing angle (mrad)	±11	0

Figure 3.2: From [7], the BEPCII design parameters compared to BEPC.

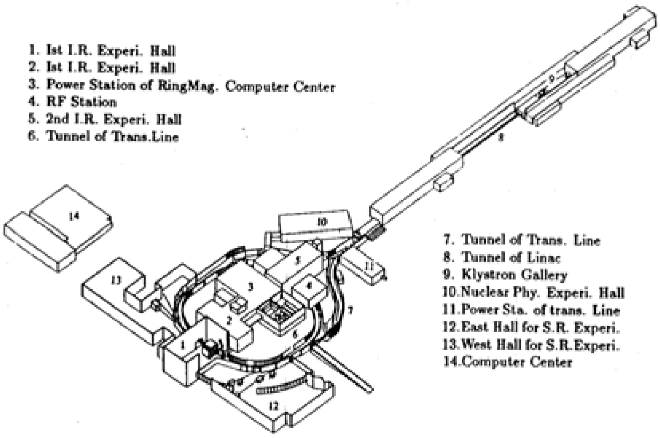

Figure 3.3: From [62], the layout of the Beijing Electron Positron collider facility.

3.1.1 Creation of e^+e^- beams

An electron gun system is used to produce the necessary high current and short pulse electrons needed for high luminosity running at BESIII. Electrons are produced via thermionic emission from the electron gun cathode. The Y796 cathode grid assembly used at BEPCII is a high emitting cathode capable of short 1 ns pulse beam and beam currents greater than 10 A. The repetition rate of the electron gun can be dialed to 12.5, 25, and 50 Hz [49].

The electrons are accelerated to 240 MeV before some are diverted to a separate beam line where they are converted to positrons. A positron beam is created by bombarding a tungsten target with electrons. The upgrade improved the positron rate by 20 times compared to its predecessor, essential for high luminosity running.

3.1.2 Injector Linac

The injector is responsible for identically accelerating the energy of the electrons and positrons to the storage ring. To study τ and charm physics the linac is designed to inject beams into the electron storage ring at energies between 1-2.3 GeV. The BEPCII linac, which includes the electron gun and positron converter is 202 m long.

The design of linear accelerators has evolved with the development of high power radio frequency (rf) sources, rf engineering, superconductivity, designs of accelerating structures, and high brightness electron sources [48]. The basic principle of a linac is to apply electric fields parallel to the charged particles direction of motion. At BEPCII e^+/e^- acceleration is driven by rf pulses propagating down a cylindrical waveguide. The waveguide is broken into cavities by disks separated a distance d, see Figure 3.4. The cavity size and rf frequency are chosen so that beams of charged particles are constantly accelerated down the 3.05 m long waveguide. The disks in the waveguide also serve the important function of slowing down the phase velocity of the electromagnetic (EM) wave. The radius of the iris and waveguide are tuned to match the EM and beam phase velocities. The BEPCII linear accelerator is composed of 56 normal conducting disk loaded waveguides and 16 rf power sources.

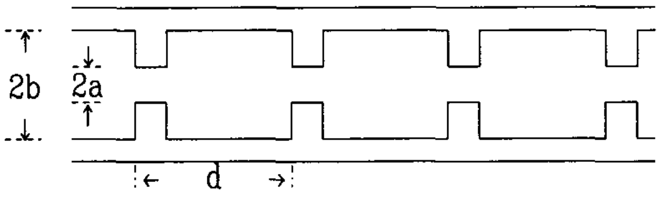

Figure 3.4: From [48], an illustration of a disk loaded waveguide used to accelerate e^+/e^- beams.

The improved BEPCII injector linac also provides the necessary beam current to maintain up to 93 circulating e^+/e^- bunches in the storage ring. This "top-off" scheme is possible for beam energies up to 1.89 GeV [7].

3.1.3 Beam Transport

The beam transport connects the injector LINAC and the electron storage ring. It is composed of a series of magnets designed to keep the beam size within design parameters until it reaches the electron storage ring. A lattice of bending magnets, quadrupoles and sextuples make up the beam transport.

The flux lines of a quadrupole magnet are shown in Figure 6.1. A quadrupole magnet is commonly used in accelerators to focus charged beams. One caveat of quadrupoles is that focusing in one direction leads to defocusing in the other. For this reason a typical beam transport will consist of both horizontal and vertical focusing quadrupoles. Not all particles of a beam are focused to the same spot due to differences in the beam bunch momentum. A high (low) energy particle will have a weaker (stronger) effective focusing strength. To correct for this and other chromatic effects sextuple magnets are employed. An understanding of beam envelope and dispersion of a beam throughout the lattice informs the accelerator physicist as to the best placement of sextuples and other magnets. At the end of the transport line the beam enters the storage ring where they will be bunched and collided at center of mass energies between 2-4.6 GeV.

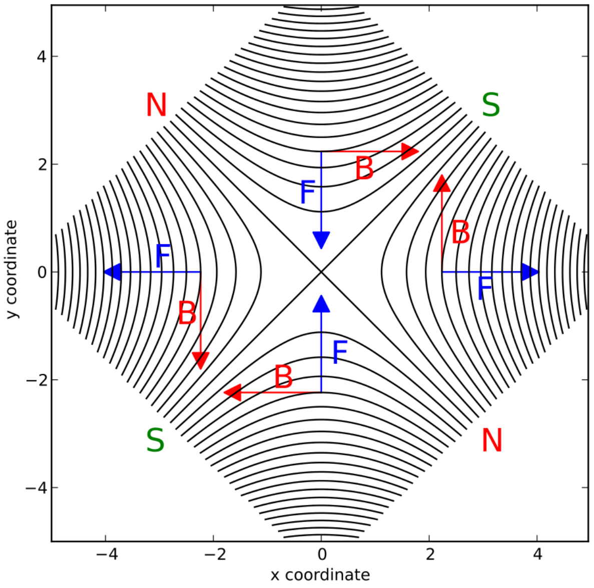

Figure 3.5: From Wikipedia, the free encyclopedia [33], the magnetic field lines of a typical vertical focusing quadrupole magnet.

3.1.4 Storage Ring

The storage ring at BEPCII is composed of two identical rings, each with a circumference of 237.5 m, see Figure 3.6. To keep the bunch number to as high at 93 for beam energies up to 1.89 GeV the beam optics in the storage and linac are identical. The maximum energy in this "top-off" injection scheme, 1.89 GeV, is the energy used to optimize the storage ring optics. The peak luminosity at center of mass energy 3.78 GeV is $\sim 10^{33} cm^{-2} s^{-1}$. This optimum center of mass energy is also the threshold for charm meson production.

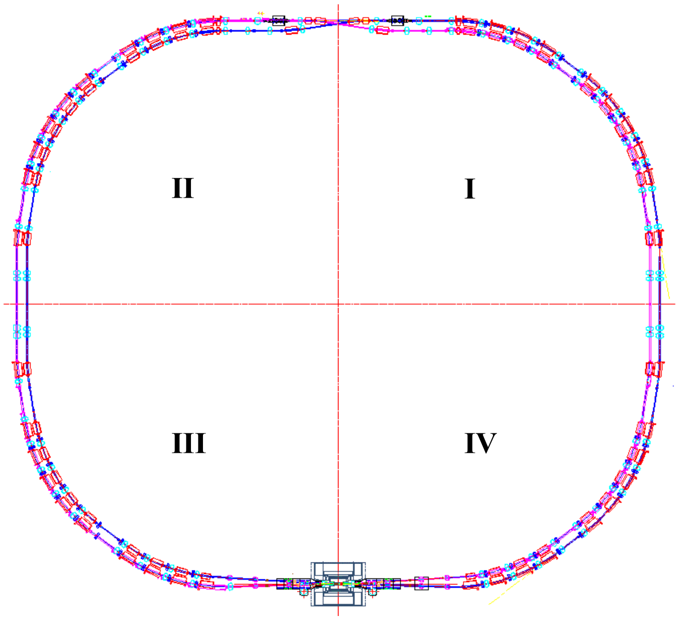

Figure 3.6: From [57], the lattice of dipole, quadrupole, and sextuple magnets that make up the BEPCII storage ring.

The beam collisions take place at the south crossing. The BESIII detector is built around the center of the collision. At the north region a vertical bump in the beams direction allows for the safe crossing of e^+/e^- beams. The horizontal crossing angle at the collision is 11 mrad.

An important design parameter for high luminosity running is the bunch length. The beam bunch length is shrunk by a pair of superconducting rf (SRF) cavities located at the north crossing. The bunch length after compression is 1.5 cm. The beam bunches are spaced by 8 ns.

The beam is steered by a lattice of dipole, quadrupole, and sextuple magnets. The dipole magnet provides a constant vertical magnetic field which bends the beam in a circle of radius ρ. The momentum rigidity of the beam is expressed at $B\rho = p_0/e$, where B is the magnetic field strength, and p_0 is the beam momentum. At the maximum BEPCII beam energy of 2.3 GeV the dipole field strength is $\sim$ 0.2 T. A total of 44 bending 60 quadrupole, and 36 sextuple magnets are used in the storage ring.

At the south crossing of the storage ring the e^+e^- beams collide. The BESIII solenoid is centered at the collision energy. The 3.52 m long solenoid severely influences the beams just before collision. A pair of superconducting insertion magnets (SIM) are installed near the interaction region to screen the beam from the solenoid and focus the beams. To screen the fields the SIM is composed of three superconducting compensation solenoids. The focusing is performed by a pair of superconducting quadrupoles.

On April 5, 2016 BEPCII came within 2% of the design luminosity, Figure 3.7.

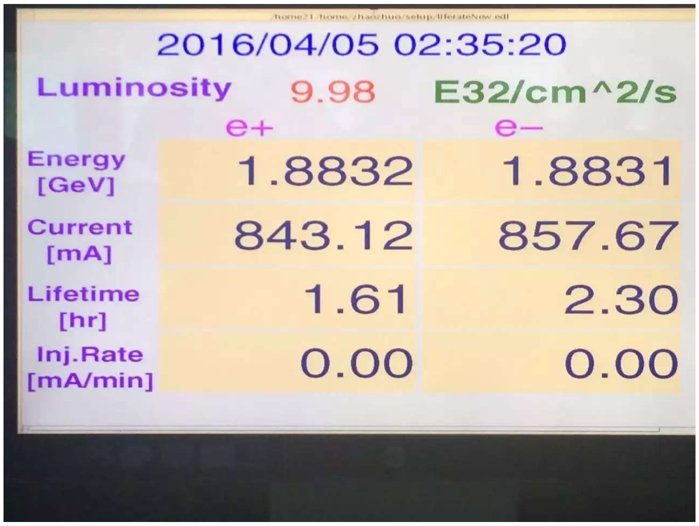

2016/04/05 02:35:20

Luminosity 9.98 E32/cm^2/s

	e+	e−
Energy [GeV]	1.8832	1.8831
Current [mA]	843.12	857.67
Lifetime [hr]	1.61	2.30
Inj.Rate [mA/min]	0.00	0.00

Figure 3.7: Record design luminosity at the BEPCII accelerator.

3.2 BESIII

The BESIII detector is a general purpose detector designed around the interaction region (IR) of the BEPCII collider. BESIII was designed to study the tau-charm energy regime. The collision of the two beams takes place at the center of the cylindrically shaped BESIII detector.

The BESIII detector is designed to capture charged and neutral particles with a geometric acceptance of 93% of 4π. The detector is composed of 5 subsystems which, in conjunction with the BESIII offline software system (BOSS), is designed to track particles everywhere in the detector volume, distinguish particle species like pions and kaons, and measure photon energies. The BESIII detector is shown in Figure 3.8. Charged particles are reconstructed in a multilayer drift chamber (MDC) covering the polar angle $|\cos\theta| < 0.93$. The momentum resolution (σ_p/p) and dE/dx resolution of charged tracks in the MDC are 0.5% and 6% at 1 GeV/c^2, respectively. Charged particles escaping the MDC hit a wall of plastic scintillator counters, or Time-of-Flight wall (TOF), placed around the MDC barrel and endcap. The timing resolution of the TOF is 100 ps in the barrel and 110 ps in the endcap. Electromagnetic showers are reconstructed in the Electromagnetic Calorimeter (EMC) by clustering crystal energies. The EMC is composed of 6240 CsI(T1) crystals arranged around the barrel and endcap regions. The energy resolution of showers (σ_E/E) at 1 GeV is 2.5% in the barrel and 5% in the endcap. The position resolution is 0.6 cm in the barrel and 0.9 cm in the endcap. Outside the EMC is the Superconducting Solenoid Magnet (SSM) which provides a uniform, on-axis 1 Tesla magnetic field for the MDC. The SSM is supported by a steel structure which provides the flux return for the magnet. High energy particles that make it through the EMC hit the muon chamber system (MUC) which is interleaved in the steel support structure. Hit patterns in the MUC are used to identify muons.

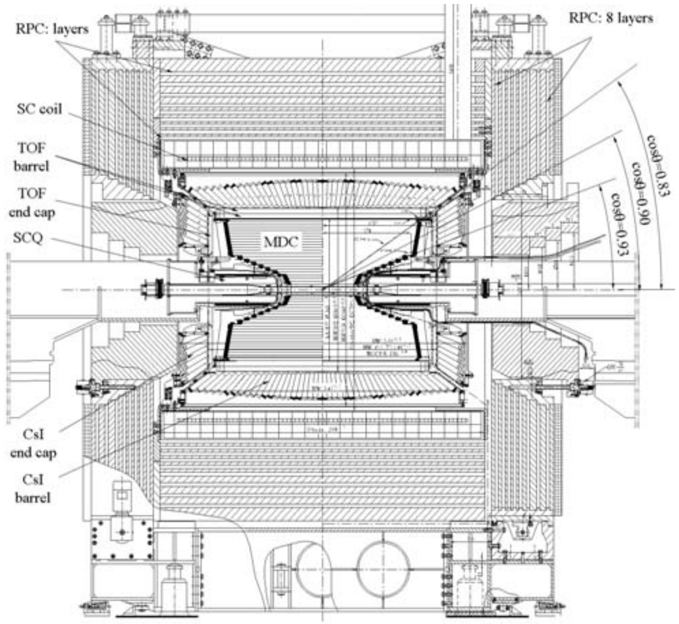

Figure 3.8: From [7], the BESIII detector.

3.3 Tracking

Tracking refers to the reconstruction of charged particles. Neutral particles are detected by calorimeters and will be further discussed in Section 3.5.

Tracking all charged particles generated in e^+e^- collisions everywhere in a detector as large as BESIII is a difficult task. To make way for the beam pipe, the multilayer drift chamber can only measure tracks in the polar angle $|\cos\theta| < 0.93$. Tracking is performed by the MDC and MUC detectors. The momentum p is determined by measuring the curvature of a charged particle in the presence of the uniform 1 T magnetic field provided by the Superconducting Solenoidal Magnet (SSM).

3.3.1 SSM

A uniform magnetic field in the volume of the drift chamber is important for accurate momentum measurements of charged particles. At BESIII this is achieved with a Superconducting Solenoid Magnet (SSM) which provides a 1 Tesla on-axis magnetic field. The solenoid has a mean radius of 1.482 m and a length of 3.52 m. To keep the solenoid at superconducting temperatures a cryogenic system supplies liquid helium to the coil. The coils are kept at 4.5 Kelvin.

The flux is returned by two forward yokes and a octagonal barrel yoke. The 50 ton weight of the solenoid, calorimeter, and drift chamber are supported by the yoke. The yokes are made up of steel plates with low carbon content (∼0.1%) whose magnetic properties were closely monitored to be within specifications [7].

The SSM deflects charged particles in helical patterns according to the Lorentz force. The sign of the electric charge dictates the direction of deflection. This allows the reconstruction algorithm to determine the sign of charged particles. The flux return and other magnetic field sources, such as the superconducting insertion magnets, can significantly alter the uniformity of the SSM. At BESIII, these sources were carefully studied to provide high precision tracking.

3.3.2 MDC

The multilayer drift chamber (MDC) is filled with a gas mixture that charged particles ionize. The trail of ionized gas are collected onto field and sense wires. The ions are forced to collect onto the grounded field wire due to the electric field induced by an array of sense wires kept at positive voltage. By arranging layers of such field wires tracking of the charged particle is accomplished.

A cross sectional view of the wire layers reveal many small drift cells. Each cell is centered about a 110 μm gold plated aluminum field wire surrounded by eight 25 μm gold plated tungsten sense wires. In total, 6,796 sense wires and 21,844 field wires make up the MDC.

The MDC is made up of an inner and outer chamber with the ability to replace the inner chamber. The inner radius of the MDC is 59 mm, 2 mm from the beam pipe, and the outer radius is 810 mm. For good position resolution drift cells in the inner drift chamber are approximately 12 mm high. To minimize material, the cell height in the outer chamber is increased to 16.2 mm.

The drift velocity of ions to the sense wire is dependent on the type of gas ionized, the electric field strength, and the 1 Tesla magnetic field. A helium based gas with 60% He to 40% propane (C_3H_8) was chosen to minimize multiple scattering. Measuring the time ions take to collect onto the sense wire with knowledge of the drift velocity gives the particle position within the cell. The resulting $r-\phi$ resolution for the MDC is better than 130 μm. Alternating layers of axial and stereo sense wire layers are used to determine the z position of charged tracks. Stereo wire layers with identical radius at both ends are rotated in ϕ creating a hyperboloid surface. The z resolution is between 3 mm to 4mm.

The design of the MDC was optimized for excellent momentum and position resolutions. The momentum resolution is limited by multiple scattering effects due to interactions of charged particles with material in the MDC. Efforts to reduce material and still achieve the needed tracking resolutions include using thin field wires, a helium based gas system, joining the inner and outer components of the drift chamber with no separating wall and an optimum drift cell size. Position resolution is dominated by the diffusion of ions generated from the primary charged particle. Designing small drift cells can reduce electron diffusion but increases material which impacts momentum resolution.

3.3.3 MUC

The outermost detector at BESIII is interleaved in the steel yoke that supports the 50 ton spectrometer. The MDC tracks large momentum charged particles that escape the spectrometer inner components. The steel yoke is broken into 9 barrel layers and 8 end cap layers of resistive plate chambers (RPC). The hits in each layer combined with tracking information from the MDC can be used to identify muons.

An RPC is housed inside a gas filled box. The ionization of the gas due to interactions with charged particles facilitates tracking, where the electric field is applied by plates held at positive voltage. The charge is collected on grounded readout strips. A double gap RPC can reach close to 98% muon tracking efficiency. A schematic of a super module composed of a grounded readout strip and a double gap RPC is shown in Figure 3.9

3.4 Particle identification system

Information from the MDC and TOF from charged particles are used as input to a particle identification system which can assign a probability for each particle species hypothesis. The candidate charged particles of primary interest are the electron,

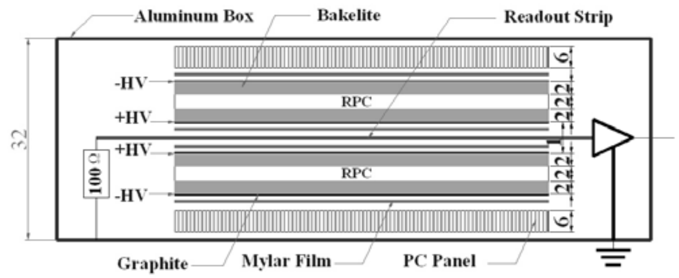

Figure 3.9: From [7], a double gap RPC super module at BESIII.

muon, proton, pion, kaon, and their respective anti-particle.

3.4.1 dE/dx

Charged particles interact with the gas in the MDC forming streaks of ions that are picked up by field wires. The pulse peak of the signal is related to the energy loss of the particle. Tracking the energy loss of the particle is used to derive dE/dx. Ionization energy loss is a function of momentum and mass by the relation, $\beta\gamma = p/m$. When dE/dx is plotted as a function of momentum some discrimination of charged particle species is evident, see Figure 3.10(a). At BESIII, kaons and pions can be separated by 3σ for momentum below 0.6 GeV/c and their is good e/π separation for momentum above 0.4 GeV/c.

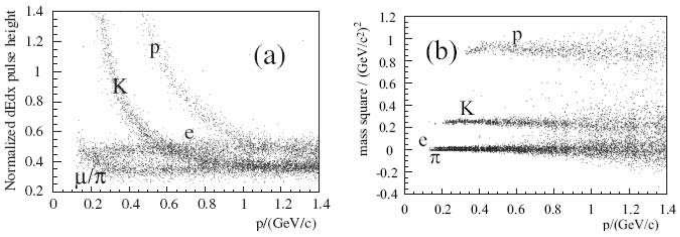

Figure 3.10: From [19], the BESIII particle identification system inputs as a function of momentum. (a) The energy loss per unit distance. (b) The expected mass square from TOF measurements.

3.4.2 TOF

The TOF is composed of plastic scintillator counters that run the length of the MDC. The MDC is enclosed by a double layer barrel and two single layer end cap TOF counters. Small gaps between the barrel and end cap TOF allow for mechanical access to the MDC and result in a polar angle coverage of $|\cos\theta| < 0.82$ in the barrel and $0.85 < |\cos\theta| < 0.95$ in the end cap.

When a charged particle interacts with the TOF they give off scintillation light that is read by a photomultiplier. The leading uncertainty of the TOF system is the intrinsic timing resolution of the plastic scintillator. At BESIII this is between 80-90 ps. The total timing uncertainty of the TOF detector is between 100 and 110 ps. Precise knowledge of the time and path length is combined to determine β, the velocity of the particle normalized to the speed of light. The energy of a particle if $E = \gamma m$ where $\gamma = \frac{1}{\sqrt{1-\beta^2}}$. From the energy-momentum relation we can re-write $E^2 = m^2 + p^2$ as $m^2 = p^2(\frac{1-\beta^2}{\beta^2})$, where p is the particles momentum. The mass square as a function of momentum at BESIII is shown in Figure 3.10(b). The TOF can provide 2σ discrimination of kaons and pions up to 0.9 GeV/c.

3.5 Calorimetry

While the MDC is an excellent device to learn about charged particles, it is oblivious to photons and other neutral particles. To learn about these neutral particles their energy must be measured in devices known as calorimeters.

3.5.1 EMC

The electromagnetic calorimeter (EMC) at BESIII is composed of 6240 CsI(Tl) crystals arranged around the TOF. The barrel is composed of 44 rings, each with 120 crystals. Each end cap consist of 6 rings that are split into two tapered half-cylinders. For mechanical support, cables, and cooling pipes a 50 mm gap separates the barrel and end cap. The polar angle coverage of the barrel is $|\cos\theta| < 0.83$ and $0.85 < |\cos\theta| < 0.95$ in the end cap for a total coverage of 93% of 4π.

Each crystal points towards the interaction region with a 1.5° tilt in the ϕ directions and 1.5° to 3° in the θ directions. This is to capture photons from the interaction point escaping through cracks between crystals. The material of the crystal plays an important role in determining the low energy threshold for photon detection and the light yield. The crystal best suited for physics at BESIII was the CsI(Tl). The minimum photon energies considered in our reconstruction are 25 MeV (in the barrel) and 50 MeV (in the end caps). The position resolution of the calorimeter is 0.6 cm for 1 GeV photons.

Attached at the end of the crystal are two Hamamatsu S2744-08 photodiodes. The choice of solid state photodiodes as opposed to traditional vacuum tube photomultipliers is necessary for its operation in the presence of strong magnetic fields. The silicon photodiode is powered by a pre-amplifier box and is attached to the center of the glass as shown in Figure 3.11. While the area of the two photodiodes is only about 10% of the total area of the back crystal, it can collect over 10% of the light. This is due to the reflective material wrapped around each crystal unit which provides efficient reflection and prevents light leakage.

Photons that hit the silicon photodiode will pair produce, and be accelerated by a gradient electric field produced by the pre-amplifier. The cascade of electrons and positrons results in a charge distribution whose area is proportional to the photon energy. The uniformity of energy measured in each crystal unit was carefully studied as this impacts the energy resolution. The quantum efficiency of each photodiode, the variation in its gain, and non-uniformities in the crystal are measured and taken into account when calibrating the crystal energy.

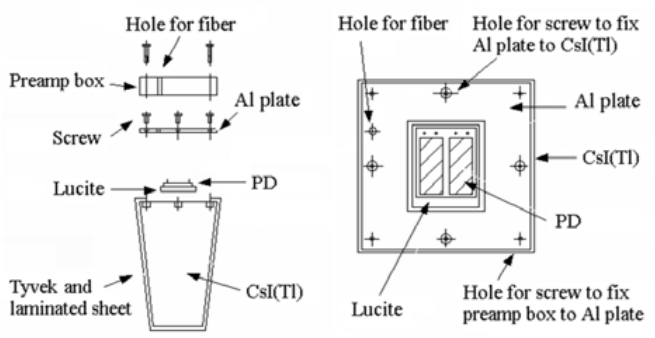

Figure 3.11: From [7], the mechanical assembly of an EMC crystal unit.

In $\pi^0 \to \gamma\gamma$ decays the showers of the two photons are converted into energy by clustering hits and summing over the energy in each crystal. By comparing the measured two photon mass with the well known π^0 mass the energy resolution σ_E/E can be calculated. The energy resolution of the BESIII EMC is 2.5% at 1 GeV.

3.6 Trigger

Detectors like BESIII which are close to the surface of the Earth suffer from the constant bombardment of cosmic ray muons. The cosmic ray event rate at BESIII is estimated at 1.5 kHz assuming the number of muons per meter-square per second is 170 and the BESIII detector cross section is $3\ m \times\ 3\ m$. With a level 1 (L1) trigger this event rate is suppressed to about 200 Hz. Based on the beam luminosity the event rate for physics is about 2 kHz. The total background rate after a L1 trigger is kept to less than 2 kHz.

The TOF response time from a physics interaction is the fastest of the BESIII subsystems. Hits in the TOF trigger the L1 trigger system. The L1 trigger system is additionally informed by the MDC and EMC, see Figure 3.12. The length of tracks reconstructed by the properties of the event are passed from each subsystem to yield basic trigger conditions. The final trigger decision is handled with the Global Trigger Logic (GLT). The TOF hit patterns and MDC tracks are combined by a Tracking Matching Logic unit that additionally informs the GLT.

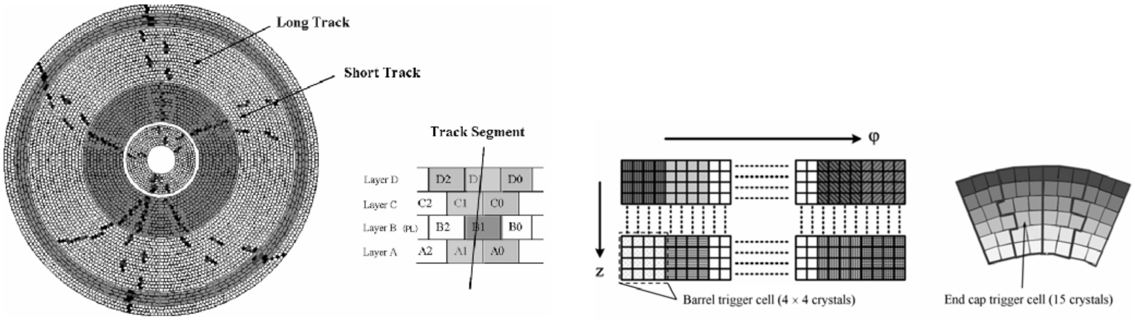

Figure 3.12: From [7], (left) long and short tracks reconstructed in the MDC, (right) EMC cell energies in the barrel and end cap.

The L3 trigger further suppresses background from signal events using specialized software packages that run off-line. After the L3 trigger background events are reduced to below 1 Hz while keeping the physics event rate constant.

3.7 Data Acquisition

The BESIII data acquisition system (DAQ) accomplishes data collection, event building, filtering, and recording of event data. The data rate must be reliable and handle over 30 thousand signals. The results of the L3 trigger are ultimately saved on disk. The data can be later analyzed using reconstruction software.

3.8 Data summary

The announcements from BaBar and Belle of unexpected vector charmonium-like particles inspired the BESIII collaboration to begin their own investigation in 2013. In 3 years over 5 fb^{-1} of electron-positron collisions have been accumulated. In this analysis we use a total integrated luminosity of 4.6 fb^{-1} spread among six center-of-mass energies: 482 pb^{-1} at 4.01 GeV, 1092 pb^{-1} at 4.23 GeV, 826 pb^{-1} at 4.26 GeV, 540 pb^{-1} at 4.36 GeV, 1074 pb^{-1} at 4.42 GeV, and 567 pb^{-1} at 4.60 GeV [5].

Chapter 4

BESIII Offline Software System

The velocity and volume of data produced by the BESIII detector stretches the limits of modern electronics. The detector is made-up of about 30K channels [7] that, when pieced together with software, can reveal the position, momentum, and energy of charged or neutral particles. Mapping channels to a detector component and combining that measurement for a higher level understanding of the interactions inside the detector are handled by the BESIII offline software system (BOSS). In this chapter we will discuss the simulation, calibration, and reconstruction of particles using the BESIII detector.

The BESIII offline software system (BOSS) was developed in C++ and built to incorporate external high energy physics (HEP) libraries. BOSS is designed to manage and process data collected by the BESIII detector. It also re-uses parts of code from other HEP experiments such as Belle, BaBar, ATLAS, and GLAST [7]. The BOSS framework is based around software that provides common interfaces for data processing and analysis called Gaudi [28].

Events that pass the L3 trigger and information concerning the data quality are saved to disk. These digitized detector signals are known as raw data. Raw data can also be generated by monte-carlo (MC) packages with the help of HEP libraries and Gaudi's event data service. Section 4.1 further describes select MC packages. Reconstruction algorithms and calibration constants are applied to raw data. The resulting data file is known as a data summary tape (DST). Gaudi's event data service can handle both raw and DST data types and is the common interface for reconstruction algorithms. BOSS also provides services and utilities than can be accessed by different algorithms. The magnetic field in the detector volume is provided by the magnetic field service. Services also exist that provide properties of particles and their paths. An overview of the software architecture of BOSS is shown in Figure 4.1.

4.1 Simulation

The simulation of particle interactions within the BESIII detector is a powerful tool used to model both signal and background processes. In addition, simulated data allows the experimentalist to study different aspects of the detectors performance such as: the detection efficiency of our final state $\eta_c(1S)$ decay channels and the mass resolution of the $\eta_c(1S)$ signal.

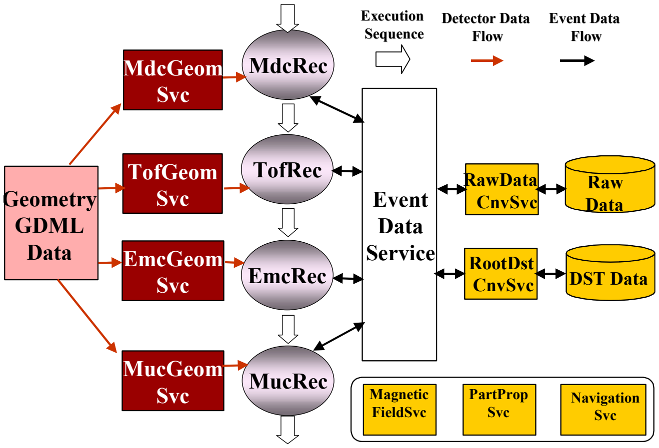

Figure 4.1: From [7], the BESIII software architecture overview.

When the detector picks up a signal from a particle it is sent to a trigger system. If the event passes L3 then properties of the signal are saved to disk. These properties include its shape, integral, and timing. Reconstruction software builds a picture of the interaction from these properties. The high level interaction of particles with the detector can be used to generate low level signal properties and run through the same reconstruction software. BOSS integrates about 30 generators written in Fortran. The generators relevant to this analysis will be discussed.

4.1.1 GEANT4

To simulate a particles interaction with the detector material GEANT4 [17] simulation software is used. Some of the BESIII detector shapes are difficult to model so the external packages G4TwistedTube [42] and G4IrregBox [1] were added. With this any particle can be simulated anywhere in the detector. At BESIII, this powerful tool is used to simulate particles produced from electron-positron annihilation with tunable center of mass energies at the center of the detector. The physics of a reaction such as the decay amplitude and rates is handled by KKMC and EvtGen. The physics domain of each generator is shown in Figure 4.2

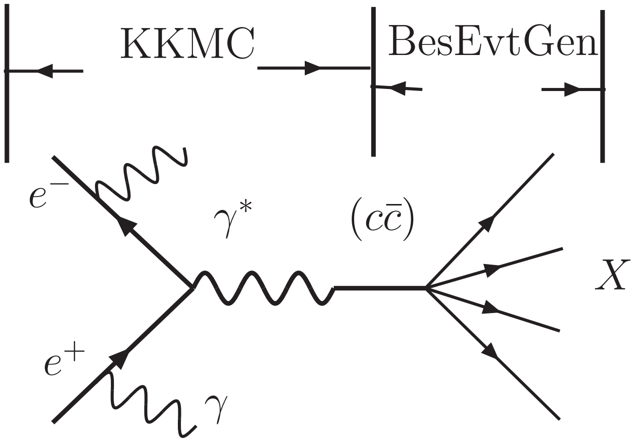

Figure 4.2: From [19], event generator framework at BESIII.

4.1.2 KKMC

The QED processes of e^+e^- annihilation to fermion anti-fermion pairs, $e^+e^- \to f\bar{f} + n\gamma$ $(f = \mu, \tau, d, u, s, c, b)$, is precisely implemented by KKMC [44]. Importantly, initial and final state interference effects are also implemented. The generator can simulate this e^+e^- interaction from $\tau^+\tau^-$ threshold to 1 TeV. At BESIII, KKMC is used to generate $c\bar{c}$ resonances with the inclusion of ISR effects and the beam energy spread.

4.1.3 EvtGen

The decay of a $f\bar{f}$ resonance produced by KKMC can be modeled in many ways. EvtGen is designed to use spin-density matrix information and a decay model of the probability amplitudes to generate a sequential decay chain. At BESIII, EvtGen is modified for tau-charm physics and called BesEvtGen. This analysis uses BesEvtGen to generate MC samples of signal and background processes [47].

4.2 Calibration

At BESIII each electronic signal undergoes some combination of amplification and pulse shaping before being digitized by a flash analog-to-digital converter (fACDC). The digitized pulse is then processed by a field programmable gate array (FPGA) which can extract the pulse integral. At any step in the electronics chain noise can contaminate the signal and reduce the design resolutions of the BESIII detector. These low level calibrations are performed regularly by using onboard pulse generators.

A particle physics detector will degrade due to the extreme radiation environment caused by colliding beams of electrons and positrons. Over time the components degrade and the design resolution worsens. By comparing MC of well-known decay processes with data we can calibrate the detector. Calibration often require large statistics which BESIII can provide with its high luminosity e^+e^- beam and by choosing physics processes with a large cross section. The MDC, for instance, used $J/\psi \to \mu^+\mu^-$ to calibrate both position and dE/dx. The efficiency in the MDC as a function of wire layer is shown in Figure 4.3. The MUC calibration involves studying the RPC detection efficiencies as a function of area. In addition, the cluster size and noise level are also studied.

The EMC is composed of CsI(Tl) crystals with a photodiode attached at the end to measure a particles energy as a charge distribution. The integral is related to the energy distributed in the crystal. The gain on each photodiode can be tuned which will change the signal integral. The gains in each crystal are recalibrated periodically and monitored frequently by a LED pulser system. Offline calibration is performed by analyzing $\pi^0 \to \gamma\gamma$ decays.

The TOF is made up of plastic scintillators which have a very fast response time. The timing and energy calibration is done by analyzing J/ψ to leptons. The effective velocity, attenuation length, muon energy loss, etc are saved to the calibration database for later use by the reconstruction algorithms. The status and performance of the TOF is monitored regularly by a laser-fiberoptics pulsing system.

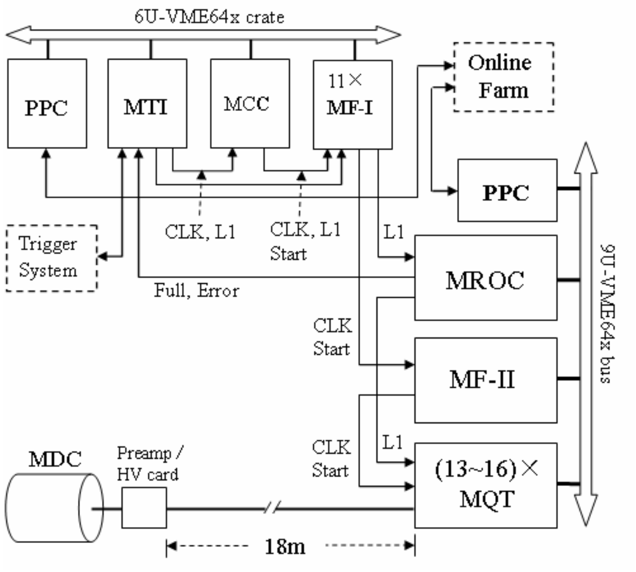

Figure 4.3: From [19], Electronics chain of the MDC.

4.3 Reconstruction

Digitized signals either real or simulated are mapped to physical space and reconstructed with various algorithms. The final states in the analysis involve charged particles which require track momentum and position reconstruction algorithms. The position of charged particles is calculated by a track-finding algorithm. The momentum additionally requires a track-fitting algorithm which is based on a Kalman-Filter. In addition, a probability is assigned to each charged particle species by a particle identification algorithm which combines information about dE/dx and time-of-flight.

Photons are measured by the electromagnetic calorimeter (EMC). When a photon shower hits the calorimeter its energy is distributed among multiple crystals. The crystal energies are then clustered to determine the original energy and position of the shower. Other final state particles include the π^0 and η mesons which are measured in their $\gamma\gamma$ decays.

Kinematic information about a particles decay is used to further select final state reactions. In the case of the π^0 and η mesons, combinations of two photon masses are constrained to fall within $107 < M(\gamma\gamma) < 163$ MeV/c^2 for the π^0 and $400 < M(\gamma\gamma) < 700$ MeV/c^2 for the η. The invariant mass of all final state particles can be compared to the center-of-mass energy of the e^+e^- collision to differentiate signal from background. The K_S meson primarily decays to charged pion pairs. The long mean lifetime of the K_S of about 90 ps leaves a displaced vertex with respect to the interaction point. In analyses involving a K_S the decay length of a K_S over its error L/σ can sometimes be a discriminator of signal from background. In this analysis we do not find selecting on L/σ for K_S candidates to be a significant discriminator of signal, but typically the decay length is at least twice as big as its variation.

While the algorithms used at BESIII are sophisticated and used in many other HEP experiments, they are imperfect and cannot reconstruct all particles in an event. Some of this is due fiducial constraints of the spectrometer and some is due to limitation of the detector subsystems to detect low energy particles. There is also the issue of combinatoric background due to intermediate particles which decay into photon or pion pairs. These issues are studied with the MC samples which model a signal process and is presented in Chapter 7. The reconstruction efficiency is also estimated from signal MC. Furthermore, MC is used to study the resolution of a particle due to the limitations of digitizing a signal in the detector.

Chapter 5

Statistical Techniques in High Energy Physics

The interactions of subatomic particles is fundamentally probabilistic due to its quantum mechanical nature. An experimenter, therefore, can only study such process by repeating an interaction a sufficient number of times. Since each event is independent we can borrow from the mathematics of probability and statistics to make measurements and test hypotheses.

The occurrence or nonoccurrence of a phenomena is known as an event [52]. Statistics provides a general framework to analyze events without needing to consider the nature of the event. A sample space is a set of all possible outcomes denoted by Ω. A collection of "interesting" events is a subset of Ω and denoted $\mathcal{F}$. The space $\mathcal{F}$ is a σ-algebra since each event must be assigned a probability where the probability is a function that maps $\mathcal{F} \rightarrow [0, 1]$. For all events A the probability satisfies the following requirements

$$P(A) \geq 0,\ P(\sum A_j) = \sum P(A_j),\ P(\Omega) = 1 \tag{5.1}$$

If the sample space Ω is composed of a finite number of disjoint events $\Omega = \cup_{j=1}^{m} A_j$ then the random variable X assigns to these events real numbers $x_{A1}, \ldots, x_{Am}$. For instance, a random variable could be the invariant mass of a set of particles for a specific event with probability $P(A_j)$. The concept of a random variable is more general than that of a random event in that for every random event A we can assign a random variable with a 1 or 0 indicator based on whether or not event A occurred denoted I_{Aj}. The expectation of a random variable $X = \sum_{j=1}^{m} x_j I_{Aj}$ is

$$E[X] = \sum_{i=j}^{m} x_j P(A_j) \tag{5.2}$$

The expectation $E(X - E[X])^2$ is called the variance and is a measure of the spread of the random variable. This is denoted $\sigma^2[X]$

$$\sigma^2[X] = E[X^2] - E^2[X] \tag{5.3}$$

The probability that event B occurs given the occurrence of event A is known as the conditional probability. For every event A with non-zero probability $(P(A) > 0)$ the conditional probability of event B given A is denoted

$$P(B|A) = \frac{P(B \cap A)}{A} \tag{5.4}$$

If the events A and B are independent then $P(B \cap A) = P(B)P(A)$. Random variables X and Y are independent if any event in X is independent from Y.

5.1 Distributions

A probability distribution assigns probabilities to each random event. A discrete probability distribution is known as a probability mass function or pmf, while a continuos distribution is known as probability density function or pdf. A simple random variable that forms the basis of the distributions discussed in this section involve a binary choice (success, fail) with respective probabilities (p, $1 - p$). This is known as the Bernoulli random variable.

5.1.1 Binomial

The Binomial distribution describes the probability of getting exactly k successes in n independent events of a Bernoulli random variable. The probability mass function is given by

$$Pr(X = k) = \binom{n}{k} p^k (1 - p)^{n-k} \tag{5.5}$$

where

$$\binom{n}{k} = \frac{n!}{k!(n-k)!} \tag{5.6}$$

The expectation and variance of a random variable X chosen from a Binomial distribution is $E[X] = np$ and $\sigma^2[X] = np(1-p)$, respectively.

5.1.2 Poisson

The Poisson distribution is made up of successive independent Bernoulli random variables that occurs within some interval. The pmf for observing k events in a given interval is expressed as

$$Pr(X = k) = \frac{\lambda^k \exp(-\lambda)}{k!} \tag{5.7}$$

where λ is the average number of events per interval. The expectation and variance for a Poisson distribution is λ.

5.1.3 Gaussian

In the limit of large n and λ the Binomial and Poisson distributions can be approximated by the Gaussian distribution given below

$$f(x|\mu, \sigma^2) = \frac{1}{\sqrt{2\pi\sigma^2}} \exp(-(x-\mu)^2/(2\sigma^2)) \tag{5.8}$$

where the mean $\mu = E[X]$ and the variance $\sigma^2 = Var[X]$. The central limit theorem states that under some conditions, the sum of many random variables will have an approximately Gaussian distribution.

5.2 Figure of Merit

We can separate the set of outcomes Ω into two disjoint subgroups S and B, where S represent the set of events classified as signal and B is the set of events classified as background. The number of events in S and B are N_S and N_B, respectively. The number of signal events and its error assuming Gaussian statistics is given by $N_S \pm \sqrt{N_S + N_B}$. The significance of the signal with respect to its error is then $N_S/\sqrt{N_S + N_B}$, which will be called the figure of merit in this analysis.

A "cut" is a function that maps $\Omega \to S$ and $\Omega \to B$. The application of successive cuts removes both signal and background with different figure of merits.

In Chapter 7.2.2 we study how well a "cut" or event selection removes background from signal where the figure of merit is optimized for each $\eta_c(1S)$ decay channel.

5.3 Kinematic fitting

A kinematic fit is a mathematical procedure that incorporates the laws of physics to improve the measurements describing the process [19]. For example, consider the reaction $e^+e^- \to \gamma\eta_c(1S)$ where $\eta_c(1S)$ decays to $2(\pi^+\pi^-\pi^0)$, $K^+K_S\pi^-$, or $\pi^+\pi^-\eta$, and where $K_S \to \pi^+\pi^-$, $\pi^0 \to \gamma\gamma$ and $\eta \to \gamma\gamma$. There are several constraints that can be applied here: the $\pi^+\pi^-$ pair from K_S decays can be constrained to share a common space point (2x2 - 3 = 1 constraint); in $\pi^0 \to \gamma\gamma$ the mass has to equal the mass of the π^0 (1 constraint); in $\eta \to \gamma\gamma$ the mass has to equal the mass of the η (1 constraint); and the final state energies and momentas must equal the initial center-of-mass energy (4 constraints). The application of these constraints improve the mass resolution of the η_c.

The χ^2/dof from kinematically fitting all final state particles to the initial center-of-mass energy with additional constraints on the invariant mass due to the intermediate π^0's, η's, or K_S's provides good signal to background separation in this analysis. In Chapter 7.2.2 we discuss the event selection procedure used to optimize this χ^2/dof. We discuss the systematic uncertainties due to the kinematic fit in Chapter 9.

The track parameters of a candidate particle can be defined in terms of seven parameters for four-momentum and position

$$\alpha_W = (p_x, p_y, p_z, E, x, y, z) \tag{5.9}$$

In general, the set of n tracks where each track parameter can have a generic number of parameters is denoted in vector form as

$$\alpha = \begin{pmatrix} \alpha_1 \\ \alpha_1 \\ \vdots \\ \alpha_n \end{pmatrix} \tag{5.10}$$

The errors for each track measurement make up the diagonal elements of the so called "weight matrix" which is denoted as $V_{\alpha 0}^{-1}$ [25] and defined below

$$V_{\alpha 0}^{-1} = \begin{bmatrix} 1/\sigma_{\alpha 1}^2 & 0 & \cdots & 0 \\ 0 & 1/\sigma_{\alpha 2}^2 & \cdots & 0 \\ \vdots & \vdots & \ddots & \vdots \\ 0 & 0 & \cdots & 1/\sigma_{\alpha n}^2 \end{bmatrix} \tag{5.11}$$

We can write the r constraint functions generally as

$$\mathbf{H}(\alpha) \equiv 0, \text{ where } \mathbf{H} = (H_1 \; H_2 \; \cdots \; H_r) \tag{5.12}$$

We can expand 5.12 around α_0 to yield the linearized equations

$$0 = \frac{\partial H(\alpha_0)}{\partial \alpha}(\alpha - \alpha_0) + H(\alpha_A) = \mathbf{D}\delta\alpha + \mathbf{d} \tag{5.13}$$

where $\delta\alpha = \alpha - \alpha_0$ and the matrices are

$$\mathbf{D} = \begin{bmatrix} \frac{\partial H_1}{\partial \alpha_1} & \frac{\partial H_1}{\partial \alpha_2} & \frac{\partial H_1}{\partial \alpha_3} & \cdots & \frac{\partial H_1}{\partial \alpha_n} \\ \frac{\partial H_2}{\partial \alpha_1} & \frac{\partial H_2}{\partial \alpha_2} & \frac{\partial H_2}{\partial \alpha_3} & \cdots & \frac{\partial H_2}{\partial \alpha_n} \\ \vdots & \vdots & \vdots & \ddots & \vdots \\ \frac{\partial H_r}{\partial \alpha_1} & \frac{\partial H_r}{\partial \alpha_2} & \frac{\partial H_r}{\partial \alpha_3} & \cdots & \frac{\partial H_r}{\partial \alpha_n} \end{bmatrix}, \ \mathbf{d} = \begin{pmatrix} H_1(\alpha_0) \\ H_2(\alpha_0) \\ \vdots \\ H_r(\alpha_0) \end{pmatrix} \tag{5.14}$$

The χ^2 with r degrees of freedom is written as

$$\chi^2 = (\alpha - \alpha_0)^T V_{\alpha 0}^{-1} (\alpha - \alpha_0) + 2\lambda^T (\mathbf{D}\delta\alpha + \mathbf{d}) \tag{5.15}$$

where λ is a vector of r unknown Lagrange multipliers and $V_{\alpha 0}$ is the covariance matrix. The χ^2 is minimized with respect to α and λ. The resulting vector equations can be used to solve for the parameters α and their covariance matrix:

$$\begin{aligned} V_{\alpha 0}^{-1}(\alpha - \alpha_0) + \mathbf{D}^T\lambda &= 0 \\ \mathbf{D}\delta\alpha + \mathbf{d} &= 0 \end{aligned} \tag{5.16}$$

The solution can be written as:

$$\begin{aligned}\alpha &= \alpha_0 - V_{\alpha 0}\mathbf{D}^T\lambda, \\ \lambda &= V_D(\mathbf{D}\delta\alpha_0 + \mathbf{d}), \qquad (5.17) \\ V_\alpha &= V_{\alpha 0} - V_{\alpha 0}\mathbf{D}^T V_D \mathbf{D} V_{\alpha 0}\end{aligned}$$

where $V_D = (\mathbf{D}V_{\alpha 0}\mathbf{D}^T)^{-1}$ is the covariance matrix after the constraint with dimensions $r \times r$ and

$$\chi^2 = \lambda^T V_D^{-1}\lambda = \lambda^T(\mathbf{D}\delta\alpha_0 + \mathbf{d}) \ . \qquad (5.18)$$

The nonlinearities in the constraint equations requires the kinematic fitting to be an iterative procedure until convergence is satisfied.

5.4 Likelihood Fitting

The likelihood that a *hypothesis* H describes a dataset $\mathbf{x}$ is denoted $L(H) = P(\mathbf{x}|H)$, where $\mathbf{x}$ is the set of n outcomes of an experiment. Generally, the likelihood function is obtained from the probability of the data under a hypothesis. In many cases the hypothesis can be described by one or more continuous variables θ so the likelihood becomes $L(\theta) = P(\mathbf{x}|\theta)$. A special case of the likelihood function is when the data consist of independent and identically distributed (i.i.d) values. For a dataset of n

i.i.d quantities $\mathbf{x} = (x_1, \ldots, x_n)$ described by a common probability density function (p.d.f) $f(\mathbf{x}; H)$ we can write the likelihood as

$$L(\theta) = P(x_1, x_2, \ldots, x_n|\theta) = P(x_1|\theta)P(x_2|\theta)\cdots P(x_n|\theta) = \prod_{i=1}^{n} f(x_i|\theta) \tag{5.19}$$

The likelihood and χ^2 are related if, for a set of n independent measurements y_i at a known x_i, y_i is assumed to be Gaussian distributed with mean $\mu(x_i;\theta)$ and known variance σ_i^2. The likelihood is

$$\begin{aligned} L(\theta) &= \prod_{i=1}^{n} \frac{1}{\sqrt{2\pi\sigma_i^2}} \exp(-(y_i - \mu(x_i;\theta))^2/(2\sigma^2)) \\ -\ln(L(\theta)) &= \sum_{i=1}^{n} \frac{(y_i - \mu(x_i;\theta))^2}{2\sigma_i^2} + constant \\ \chi^2(\theta) &= -2\ln L(\theta) + constant \end{aligned} \tag{5.20}$$

The data will be best described by a hypothesis when the parameters $\hat{\theta}$ maximize the likelihood function. Equivalently, the maximum likelihood estimators can also be determined by minimizing $\ln L(\theta)$ which can be found by solving

$$\frac{\partial \ln L}{\partial \theta_i} = 0, \ i = 1, \ldots, N \tag{5.21}$$

where N is the number of parameters in θ. In practice, the maximum likelihood estimators are found numerically.

A minimization routine used in this analysis and more broadly in high energy physics is called MINUIT [45].

In a fitting procedure algorithms are used to estimate the parameters $\hat{\theta}$ that best describe the data. These estimators maximize the likelihood function.

The number of n independent measurements in the expressions above are assumed to be fixed. To incorporate a case where n is itself dependent on the parameters of the hypothesis θ we need to augment the likelihood function. This is known as the extended likelihood. If n follows a Poisson distribution the likelihood becomes

$$L(\theta) = \frac{\mu^n}{n!} e^{-\mu} \prod_{i=1}^{n} f(x_i;\theta) \tag{5.22}$$

The number of outcomes for a given p.d.f $f(x_i;\theta)$ can be varied to maximize the likelihood function

5.5 Hypothesis test

A hypothesis attempts to model a given set of data in terms of a set of parameters. This model based understanding of data is particularly important in high energy physics since the data is describing some physical process. For instance, the model to explain the recoil-mass distribution of the transition photon for an $\eta_c(1S)$ decay channel in this analysis might, in addition to the parameters that describe the backgrounds, also include parameters to describe the $\eta_c(1S)$ signal. The data can then be fit with two hypothesis and their likelihoods compared, namely: a background only hypothesis denoted H_{B}; a signal plus background hypothesis denoted $H_{\mathrm{S+B}}$. The maximum probability to reject H_{B} if $H_{\mathrm{S+B}}$ is true can be determined by defining a test statistic $\lambda(\mathbf{x})$ defined as

$$\lambda(\mathbf{x}) = \frac{f(\mathbf{x}|H_{\mathrm{S+B}})}{f(\mathbf{x}|H_{\mathrm{B}})} = \frac{L(\theta_{\mathrm{S+B}}|\mathbf{x})}{L(\theta_{\mathrm{B}}\mathbf{x})} \tag{5.23}$$

where $f(\mathbf{x}|H)$ is the probability density function with hypothesis H fit to data $\mathbf{x}$. The pdf can be replaced with the appropriate likelihood functions of parameters θ given the data $\mathbf{x}$. If certain general conditions are satisfied then Wilks' theorem states $-2ln\lambda$ approaches a χ^2 distribution in the limit of large data samples. If the difference in the number of degrees of freedom between $H_{\mathrm{S+B}}$ and H_{B} is $\Delta(H_{\mathrm{S+B}} - H_{\mathrm{B}}) = 1$ then the significance is simply $\sqrt{-2\ln\lambda}$.

5.6 Upper limits

A model may have many free-floating parameters that are varied to maximize the likelihood. A profile of the likelihood for a single free parameter can be mapped by fixing all other parameters to their best value. The likelihood profile of the $e^+e^- \to \gamma\eta_c(1S)$ cross section at $E = 4.26$ GeV in Figure 5.1 (left) shows a sharp distribution peaked at the nominal cross section measurement. The value of the cross section that encompasses 90% of the distributions area defines the upper limit of the measurement to 90% confidence. This profile of the likelihood is probing the statistical uncertainty of the measurement. To incorporate the systematic uncertainty into our upper limit we assume the systematic error is normally distributed about 0 with a width equal to the systematic error in picobarns ($\sigma_{\text{syst.}}$) which will be denoted $\mathcal{N}(0, \sigma_{\text{syst.}}; x)$, where x is in picobarns. We can then convolve the profile likelihood of the cross section with $\mathcal{N}(0, \sigma_{\text{syst.}}; x)$ and integrate the distribution to 90% of the area. To be conservative in our estimate we integrate the likelihood distribution starting at 0 given by the following:

$$0.9 = \frac{\int_0^x L(u) \oplus \mathcal{N}(0, \sigma_{\text{syst.}}; u) du}{\int_0^\infty L(u) \oplus \mathcal{N}(0, \sigma_{\text{syst.}}; u) du} \tag{5.24}$$

where x is the upper limit cross section to 90% confidence.

5.7 Summary

In this chapter we motivate the use of probability and statistics in high energy physics. We discuss specific probability distributions often encountered by practitioners of

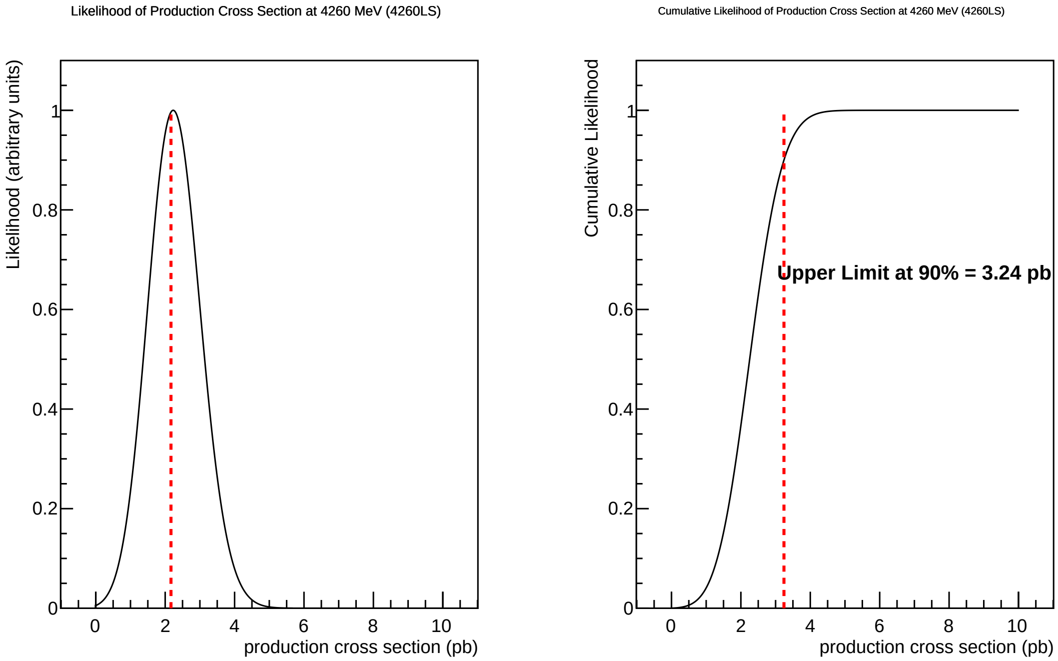

Figure 5.1: The cumulative likelihood as a function of signal yield, in pb, when fixing all other fit parameters. The fit combines all energies and assumes a Breit-Wigner Y(4260) lineshape. The 90% confidence line which does include the systematic uncertainty is overlaid.

statistics. In addition, we discuss advanced topics such as the figure of merit, kinematic fitting, maximum likelihood estimation, hypothesis testing, and the upper limit. These topics are motivated by their use in this analysis. The figure of merit and kinematic fit are both used in this analysis to best select final states consistent with decaying from an $\eta_c(1S)$, see Chapter 7. In Chapter 8 we will fit distributions of the transition photon recoil-mass by maximizing the likelihood of the fit. In this way we can extract a Born cross section for the process $e^+e^- \to \gamma\eta_c(1S)$. An upper limit is then extracted using the technique described in section 5.6. The significance of the $e^+e^- \to \gamma\eta_c(1S)$ is also determined by fitting distributions of the transition photon recoil-mass with and without an $\eta_c(1S)$ signal. By comparing their likelihoods we can use Wilks Theorem to calculate the $e^+e^- \to \gamma\eta_c(1S)$ significance.

Chapter 6

Measuring e^+e^- cross section

The strong, weak, and electromagnetic interactions can all be studied by annihilating e^+e^- beams. Unlike colliding hadronic beams, a particle created from e^+e^- annihilation has well constrained J^{PC} quantum numbers of 1^{--}. The probability that the e^+e^- beams annihilate and produce a resonance X is known as the cross section. In this chapter we introduce measurements of $\sigma(e^+e^- \rightarrow X)$, where σ is the cross section to produce a resonance X. This chapter first introduces the concept of a resonance and how to theoretically derive an interaction cross section. The last sections introduce experimental techniques to measure a cross section. We motivate these techniques around the study of the Y(4260).

6.1 Theoretical cross section

A particle decaying via the strong interaction has a lifetime of about 10^{-23} s and, therefore, does not live long enough to be measured in a detector. Instead, this type of particle, also known as a resonance, is identified by tracking its decay products. The total momentum and energy of the daughter particles make up the resonance mass. Due to the short lifetime of a resonance the mass uncertainty of about $h/\Delta t$ is measurable at detectors like BESIII. The decay of such an unstable resonance proceeds according to an exponential law

$$|\psi(t)|^2 = |\psi(0)|^2 \exp(-\Gamma t) \tag{6.1}$$

where the lifetime of the state is $\tau = \hbar/\Gamma$. We can thus write the time dependence of $\psi(t)$ as

$$\psi(t) \sim \exp(-iMt)\exp(-\Gamma t/2) \tag{6.2}$$

where M is the rest mass of the state. Applying a Fourier Transform transforms the wave function to the energy domain

$$\begin{aligned} \chi(E) &= \int \psi(t)\exp(iEt)dt && (6.3) \\ &\sim \frac{1}{E - M + (i\Gamma/2)} && (6.4) \end{aligned}$$

The probability of forming a resonance is proportional to $\chi(E)\chi(E)^*$. We can write the cross section of such a resonances then as

$$\sigma(E) = \sigma_{\max}\frac{\Gamma^2/4}{(E-M)^2+(\Gamma/2)^2} \tag{6.5}$$

Eqn 6.5 is also known as the non-relativistic Breit-Wigner form of a resonance [41] of mass M and full width at half maximum Γ. In Lorentz invariant relativistic form the interaction cross section can be written as [58]

$$\sigma(s) = \sigma_{\max}\frac{M^2\Gamma^2}{(s-M^2)^2+\Gamma^2M^2} \tag{6.6}$$

where s is the center of mass energy squared. The general form of $\sigma_{\max}$ for resonances produced by the interaction of two incident particles is

$$\sigma_{\max} = \frac{2J+1}{(2S_1+1)(2S_2+1)}\frac{4\pi}{k^2}\mathcal{B}_{in}\mathcal{B}_{out} \tag{6.7}$$

where J is the total angular momentum of the resonance, $(2S_1+1)$ and $(2S_2+1)$ are the number of polarization states of the incident particles, k is the center of mass momentum of the resonance, $\mathcal{B}_{in} = \Gamma_{in}/\Gamma$ is the branching fraction of the incident particles into the resonance and $\mathcal{B}_{out} = \Gamma_{out}/\Gamma$ is the branching fraction of the resonance into the final state channel. For resonances produced from e^+e^-

incident particles the Lorentz invariant cross section simplifies to

$$\sigma(s) = \frac{12\pi\Gamma_{ee}\Gamma_f}{(s - M^2)^2 + \Gamma^2 M^2} \tag{6.8}$$

where Γ_{ee} is the partial width of forming the resonance from e^+e^- or, equivalently, the decay of the resonance into the e^+e^- decay channel and Γ_f is the partial width in the final state channel. A detailed analysis of a resonance should also account for resonance production and decay near thresholds that inhibit the phase space.

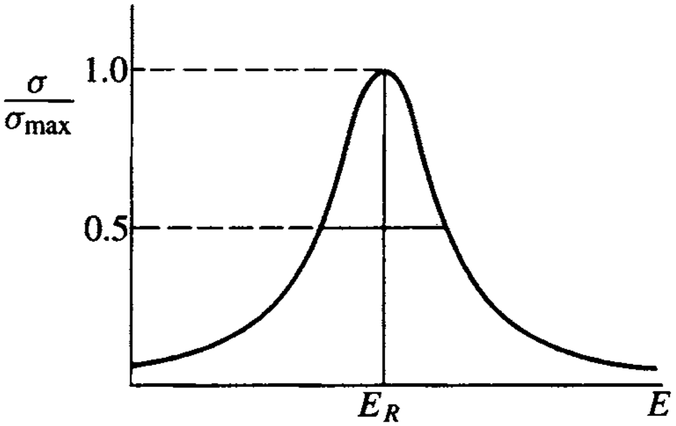

Figure 6.1: From [58], the Breit-Wigner resonance centered at the energy of the resonance E_R (= M).

Due to the quantum mechanical nature of resonances, they may interfere coherently or incoherently. A coherent sum involves the mixing of two or more resonances which make for a more involved energy-dependent cross section lineshape than just the single Breit-Wigner form. In the case of the Y(4260) parameterization by the

Belle experiment, its decay to $\pi^+\pi^- J/\psi$ is described by the interference of a Y(4008) in addition to a Y(4260) resonance. This coherent sum is incoherently summed with a third resonance for $\psi'(3686)$ which strongly decays into $\pi^+\pi^- J/\psi$. The resulting energy-dependent cross section is denoted in this analyis as σ_{BELLE}. The form and parameters of σ_{BELLE} are given in Equation 6.9 and Figure 6.2, respectively

$$\sigma_{\text{BELLE}} \propto |BW(M_{\psi(3686)}, \Gamma_{\psi(3686)})|^2 + |BW(M_1, \Gamma_1) + BW(M_2, \Gamma_2)|^2 \tag{6.9}$$

where BW is of Lorentz invariant form Eqn 6.6.

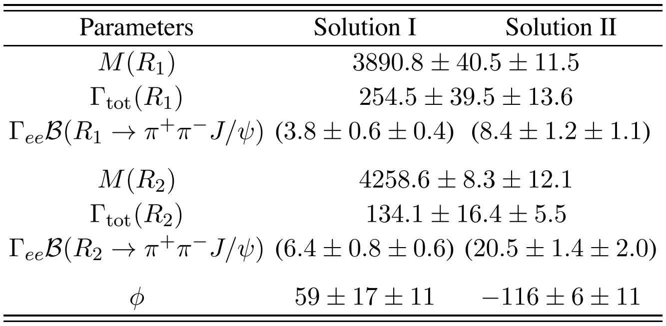

Parameters	Solution I	Solution II
$M(R_1)$	$3890.8 \pm 40.5 \pm 11.5$	
$\Gamma_{\text{tot}}(R_1)$	$254.5 \pm 39.5 \pm 13.6$	
$\Gamma_{ee}\mathcal{B}(R_1 \to \pi^+\pi^- J/\psi)$	$(3.8 \pm 0.6 \pm 0.4)$	$(8.4 \pm 1.2 \pm 1.1)$
$M(R_2)$	$4258.6 \pm 8.3 \pm 12.1$	
$\Gamma_{\text{tot}}(R_2)$	$134.1 \pm 16.4 \pm 5.5$	
$\Gamma_{ee}\mathcal{B}(R_2 \to \pi^+\pi^- J/\psi)$	$(6.4 \pm 0.8 \pm 0.6)$	$(20.5 \pm 1.4 \pm 2.0)$
ϕ	$59 \pm 17 \pm 11$	$-116 \pm 6 \pm 11$

Figure 6.2: From [50], the fit from Belle of the $\pi^+\pi^- J/\psi$ mass spectrum with two coherent resonances.

6.2 Experimental cross section

An experiment like BESIII is designed to reconstruct charged and neutral particles in discrete time slices known as an event. The total number of events (N) for a specific process to be reconstructed is proportional to the cross section (σ) and luminosity (L). In an experiment the quantity measured is the visible cross section or

$$\sigma_{\text{vis}} = \frac{N}{L}. \tag{6.10}$$

In every e^+e^- collision there is some probability one or several photons are spontaneously radiated just before annihilation which is known as initial state radiation (ISR). The lower the center-of-mass energy caused by the radiated photons make the visible cross section dependent on the Born cross section at all energies below the nominal e^+e^- center-of-mass energy $2E_0$. The ISR correction factor $1 + \delta_{isr}$ is used correct the visible cross section, more on these calculations is presented in the next section 6.2.1. The reconstruction efficiency is estimated with signal MC, which models the production and decay processes. If the decay involves intermediate states such as an η, π^0, or K_S then the branching fraction of those decays must also be accounted for. The Born cross section from e^+e^- annihilation is

$$\sigma = \frac{N_{sig} - N_{bg}}{\mathcal{L}\epsilon(1+\delta_{isr})(1+\delta_{vac})\sum_i \mathcal{B}_i} \tag{6.11}$$

where N_{sig}, N_{bg} are the number of reconstructed signal and background events, respectively; $\mathcal{L}$ is the integrated luminosity; ϵ is the reconstruction efficiency; $(1+\delta_{isr})$ is the ISR correction factor; $(1+\delta_{vac})$ is the vacuum polarization; $\sum_i \mathcal{B}_i$ is the sum of branching fractions to account for sequential decays. The vacuum polarization term is the effective screening induced by the vacuum induced by the electron and positron charge. Table 6.1 lists the vacuum polarization calculated at center of mass energies between 4.0-4.6 GeV [15] and is independent of final state reaction of the e^+e^- beams. The production mechanism is especially important in e^+e^- experiments since energy dependent initial state radiation (ISR) effects are expected. We will use the Y(4260) to illustrate the techniques for measuring e^+e^- cross sections at charmonium energies at B-factories and at BESIII.

$\sqrt{s}$(GeV)	4.090	4.190	4.210	4.220	4.230	4.245	4.260	4.310	4.360	4.390	4.420	4.470	4.530	4.600
$1+\delta_{vac}$	1.052	1.056	1.057	1.057	1.056	1.056	1.054	1.052	1.051	1.051	1.053	1.055	1.055	1.055

Table 6.1: Calculation of the vacuum polarization based on Fred Jegerlehner's alphaQED.

6.2.1 via initial state radiation

A B-factory is an e^+e^- accelerator facility designed to collide beams above 10 GeV, the threshold for $b\bar{b}$ quarkonium. The only planned B-factory experiment is Belle II, located in Tsukuba, Japan, which is an upgrade to their earlier Belle experiment where the $Y(4260)$ and $Y(4360)$ states were confirmed. Another B-factory experiment, BaBar, was operational until 2008 but is still actively analyzing data. BaBar was located at the Stanford Linear Accelerator Collider (SLAC), where the J/ψ and the $\psi'(3686)$ were discovered. B-factories are designed with high luminosity and excellent particle identification systems and have demonstrated the ability to select ISR events where the electron or positron beam emit a photon and collide at lower center of mass energy. One benefit of this ISR tagging technique is the study of resonances below the design energies. In studies of $e^+e^-(\gamma_{\text{ISR}}) \to \pi\pi J/\psi$ at center of mass energies near 4.26 GeV the Y(4260) was discovered at BaBar and confirmed by Belle using this ISR tagging technique.

In the ISR process, $e^+e^-(\gamma_{\text{isr}}) \to X$, the energy radiated by the photon (E_γ) results in a hadronic system with invariant mass $m = \sqrt{s(1-x)}$, where $\sqrt{s}$ is the e^+e^- center of mass and $x = 2E_\gamma/\sqrt{s}$ [36]. The mass spectrum of such an ISR process is related to the $e^+e^- \to X$ cross section by

$$\frac{d^2\sigma(e^+e^-(\gamma_{\text{isr}}) \to X)}{dx d\cos\theta_\gamma} = W(s, x, \theta_\gamma)\sigma(m) \tag{6.12}$$

where W is the well-known radiator function which describes the ISR energy and angular distribution [37]. The distribution of ISR photons is peaked along the direction of the e^+e^- beam.

The fit to the $\pi\pi J/\psi$ final state in the Belle data is shown in Figure 6.3 (a). The data was fit according to Eqn 6.9. The resulting energy-dependent cross section is shown in Figure 6.3 (b).

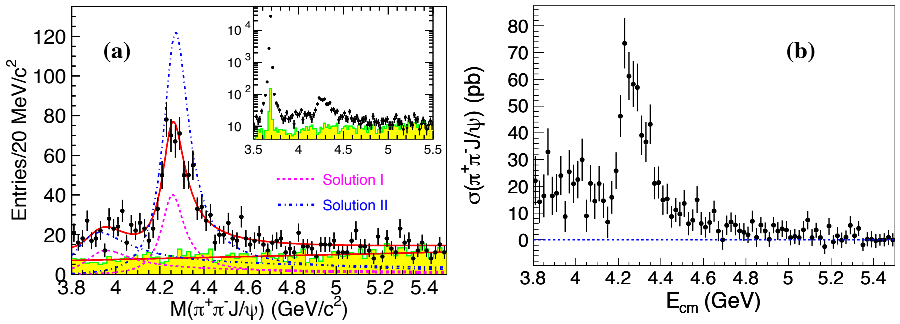

Figure 6.3: From [50], the invariant mass of $\pi^+\pi^-J/\psi$ between 3.8-5.6 GeV measured by the Belle Collaboration. (a) The solid curve shows the best total fit to the mass spectrum. The dotted lines represent the two equivalent solutions to the fit. (b) The cross section of $e^+e^- \to \pi^+\pi^-J/\psi$ after background subtraction.

6.2.2 via direct processes

To calculate a cross section from direct e^+e^- annihilation we must adjust the measurement to account for vacuum polarization and initial state radiation effects. The only e^+e^- facility capable of directly producing charmonium-like vector states is BESIII. The XYZ program at BESIII includes six high-integrated luminosity and over forty low-integrated luminosity data sets at energies between 4.0-4.6 GeV. Just as at B-factories, ISR collisions of e^+e^- beams also occur which will impact the reconstruction efficiency. This process can be calculated to separate the intended process where e^+e^- annihilate into a resonance from processes where either e^+e^- beam radiates a photon just before colliding. The angular distribution of the radiative photon can be integrated out in Eqn 6.12 to yield a radiator function only dependent on the center of mass energy squared (s) and the fractional energy carried by the ISR photon x to yield $W(s,x)$. If we fix s then the number of events given a cross section σ, efficiency ϵ, and luminosity $\mathcal{L}$ which incorporates the radiator function is given by

$$N = \mathcal{L} \int_0^1 \sigma(x)\epsilon(x)W(x)dx \tag{6.13}$$

where $x = 2E_\gamma/\sqrt{s}$. From the definition of N, the number of events, given in Eqn 6.13 we can define the reconstruction efficiency as

$$\begin{aligned}\epsilon &= \frac{N_{\mathrm{REC}}}{N_{\mathrm{GEN}}} \\ &= \frac{\mathcal{L}_{\mathrm{MC}} \int_0^1 \sigma(x)\epsilon(x)W(x)dx}{\mathcal{L}_{\mathrm{MC}} \int_0^1 \sigma(x)W(x)dx}\end{aligned} \tag{6.14}$$

An ISR correction factor $(1+\delta_{isr})$ accounts for the impact of ISR. The ISR correction factor is concerned with the shape of the ISR process and not the absolute magnitude. This is expressed in Equation 6.15 below

$$1 + \delta_{isr} = \int_0^1 \frac{\sigma(x)}{\sigma_0} W(s,x)dx \tag{6.15}$$

where the angular distribution of the radiative photon is incorporated into the radiator function $(W(s,x))$, $\sigma(x)$ is the assumed energy-dependent cross section, and σ_0 is the cross section at a fixed energy. The ISR correction factor for a given assumed lineshape is independent of the specific decay channel.

The reconstruction efficiency ϵ in Eqn 6.14 and the ISR correction factor $1 + \delta_{isr}$ can all be modeled in KKMC. KKMC offers a simple interface for uploading custom energy dependent lineshape assumptions to model the ISR with.

Chapter 7

Analysis of $\mathbf{e^+e^-} \to \gamma\eta_\mathbf{c}(\mathbf{1S})$

In this dissertation we measure the Born cross section for the process $e^+e^- \to \gamma\eta_c(1S)$ by reconstructing the transition photon and $\eta_c(1S)$ in twelve decay channels. The branching fractions for each of these $\eta_c(1S)$ decay channels are shown in Table 7.1.

$\eta_c(1S) \to$	$2(\pi^+\pi^-\pi^0)$	$\pi^+\pi^-\pi^0\pi^0$	$2(\pi^+\pi^-\pi^+\pi^-)\eta$
Branching Fraction (%)	17.23 ± 1.70 ± 2.29	4.66 ± 0.50 ± 0.76	4.40 ± 0.86 ± 0.85
$\eta_c(1S) \to$	$K^+K^-\pi^+\pi^-\pi^0$	$3(\pi^+\pi^-)$	$2(\pi^+\pi^-)$
Branching Fraction (%)	3.50 ± 0.60	2.02 ± 0.36 ± 0.36	1.72 ± 0.19 ± 0.25
$\eta_c(1S) \to$	$\pi^+\pi^-\eta$	$K^{-\pm}K_S\pi^\mp\pi^+\pi^-$	$K^\pm K_S\pi^\mp$
Branching Fraction (%)	1.66 ± 0.34 ± 0.26	2.75 ± 0.51 ± 0.47	2.60 ± 0.29 ± 0.34
$\eta_c(1S) \to$	$K^+K^-\pi^0$	$\pi^+\pi^-K^+K^-$	$2(\pi^+\pi^-)K^+K^-$
Branching Fraction (%)	1.04 ± 0.17 ± 0.11	0.95 ± 0.17 ± 0.13	0.83 ± 0.39 ± 0.15

Table 7.1: The twelve $\eta_c(1S)$ decay channels reconstructed in this analysis. The branching fractions include their statistical and systematic error, if known. The channel $\eta_c(1S) \to$ is taken from its world average branching fraction and statistical error from the PDF [56]. In all other decay channels we use the BESIII measurements in Ref. [10] with their systematical error also included.

The size of the $\eta_c(1S)$ is determined by studying distributions of the recoil-mass of the transition photon. For a transition photon of energy E_γ and momentum of $\vec{P}_\gamma$

the recoil-mass of the transition photon, $RM(\gamma)$, is expressed below

$$RM(\gamma) = (\sqrt{s} - E_\gamma)^2 - (\sqrt{s}\sin(\theta) - P_{\gamma,x})^2 - P_{\gamma,y}^2 - P_{\gamma,z}^2 \tag{7.1}$$

where $\sqrt{s}$ is the center of mass energy and θ is the e^+e^- beam crossing angle. The coordinate system of the reconstructed particle momentum and positions is centered at the interaction point with the x-axis (y-axis) aligned in the horizontal (vertical) direction. An example distribution of the recoil-mass of the transition photon using MC which models the decay $\eta_c(1S) \rightarrow 2(\pi^+\pi^-\pi^0)$ is shown in the left plot of Figure 7.1. How signal MC is generated will be discussed in section 7.1.1.

If we plot the recoil-mass of the transition photon in data for the $\eta_c(1S) \rightarrow 2(\pi^+\pi^-\pi^0)$ channel and blind the $\eta_c(1S)$ mass region we get the right plot of Figure 7.1. Evident in this figure is a prominent distribution that peaks at 3.1 GeV, due to initial state radiation (ISR) background from the process $e^+e^-(\gamma_{isr}) \rightarrow J/\psi$, on top of a smooth distribution explained by the continuum process $e^+e^- \rightarrow q\bar{q}$. The generation of the MC that models these backgrounds will be discussed in this chapter. In section 7.1.2 background MC is generated that models the continuum, QED, and open charm processes. In section 7.1.3 we discuss the generation of the J/ψ ISR MC.

The event selections used to produce Figure 7.1 are discussed in sections 7.2.1 and 7.2.2. As a final data processing step we select only one combination of a can-

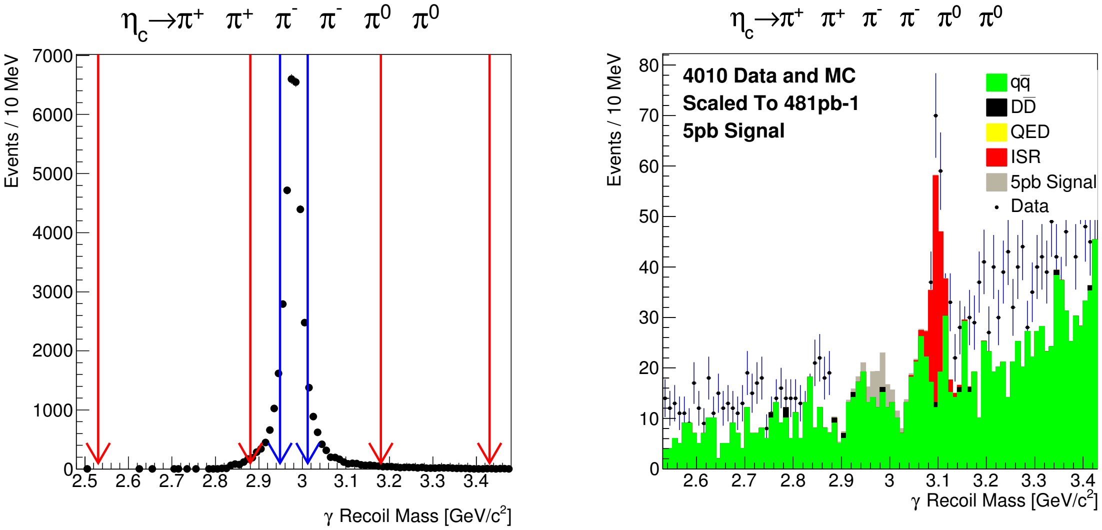

Figure 7.1: The distribution of the recoil-mass of the transition photon for the channel $\eta_c(1S) \to 2(\pi^+\pi^-\pi^0)$. (Left) The sideband (between the red lines) and signal (between the blue lines) regions used in figure-of-merit calculation. (Right) The data (in points) is superimposed on the MC after event selections and removal of multiple counting.

didate final states in every event, thus removing multiple counting. The method for selecting the best combination is discussed in section 7.2.3. In section 7.2.4 the recoil-mass of the transition photon in MC and data for each $\eta_c(1S)$ decay channel after event selection and removal of multiple counting is presented. To prevent bias in our measurement the data is blinded in the signal region.

Once we have our event selections and have a procedure in place for removing multiple counted events we can then learn from MC. If are interested in the components necessary to make the $\sigma_E(e^+e^- \to \gamma\eta_c(1S))$ measurement we can use signal MC to learn the reconstructions efficiency and the mass resolution of the $\eta_c(1S)$ from detector effects (7.3.1). In addition, with signal MC we study the contamination from reconstructing cross feed $\eta_c(1S)$ decay channels (7.3.2).

In section 7.4 the following J/ψ ISR processes are studied: $J/\psi \to X_i$ and $J/\psi \to \gamma\eta_c(1S), \eta_c(1S) \to X_i$ where X_i is an $\eta_c(1S)$ decay channel from Table 7.1. In section 7.4.1 the shape of the $J/\psi \to X_i$ is studied with MC and used to fix the shape of the J/ψ component of the fit discussed in the next chapter. In section 7.4.2 the size of the $e^+e^-(\gamma_{isr}) \to J/\psi$ background is measured and compared to theoretical calculations as a test of our fitting procedure. In section 7.4.3 the contamination of peaking background from $J/\psi \to \gamma\eta_c(1S)$ is estimated.

In the next next chapter we will present the $e^+e^- \to \gamma\eta_c(1S)$ Born cross section measurement.

7.1 MC samples

Just as the decay of a resonance is a probabilistic process, so is the generation of toy data commonly known as MC. The details of the MC generators used at BESIII were presented in Chapter 4. In this section we present an overview of the types and sizes of MC samples generated for this analysis.

7.1.1 Signal MC

Signal MC is generated with KKMC to describe the signal process $e^+e^- \to \gamma\eta_c(1S)$ including any intermediate states such as decays of π^0, η, or K_S. In generating these MC samples we do not assume any substructure in $\eta_c(1S)$ decays. For instance, the decay $\eta_c(1S) \to K^+K^-\eta$ and $\eta_c(1S) \to f_2'\eta, f_2' \to K^+K^-$ yield the same final state, but we do not account for the latter possibility. Instead we estimate the size of this effect and include a systematic error for it in the Born cross section measurement, see Chapter 9.3. The KKMC event generator is responsible for modeling the physics of the e^+e^- beam just before annihilation including any ISR process. The ISR processes studied in this analysis are the same as the assumed energy-dependent cross section used to combine data at all energies, see Chapter 8. The ISR process are: σ_{FLAT}, σ_{BELLE}, $\sigma_{\mathrm{Y(4260)}}$, and $\sigma_{\mathrm{Y(4360)}}$. In addition, we also generate MC assuming there is no ISR. The total number of $\eta_c(1S)$ generated was 1×10^6 for each ISR and energy combination.

The mass resolution measured by our detector will smear out the true width of any resonance. This is due to errors in measurements of a particles position, momentum, or energy. To determine the shape of the detector resolution we set the $\eta_c(1S)$ full width to zero and generate 1×10^6 signal MC for every ISR and energy combination. When we reconstruct the final states and plot distributions of the recoil-mass of the transition photon any width at the $\eta_c(1S)$ mass is due to effects of the detector.

7.1.2 Background MC

While any decay reconstructed in $e^+e^- \to \gamma\eta_c(1S)$ is background, we will make a distinction between those background that come from the ISR process $e^+e^-(\gamma_{isr}) \to J/\psi$ and all other backgrounds. This section is concerned with the latter or background processes from continuum ($e^+e^- \to q\bar{q}$), QED ($e^+e^- \to l^+l^-$), and open charm ($e^+e^- \to D\bar{D}$) processes. The continuum background is the result of the $q\bar{q}$ pairs pulling apart and beginning the hadronization process. The fragmentation of $q\bar{q}$ into pions, kaons, and other light mesons form a substantial background in many of this analysis's final state channels.

The cross section for these backgrounds drops with increasing center-of-mass energy according to $1/s$, where s is the center-of-mass energy squared. This allows us to optimize our event selections at 4.01 GeV and apply those same selections to data collected at higher center-of-mass energies. The theoretical cross section for the continuum and QED process are shown in the third column of Figure 7.2. The last column shows the number of events generated for each process. The equivalent luminosity for each process, except $e^+e^- \to e^+e^-$, is 479 pb^{-1}. The background from Bhabha scattering is very large so only a 23 pb^{-1} equivalent luminosity is generated for it.

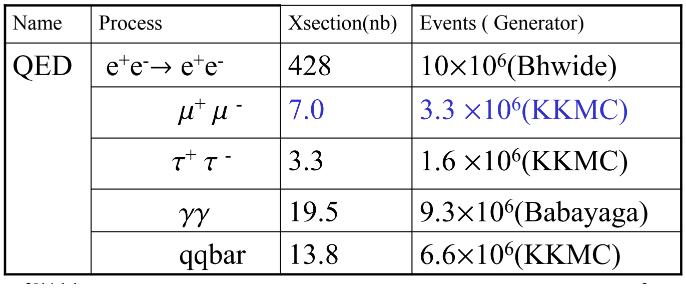

Name	Process	Xsection(nb)	Events (Generator)
QED	$e^+e^- \to e^+e^-$	428	10×10^6(Bhwide)
	$\mu^+\mu^-$	7.0	3.3×10^6(KKMC)
	$\tau^+\tau^-$	3.3	1.6×10^6(KKMC)
	$\gamma\gamma$	19.5	9.3×10^6(Babayaga)
	qqbar	13.8	6.6×10^6(KKMC)

Figure 7.2: The rates of the generated background processes at 4.01 GeV with an equivalent integrated luminosity of 478 pb^{-1}.

7.1.3 J/ψ ISR MC

Another background process which is further studied at the end of this chapter comes from ISR e^+e^- collisions which produce a J/ψ. Two possible types of J/ψ decays are important for this analysis since they could either contaminate the signal or show up as a large peak about 100 MeV away from the $\eta_c(1S)$ in recoil mass distributions of the transition photon. A total of 1×10^6 J/ψ events are generated for the two J/ψ

decay types and at each energy.

In distributions of the transition photon recoil mass in data a clear J/ψ peak is observed in most of the candidate $\eta_c(1S)$ final states analyzed due to the process $e^+e^-(\gamma_{isr}) \rightarrow J/\psi, J/\psi \rightarrow X_i$, where X_i is a decay channel of $\eta_c(1S)$. The MC generated to study this process plays a role in describing the shape of the J/ψ distribution, which ultimately reduces the number of free parameters in our fit. In addition, we use the reconstruction efficiency estimated with this MC to simultaneously measure the $e^+e^- \rightarrow \gamma\eta_c(1S)$ and $e^+e^-(\gamma_{isr}) \rightarrow J/\psi$ cross section from data. Since this ISR process can be calculated to good precision we can compare it to the experimental cross section and validate our fitting technique, see section 7.4.1.

The background that contaminates the $\eta_c(1S)$ signal is generated by the following process, $e^+e^-(\gamma_{isr}) \rightarrow J/\psi, J/\psi \rightarrow \gamma\eta_c(1S), \eta_c(1S) \rightarrow X_i$, where X_i is a decay channel of $\eta_c(1S)$. The KKMC event generator is used to estimate the size of this contamination, which we found to be negligible, see section 7.4.3.

7.2 Event Selection

The event selection procedure is presented in two stages: a stage with loose constraints on PID and kinematic fitting which represent the standard event selection criterium used in many analyses and a stage that uses the sidebands in data and MC to estimate the backgrounds in the signal region which attempt to optimize the event selections.

The cross sections for continuum and QED background are expected to decrease at higher center-of-mass energies according to $1/\sqrt{s}$. We, therefore, assume event selections optimized at 4.01 GeV to hold for all energies up to 4.60 GeV.

7.2.1 Standard

The MDC cannot measure tracks in the beam pipe which excludes 7% of the detector volume. Charged pions and kaons are reconstructed in regions where their angles with respect to the beam direction, θ, must satisfy $|\cos\theta| < 0.93$. Except for pions originating from K_S decays, all charged tracks are further required to pass within 10 cm of the interaction point along the beam direction and within 1 cm in a plane perpendicular to the beam.

Pions and kaons are separated using a combination of ionization energy loss in the MDC and timing information from the TOF. For each reconstructed track, particle identification probabilities P_π and P_K are calculated based on pion and kaon hypotheses, respectively. For pions, we require $P_\pi > 10^{-5}$; for kaons, we require $P_K > 10^{-5}$. At this stage of the event selection we do not include any additional track hypothesis requirements, however, requiring $P_K > P_\pi$ is used to reduce combinatoric background, see Section 7.3.

The $\pi^+\pi^-$ candidate daughter particles of the K_S must come from a common space point which forms a secondary vertex with respect to the interaction point. A

K_S candidate is selected if the invariant mass of $\pi^+\pi^-$ pairs at the secondary vertex satisfy $471 < M(\pi^+\pi^-) < 524$ MeV/c^2.

The gaps between the barrel and end cap regions of the BESIII detector, to make room for piping and cables, imposes fiducial constraints on where a particle can be reconstructed in the TOF and EMC. Photons are reconstructed in the EMC by clustering energies deposited in individual crystals. Energy clusters in the barrel region ($|\cos\theta| < 0.8$) must be greater than 25 MeV and they must be greater than 50 MeV in the end cap region ($0.86 < |\cos\theta| < 0.92$). Timing from the EMC is used to reduce electronic noise and background from unrelated events.

We form π^0 and η candidates using combinations of two photons whose invariant mass satisfy $107 < M(\gamma\gamma) < 163$ MeV/c^2 for the π^0 and $400 < M(\gamma\gamma) < 700$ MeV/c^2 for the η.

Table 7.2 summarizes the standard event selection criterium.

7.2.2 Optimized

From the initial lists of γ, $\pi^\pm$, $K^\pm$, π^0, η, and K_S, we form all possible combinations of γX_i for each i. We perform a kinematic fit for each of these combinations to the initial four-momentum of the center-of-mass system (4C) and add one constraint (1C) for the mass of every π^0, η, and K_S candidate. We require that the resulting χ^2/dof be less than a value optimized separately for each X_i. The candidate transition

Cut	Value
Track Selection	$Prob(e^{\pm}, \mu^{\pm}, \pi^{\pm}, K^{\pm}) > 10^{-5}$ Track corrections have also been applied
Photon Selection	E > 25 MeV (barrel) E > 50 MeV (end cap) 0 < TDC < 14
π^0/η, Selection	For π^0: 0.107 < mass($\gamma\gamma$) < 0.163 GeV/c^2 For η: 0.400 < mass($\gamma\gamma$) < 0.700 GeV/c^2 $\gamma\gamma$ events constrained to π^0/η mass (1C) $\chi^2_{\pi^0,\eta} < 2500$
K_S Selection	0.471 < mass($\pi^+\pi^-$) < 0.524 GeV/c^2 $\pi^+\pi^-$ events constrained to K_S mass and fit to displaced vertex (1C) $\chi^2 < 100$

Table 7.2: The event selections applied to every reconstructed channel of $\eta_c(1S)$.

photon is paired with all other energy clusters in an event; candidates that form a pair consistent with originating from a π^0 are rejected. The candidate transition photon in the $\gamma\pi^+\pi^-\eta$ channel is isolated from clusters formed by charged tracks by requiring their angle of separation be greater than 17.5°. To avoid multiple counting, we only use the combination with the best χ^2/dof, see Section 7.3.

The optimization procedure is applied to those selection criterium which offer the greatest discrimination of signal from background. The strength of an event selection is varied to search for the maximum combination of $N_s/(N_s + N_b)$ or figure of merit, where N_s is the number of signal and N_b is the number of background. Signal is studied with MC that models the production and sequential decay process of $\gamma\eta_c(1S)$. Reconstructed events that fall within a mass region, in distributions of the recoil-mass of the transition photon, centered around the $\eta_c(1S)$ mass and a window $\pm 2\Gamma$ are counted as N_s. To avoid relying on MC to correctly model the background process we also include data in our study of the background.

We know of the large ISR background due to $e^+e^-(\gamma_{ISR}) \rightarrow J/\psi$ but this can be modeled with MC and accounted for. For this reason we don't want to include ISR as a background for the figure of merit. To avoid ISR we select asymmetric sidebands. The number of background in the signal region (N_b) is related to events fall in either the low or high mass sideband regions. The signal and sideband regions are defined below

Signal region: $|\gamma_{\text{recoil mass}} - \text{mass}_{\eta_c(1S)}| < 2 \times \Gamma(\eta_c(1S))$

Low Mass Sideband: $-450MeV < \gamma_{\text{recoil mass}} - \text{mass}_{\eta_c(1S)} < -100MeV$

High Mass Sideband: $200MeV < \gamma_{\text{recoil mass}} - \text{mass}_{\eta_c(1S)} < 450MeV$

The number of background in the signal region is estimated from sidebands as

$$N_b = \frac{L_S}{2}(\frac{N_l}{L_l} + \frac{N_h}{L_h}) \tag{7.2}$$

where L_S is the signal mass region, L_l (L_h) is the low (high) mass sideband window and N_l (N_h) is the number of background events that in the low (high) mass sideband window.

The reaction $e^+e^- \to \gamma\eta_c(1S)$ has not been measured before this analysis, therefore, we study the figure of merit for a 1 and 10 pb assumed Born cross section. This yields four ways to combine the signal and background to calculate a figure of merit. The final event selection is averaged from these four combinations.

The various background processes are modeled in MC at 4.01 GeV with an equivalent integrated luminosity of 478 fb^{-1}. This is on par with the data collected around 4.01 GeV.

We illustrate in Figures 7.3 and 7.4 the optimization process for two typical decays of $\eta_c(1S)$. One is $\gamma\pi^+\pi^+\pi^-\pi^-\pi^0\pi^0$ which involves only final state pions and the other, $\gamma K^- K_S \pi^+$, involves a mix of kaons and pions.

The figure of merit for varying the χ^2/d.o.f for the $\gamma\pi^+\pi^+\pi^-\pi^-\pi^0\pi^0$ final state is shown in Figure 7.3 (a). The best χ^2/d.o.f is the average of the maximum figure of merit for each background and signal combination.

A common background in final states with a π^0 is when a candidate transition photon is mistaken for a daughter photon of a π^0 candidate. To remove these backgrounds we pair the transition photon with all other energy clusters in an event. Candidates that form a pair consistent with originating from a π^0 are rejected, see Figure 7.3 (b).

Charged particles can also deposit energy into the EMC and be mistaken as a photon. The figure of merit calculated as a function of separation angle between charged tracks and candidate transition photon clusters is shown in Figure 7.3 (c). The final state $\gamma\pi^+\pi^-\eta$ is the only channel that benefits from this selection. The angle of separation is required to be greater than 17.5°, see Appendix B.

We also investigate selecting K_S candidates based on the distance of the K_S vertex with respect to the interaction point. As shown in Figure 7.4 (d), their is no indication that requiring a constraint on the K_S decay length over error significantly improves the signal yield.

The flow of the optimization procedure is in order from most to least significant event selection. This is presented from left to right in Figure 7.3 and 7.4. Appendix B shows optimization flow for each final state and the final event selection from the optimization routine.

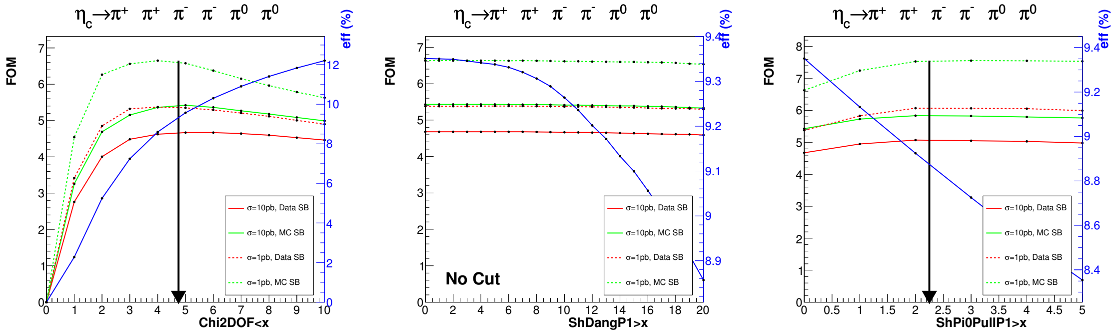

Figure 7.3: The $\eta_c(1S) \to \pi^+\pi^-\pi^+\pi^-\pi^0\pi^0$ figure of merit for different event selections. (a) Figure-of-merit of the kinematic fit, (b) Figure-of-merit of angle between shower and closest charged track, (c) Figure-of-merit of rejecting the π^0 candidates formed with a transition photon.

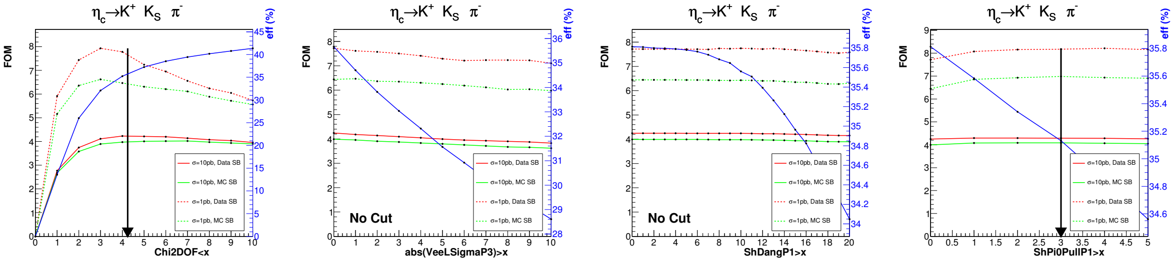

Figure 7.4: The $\eta_c(1S) \rightarrow K^+K_S\pi^-$ figure of merit for different event selections. (a) Figure-of-merit of the kinematic fit, (b) Figure-of-merit of the K_S decay length divided by its error , (c) Figure-of-merit of angle between shower and closest charged track , (d) Figure-of-merit of rejecting the π^0 candidates formed with a transition photon.

The final selection criterium for each final state is shown in Table 7.3.

7.2.3 Multiple counting

The list of candidate final state particles can be combined to form a specific intermediate state. We consider all combinations while avoiding double counting. The last data processing step in this analysis involves selecting the best combination as determined by it kinematic χ^2/d.o.f.

7.2.4 Mass distributions

The recoil-mass distribution of the transition photon after final event selection criteria for each final state at 4.01 GeV and 4.26 GeV is shown in Figure 7.5 and 7.6. The MC

$\eta_c(1S)$ Modes	χ^2/d.o.f <	Dang >	π^0 Pull >	PID
$\pi^+\pi^+\pi^-\pi^-\pi^0\pi^0$	4.75	-	2.25	-
$\pi^+\pi^-\pi^0\pi^0$	4.00	-	3.25	-
$\pi^+\pi^+\pi^-\pi^-\eta$	3.50	-	3.50	-
$K^+K^-\pi^+\pi^-\pi^0$	3.25	-	2.50	ProbK>Probπ (Both kaons)
$\pi^+\pi^+\pi^+\pi^-\pi^-\pi^-$	5.20	-	1.50	-
$\pi^+\pi^+\pi^-\pi^-$	3.50	-	1.75	-
$\pi^+\pi^-\eta$	3.00	17.5	4.00	-
$K^-K_S\pi^+\pi^+\pi^-$	4.25	-	1.75	ProbK>Probπ
$K^+K_S\pi^+\pi^-\pi^-$	4.00	-	2.00	ProbK>Probπ
$K^-K_S\pi^+$	3.75	-	3.25	ProbK>Probπ
$K^+K_S\pi^-$	4.25	-	3.00	ProbK>Probπ
$K^+K^-\pi^0$	2.75	-	2.75	ProbK>Probπ
$K^+K^-\pi^+\pi^-$	3.00	-	1.50	ProbK>Probπ (Both kaons)
$K^+K^-\pi^+\pi^+\pi^-\pi^-$	4.00	-	2.50	ProbK>Probπ (Both kaons)

Table 7.3: Summary of final event selections for each $\eta_c(1S)$ decay channel. A dashed line indicates the final event selection does not use this criterium.

is scaled to 470 pb^{-1} at 4010 MeV and 825 pb^{-1} at 4260 MeV. The ISR background, in red, is modeled with KKMC scaled by the number of J/ψ in data. The signal MC, in grey, is scaled to a 10 pb production cross section. Superimposed in the plots is the distribution in data with the signal region screened. At 4.010 MeV the MC does an excellent job modeling data in the sidebands but at 4.260 MeV $\eta_c(1S)$ decay modes involving only pions are modeled very poorly. This does not impact the event selection since only 4010 MeV data and MC sidebands were used.

The χ^2/d.o.f after all event selection for data and signal MC is shown in Figure 7.7 on a log plot. The signal MC is scaled by a 10 pb production cross section and the 4.01 GeV luminosity.

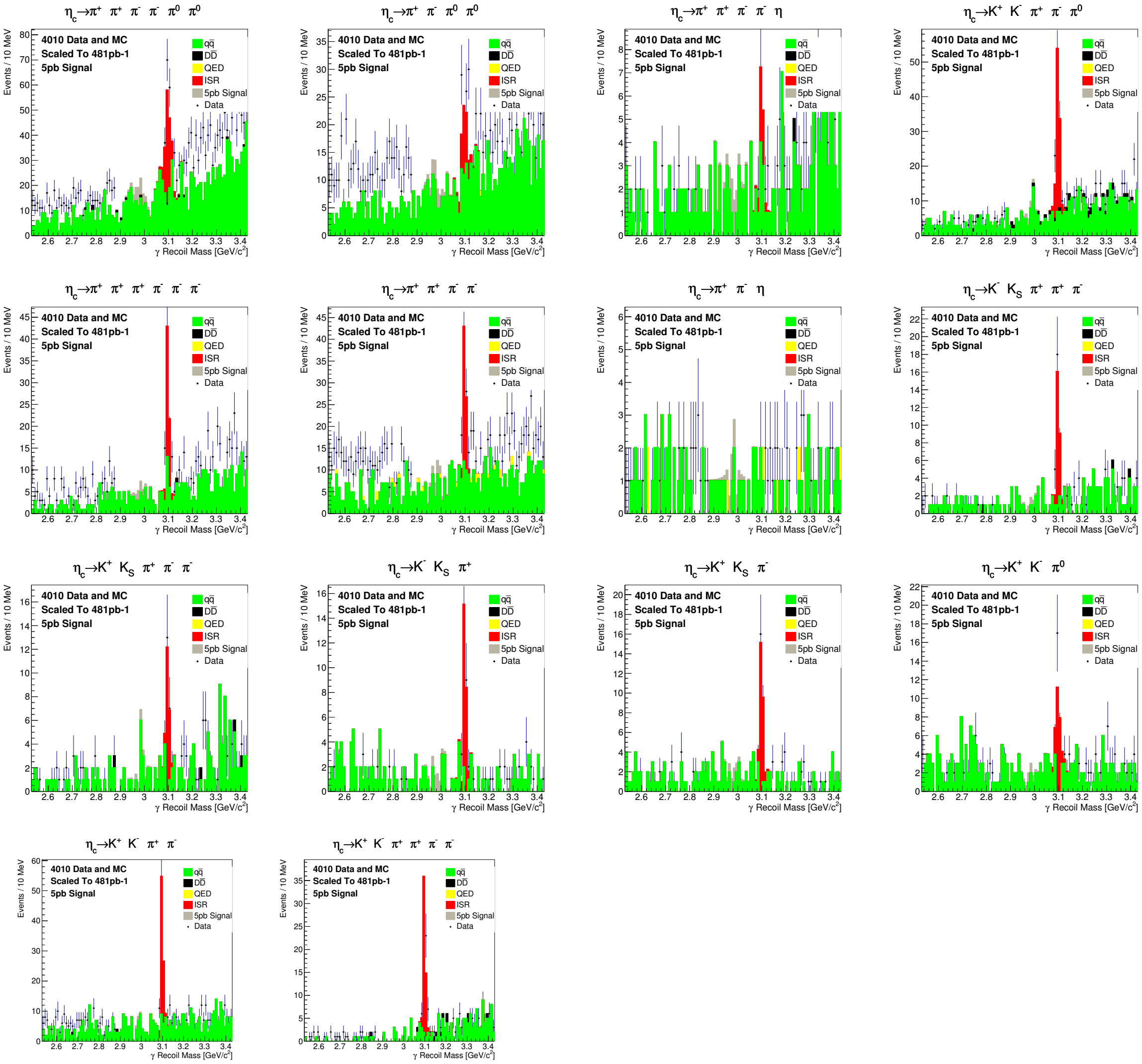

Figure 7.5: The recoil mass distribution of the transition photon for each $\eta_c(1S)$ decay channel at center-of-mass energy 4.01 GeV assuming a 5 pb production cross section.

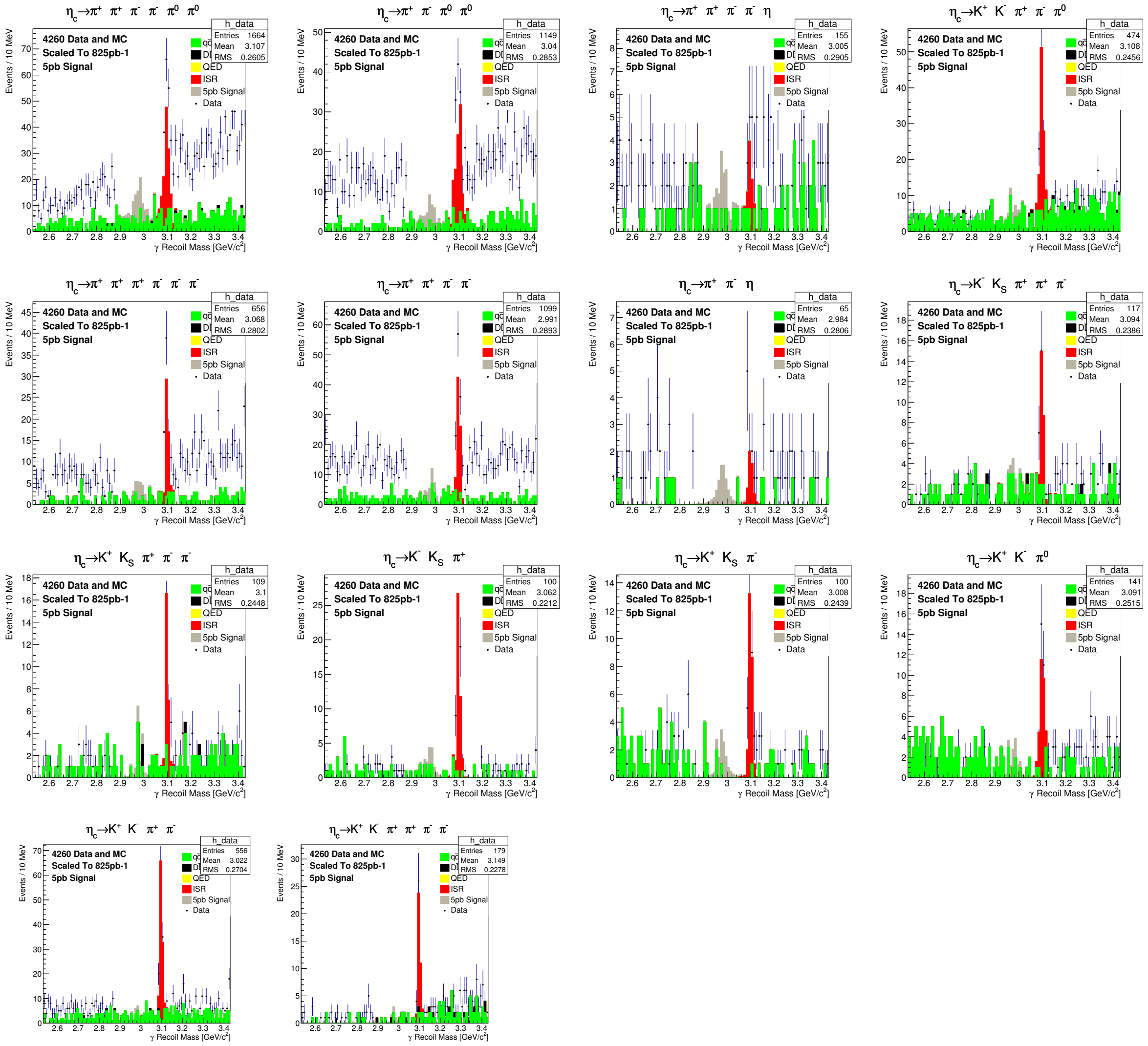

Figure 7.6: The recoil mass distribution of the transition photon for each $\eta_c(1S)$ decay channel at center-of-mass energy 4.26 GeV assuming a 5 pb production cross section.

7.3 Signal MC studies

In this section we use signal MC to estimate the reconstruction efficiency for $e^+e^- \to \gamma\eta_c(1S), \eta_c(1S) \to X_i$ at the six center-of-mass energies. In addition, we use signal MC to determine, for a candidate final state, the contamination from cross feed $\eta_c(1S)$ channels. These studies are performed after applying the final event selections listed in Table 7.3 with multiple counting removed.

7.3.1 Efficiency

The reconstruction efficiency for each final state is determined by fitting for the number of $\eta_c(1S)$ in recoil-mass distributions of the transition photon and dividing by the generated number of events. The product of the reconstruction efficiency with $(1 + \delta_{isr})$ for each $\eta_c(1S)$ decay channel are shown in Appendix B.

The signal can be described by a Breit-Wigner smeared with a channel-dependent detector resolution. The detector resolution is estimated with signal MC where the generated $\eta_c(1S)$ full width is set to zero. The mass and width of the Breit-Wigner in this fit are fixed to the values used in the MC. The only free parameter in the fit is the number of $\eta_c(1S)$. An example fit is shown on the right of Figure 7.8 for $\eta_c(1S) \to \pi^+\pi^+\pi^-\pi^-\pi^0\pi^0$.

On the left of Figure 7.8 we compare the detector resolution for the channel

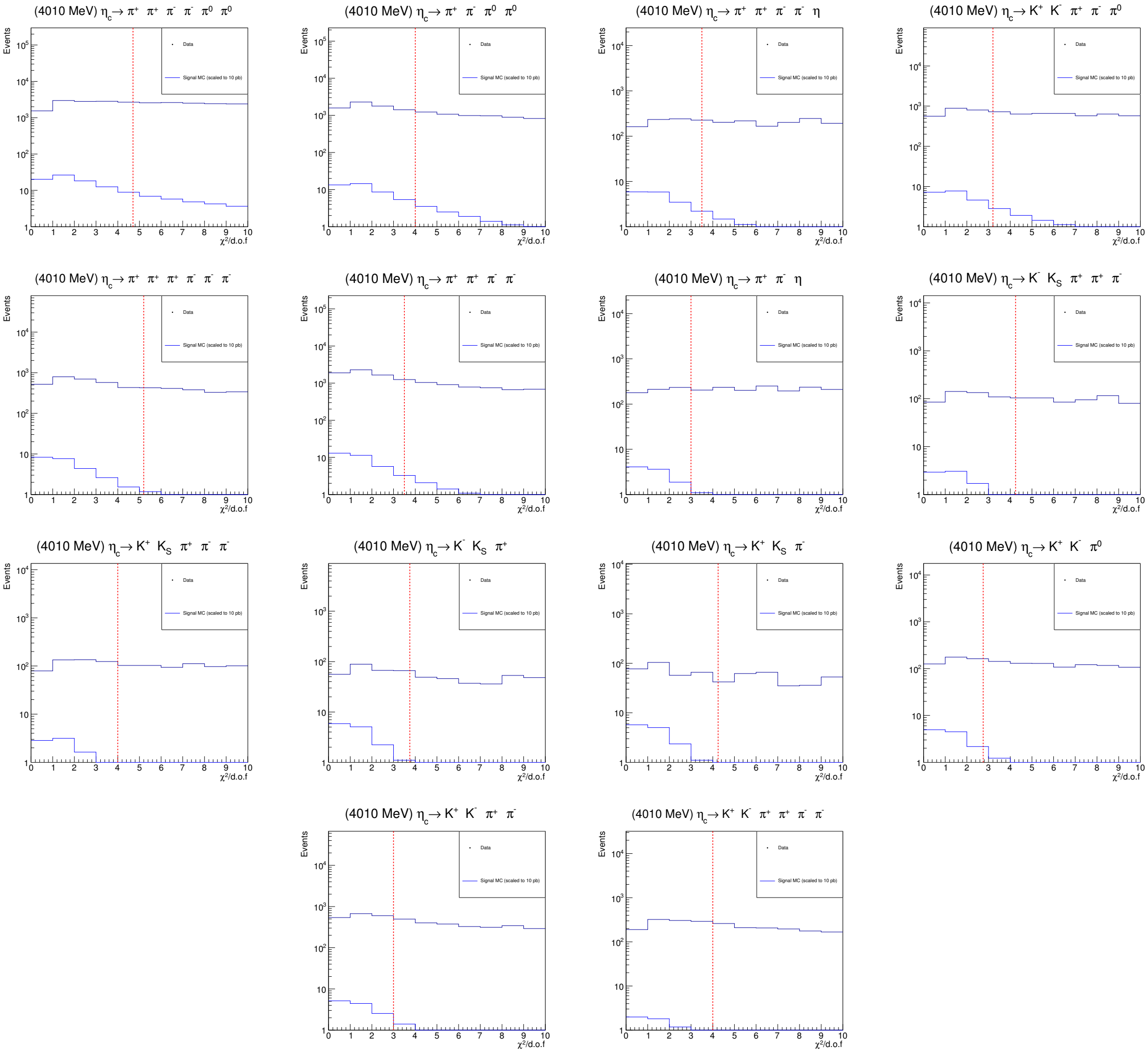

Figure 7.7: The χ^2/d.o.f of candidate events in data and signal MC at center-of-mass energy 4.01 GeV. The signal is scaled to a 10 pb production cross section. The red line is the constraint of the χ^2 which maximizes the figure-of-merit, see Table 7.3.

$\eta_c(1S) \to \pi^+\pi^+\pi^-\pi^-\pi^0\pi^0$ with and without ISR. Low energy ISR photons are more probable than high energy ISR photons making the detector resolution asymmetric in signal MC with ISR.

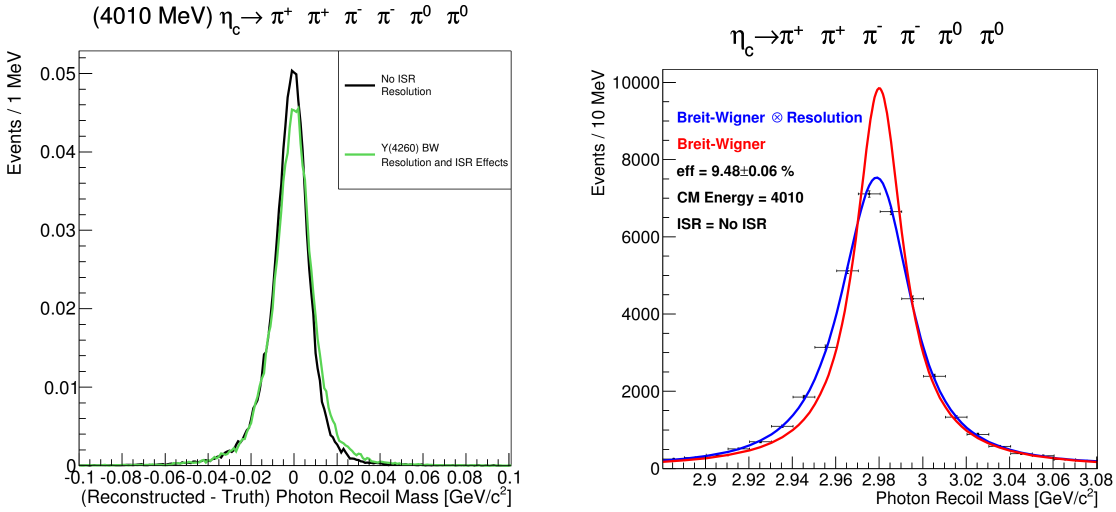

Figure 7.8: The $\eta_c(1S) \to \pi^+\pi^+\pi^-\pi^-\pi^0\pi^0$ resolution and fit in signal MC at center-of-mass energy 4.01 GeV. Left: Detector resolution with and without a Y(4260) ISR lineshape assumption. Right: Fit to signal MC with a Breit-Wigner with a fixed mass and width convolved with the detector resolution assuming ISR is turned off.

7.3.2 Cross feeds

We study the cross feeds in each $\eta_c(1S)$ decay channel by applying the selection criteria for mode i to mode j where $i \neq j$. The charged kaons in some $\eta_c(1S)$ channels can potentially be mistaken for a charged pion. By requiring $P_K > P_\pi$ we are able to significantly suppress the cross feeds in these channels. The largest cross feeds in each final state is kept below 1%, as shown in Table 7.4.

Generated	Largest Cross Feed	Amount of Cross Feed (%)
$\pi^+\pi^+\pi^-\pi^-\pi^0\pi^0$	$\pi^+\pi^+\pi^-\pi^-\eta$	0% / 0%
$\pi^+\pi^-\pi^0\pi^0$	$\pi^+\pi^-\eta$	0% / 0%
$\pi^+\pi^+\pi^-\pi^-\eta$	$\pi^+\pi^+\pi^-\pi^-\pi^0\pi^0$	0.1% / 0.1%
$K^+K^-\pi^+\pi^-\pi^0$	$\pi^+\pi^+\pi^-\pi^-\pi^0\pi^0$	0.0% / 0%
$\pi^+\pi^+\pi^+\pi^-\pi^-\pi^-$	$K^-K_S\pi^+\pi^+\pi^-$	0% / 0%
$\pi^+\pi^+\pi^-\pi^-$	$K^+K_S\pi^-$	0.3% / 0.4%
$\pi^+\pi^-\eta$	$\pi^+\pi^-\pi^0\pi^0$	0% / 0%
$K^-K_S\pi^+\pi^+\pi^-$	$K^+K_S\pi^+\pi^-\pi^-$	0.1% / 0%
$K^+K_S\pi^+\pi^-\pi^-$	$K^-K_S\pi^+\pi^+\pi^-$	0% / 0%
$K^-K_S\pi^+$	$K^+K_S\pi^-$	0.8% / 0.8%
$K^+K_S\pi^-$	$K^-K_S\pi^+$	0.8% / 0.8%
$K^+K^-\pi^0$	$\pi^+\pi^+\pi^-\pi^-\pi^0\pi^0$	0.0% / 0.0%
$K^+K^-\pi^+\pi^-$	$K^-K_S\pi^+$	0% / 0.1%
$K^+K^-\pi^+\pi^+\pi^-\pi^-$	$K^+K^-\pi^+\pi^-\pi^0$	0% / 0.0%

Table 7.4: Maximum cross feed determined with signal MC and after removal of multiple counted events for each $\eta_c(1S)$ decay channel. The cross feed is calculated for center-of-mass energies 4.01 and 4.26 GeV.

7.4 Initial State Radiation studies

With KKMC we can investigate the ISR process $e^+e^-(\gamma_{isr}) \to J/\psi, J/\psi \to X_i$ and $J/\psi \to \gamma\eta_c(1S), \eta_c(1S) \to X_i$, where X_i is an $\eta_c(1S)$ decay channel. The $J/\psi \to X_i$ process strongly peaks at the J/ψ mass or at about 3.1 GeV in distributions of the recoil-mass of the transition photon in many of our final states. This is unsurprising since many of our $\eta_c(1S)$ decay channels are also decays of J/ψ. In section 7.4.1 we estimate the shape of the J/ψ distribution with MC. In section 7.4.2 we measure the J/ψ ISR cross section in data. Furthermore, we compare the experimental J/ψ ISR cross section with that from theory and find good agreement, see Figure 7.10. In section 7.4.3 we use MC that models $J/\psi \to \gamma\eta_c(1S)$ and estimate the number of ISR events that contaminate the signal region. The MC is scaled according to the measured J/ψ ISR cross section.

7.4.1 $e^+e^-\gamma_{\text{isr}} \to J/\psi, J/\psi \to X$

We do expect a significant ISR background due to $e^+e^-(\gamma_{isr}) \to J/\psi$ since many of the $\eta_c(1S)$ decay channels are also decays of J/ψ. The theoretical width of the J/ψ is on the order of keV yet MC and data both show a much wider gaussian distribution centered at 3.1 GeV. The observed width of the J/ψ is a result of smearing the detector resolution with a narrow Breit-Wigner. The distributions of the recoil-mass of the transition photon the MC is described by a double Gaussian expressed below

$$N_{isr}(f \cdot \mathcal{N}(\mu_1, \sigma_1) + (1-f)\mathcal{N}(\mu_2, \sigma_2)) \tag{7.3}$$

where $\mathcal{N}$ is a Gaussian distribution. All parameters of the fit, except the number of ISR, are extracted from MC in each J/ψ final state and at each energy, see Figure 7.9. The shape in MC fixes the shape of the ISR in data. Differences in reconstructing MC and data make up a systematic uncertainty which is further discussed in Chapter 9.

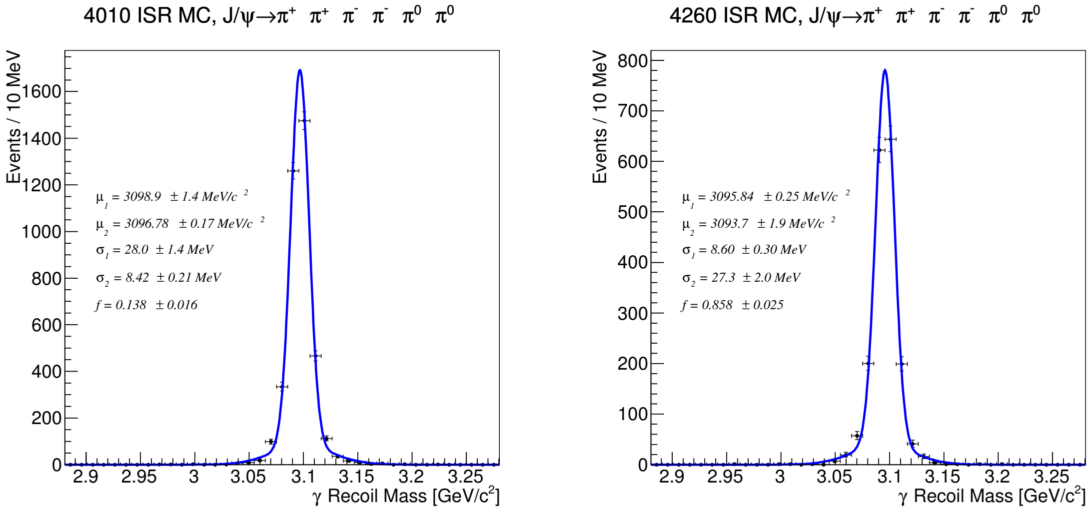

Figure 7.9: Fit to process, $J/\psi \to \pi^+\pi^+\pi^-\pi^-\pi^0\pi^0$, generated at center-of-mass energy 4.01 GeV (left) and 4.26 GeV (right).

7.4.2 Measurement of $\sigma(e^+e^-(\gamma_{isr}) \to J/\psi)$

The large number if ISR events in data due to the decay process $J/\psi \to X_i$ offers an interesting way to cross check our fitting procedure. We can compare experimental with theoretical calculations of $\sigma(e^+e^-(\gamma_{isr}) \to J/\psi)$ at each center-of-mass energy.

The theoretical cross section can be calculated from the formula below

$$\sigma(e^+e^-(\gamma_{isr}) \rightarrow J/\psi) = \int_0^1 W(s,x)\sigma_{J/\psi}(x)dx \tag{7.4}$$

where $\sqrt{s}$ is the center of mass energy, $x = 2E_\gamma/\sqrt{s}$, E_γ is the ISR photon energy, and $W(s,x)$ is the radiator function. The J/ψ cross section, $\sigma_{J/\psi}$, follows the Breit-Wigner formula given in Eqn 6.8, where we use the measurements given in Ref [16] for the $\Gamma_{ee}(J/\psi)$ and $\Gamma_{\text{tot}}(J/\psi)$ parameters.

The J/ψ ISR and $\eta_c(1S)$ experimental cross sections are extracted simultaneously. This fit is performed with the six final states with the strongest J/ψ signal, they are: $2(\pi^+\pi^-\pi^0), K^+K^-\pi^+\pi^-\pi^0, 3(\pi^+\pi^-), 2(\pi^+\pi^-), \pi^+\pi^-K^+K^-, 2(\pi^+\pi^+)K^+K^-$. In the fit a shared parameter representing the number of J/ψ is passed to the six chosen final states. The number of $e^+e^-(\gamma_{isr}) \rightarrow J/\psi$ is scaled in each final state by the J/ψ branching [56] and efficiency. The resulting experimental cross section is shown in Figure 7.10. It is great to see such good agreement between the experimental and theoretical measurements. This means our fitting procedure is correctly measuring the J/ψ process which lends credibility to our fitting procedure.

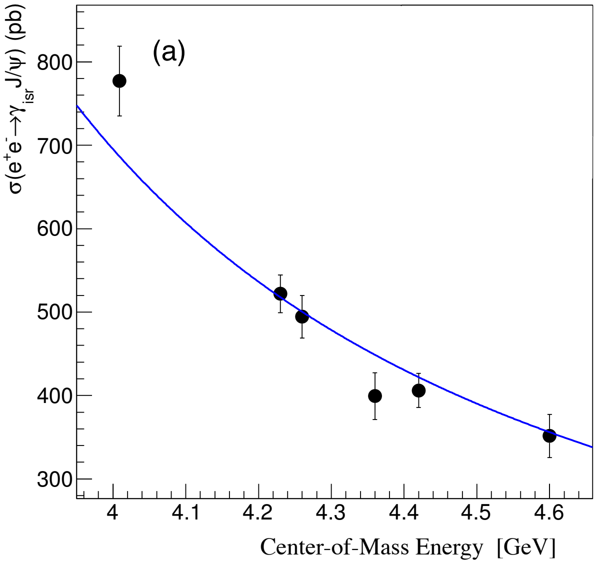

Figure 7.10: (Top) The $e^+e^-(\gamma_{\text{ISR}}) \rightarrow J/\psi$ Born cross section measurement (points) compared to the theoretical calculation (line) [37, 16].

7.4.3 $e^+e^-\gamma_{\text{isr}} \to J/\psi, J/\psi \to \gamma\eta_c(1S)$

The contribution from the peaking background $J/\psi \to \gamma\eta_c(1S)$ where the J/ψ is created through initial state radiation is investigated using KKMC. The reconstruction efficiency of the signal process $e^+e^- \to \gamma\eta_c(1S)$ is at least 1000 times greater than the background process $e^+e^- \to \gamma_{ISR}J/\psi, J/\psi \to \gamma\eta_c(1S)$, see Figure 7.11. This is reasonable considering most ISR photons will be lost down the beam pipe and the kinematic fit should do a good job of rejecting background processes where the total center of mass energy is 100 MeV off.

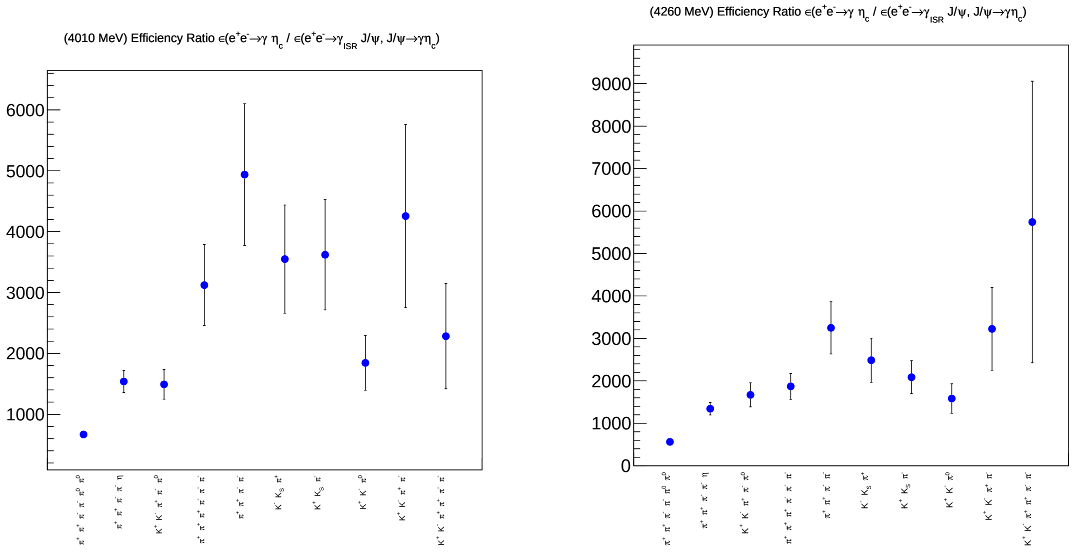

Figure 7.11: The reconstruction efficiency of the signal process $e^+e^- \to \gamma\eta_c(1S)$ divided by the background process $e^+e^- \to \gamma_{isr}J/\psi, J/\psi \to \gamma\eta_c(1S)$ at 4.01 GeV (left) and 4.26 GeV (right).

The expected number of peaking background is

$$\begin{aligned} N(e^+e^- \to \gamma_{isr} J/\psi, J/\psi \to \gamma\eta_c(1S), \eta_c(1S) \to X_i) &= \sigma(e^+e^- \to \gamma_{isr} J/\psi) \\ &\times \mathcal{B}(J/\psi \to \gamma\eta_c(1S))\mathcal{L}\mathcal{B}(\eta_c(1S) \to X_i) \\ &\times \epsilon(e^+e^- \to \gamma_{isr} J/\psi, J/\psi \to \gamma\eta_c(1S), \eta_c(1S) \to X_i) \end{aligned} \tag{7.5}$$

where X_i is a decay channel of $\eta_c(1S)$, $\mathcal{L}$ is the luminosity, $\mathcal{B}$ is the branching fraction, $\sigma(e^+e^- \to \gamma_{isr} J/\psi)$ is the theoretical Born cross section, and $\epsilon(e^+e^- \to \gamma_{isr} J/\psi, J/\psi \to \gamma\eta_c(1S), \eta_c(1S) \to X_i)$ is the reconstruction efficiency. The resulting recoil-mass distribution of the of the transition photon for each $\eta_c(1S)$ decay channel at center of mass energy 4.01 and 4.26 GeV are shown in Figure 7.12 and 7.13. The total contribution from all modes on the signal is less than one count which is considered negligible.

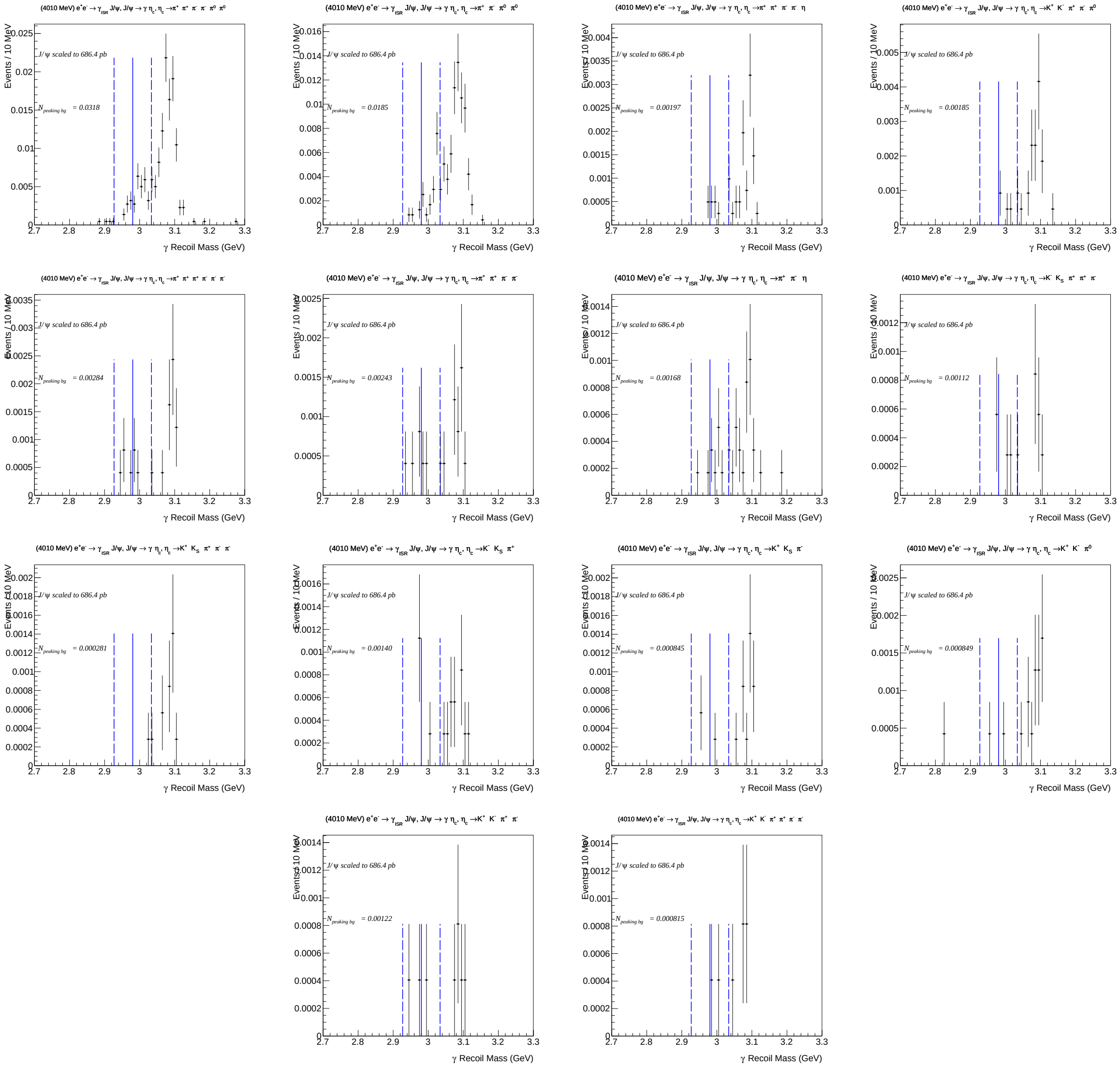

Figure 7.12: Study of peaking background $e^+e^- \to \gamma_{\rm ISR}J/\psi, J/\psi \to \gamma\eta_c(1S)$ for each $\eta_c(1S)$ decay at 4.01 GeV. The MC is scaled by the theoretical cross section $\sigma(e^+e^- \to \gamma_{\rm ISR}J/\psi)$.

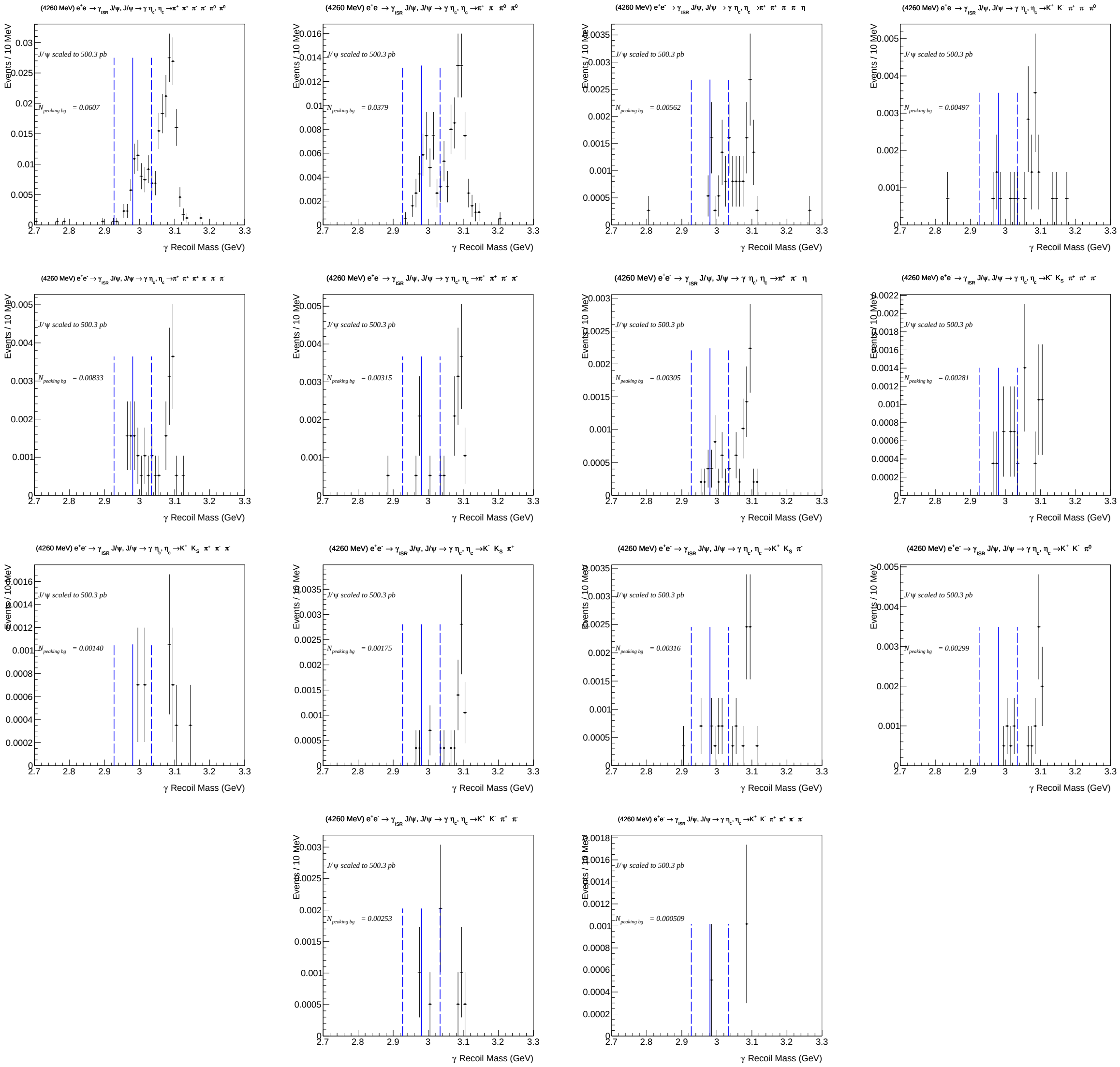

Figure 7.13: Study of peaking background $e^+e^- \rightarrow \gamma_{\mathrm{ISR}} J/\psi, J/\psi \rightarrow \gamma\eta_c(1S)$ for each $\eta_c(1S)$ decay at 4.26 GeV. The MC is scaled by the theoretical cross section $\sigma(e^+e^- \rightarrow \gamma_{\mathrm{ISR}} J/\psi)$.

Chapter 8

Results for $\mathbf{e^+e^- \to \gamma\eta_c(1S)}$

To determine the Born cross section, $\sigma_E(e^+e^- \to \gamma\eta_c(1S))$, we analyze the selected events using the selection criterium listed in Table 7.3 from each of the six center-of-mass energies E. The $\eta_c(1S)$ signal is described by a non-relativistic Breit-Wigner distribution convolved with the detector resolution and effects due to ISR. The mass and width of the $\eta_c(1S)$ are fixed to the average values from the PDG. The detector resolution and ISR effects are fixed using MC studies.

The major backgrounds in the recoil-mass distribution of the transition photon are from the continuum $q\bar{q}$ process and the J/ψ ISR process, $e^+e^-(\gamma_{\mathrm{ISR}}) \to J/\psi$, where the J/ψ decays to the same channels as the $\eta_c(1S)$. The potential background where the J/ψ decays to $\gamma\eta_c(1S)$ has been found to be negligible. The continuum is described independently in each decay channel using a second order polynomial. The J/ψ ISR background is parameterized by a double Gaussian function whose shape is fixed using MC studies. The size of the J/ψ ISR background can either be fit independently in each decay channel or can be simultaneously fit using information about the J/ψ branching fractions. In the baseline fit, this size is fit independently, but the difference between fit strategies is used as a systematic error.

The results of the Born cross section from simultaneously fitting the twelve distributions of the recoil-mass of the transition photon independently at each energy will be presented in section 8.1. In Section 8.2 we combine the six energies under four ISR assumptions: σ_{BELLE}, $\sigma_{Y(4260)}$, σ_{FLAT}, $\sigma_{Y(4360)}$. These assumptions allow us to both combine the data samples and search for $e^+e^- \to \gamma\eta_c(1S)$ using a larger sample of events. It also allows us to compare the $Y(4260)$ hypothesis to other hypotheses.

The energy-dependent cross section assumptions investigated in this analysis are explained below

1. σ_{FLAT}: the cross section is constant, consistent with the calculation in Ref. [61];
2. σ_{BELLE}: the cross section follows the Belle parameterization of $\sigma(e^+e^- \to \pi^+\pi^- J/\psi)$ found in Ref. [50], modeled with a Y(4008) in addition to the $Y(4260)$;
3. $\sigma_{\mathrm{Y(4260)}}$: the cross section follows a non-relativistic Breit-Wigner distribution for the $Y(4260)$ with its mass and width taken from the PDG;
4. $\sigma_{\mathrm{Y(4360)}}$: the cross section follows a non-relativistic Breit-Wigner distribution for the $Y(4360)$ with its mass and width taken from the PDG.

The systematic errors to the measurement are discussed in Chapter 9. Final closing remarks regarding the interpretations of these results are discussed in Chapter 10.

8.1 Single energy fits

At each energy, we use an unbinned maximum likelihood method to simultaneously fit the recoil-mass distribution of the transition photon associated with the twelve final states γX_i. The fit at 4.23 GeV is shown in Fig. 8.1. The total fit projections from each of the six energies are shown in Fig. 8.2(a-f). The fit range is centered at the $\eta_c(1S)$ mass and extends 450 MeV/c^2 on either side. The size of the $\eta_c(1S)$ signal, parameterized by $\sigma_E(e^+e^- \to \gamma\eta_c(1S))$, is a shared free parameter in the fit that accounts for the $\eta_c(1S)$ branching fractions, the reconstruction efficiencies, the corrections due to ISR effects, the vacuum polarization [15], and the integrated luminosity.

Our final measurements of $\sigma_E(e^+e^- \to \gamma\eta_c(1S))$ are listed in Table 8.1 and are shown as the points in Fig. 8.3(b). These use the $\sigma_{\Upsilon(4260)}$ assumption for the calculation of effects due to ISR. The other assumptions are also used and the differences range from 1% to 6%, which are included in the systematic errors. Significances are obtained by comparing the likelihoods of fits with and without the $\eta_c(1S)$ signal. The largest significance (3.0σ) is found at $E = 4.26$ GeV.

An upper limit of the measured Born cross section is calculated at each center-of-mass energy and shown in Table 8.1. The calculation follows Chapter 5.6, where we scan the likelihood by varying $\sigma(e^+e^- \to \gamma\eta_c(1S))$ and keeping all other parameters fixed to their nominal values in the fit. A systematic error is incorporated by convolving the likelihood profile with a normal distribution $\mathcal{N}(\mu, \sigma)$, where $\mu = 0$ and $\sigma = \sigma_{\text{syst.}}$ or the systematic error in picobarns.

The tabulated results of the cross section for all other assumptions on the energy-dependence of the cross section are shown in Appendix C. The fit projections to each final state for each energy is also shown in Appendix C.

Energy (GeV)	$\sigma_E(e^+e^- \to \gamma\eta_c(1S))$ (pb)	Significance (σ)	$UL_{\text{stat}} \oplus \mathcal{N}(0, \sigma_{\text{syst.}})$ (pb)
4.01	$0.44 \pm 1.02 \pm 0.32$	0.4	2.3
4.23	$1.34 \pm 0.59 \pm 0.21$	2.2	2.2
4.26	$2.17 \pm 0.70 \pm 0.35$	3.0	3.2
4.36	$2.03 \pm 0.77 \pm 0.37$	2.7	3.2
4.42	$0.71 \pm 0.48 \pm 0.33$	1.4	1.5
4.60	$0.23 \pm 0.53 \pm 0.34$	0.4	1.2

Table 8.1: The results for $\sigma_E(e^+e^- \to \gamma\eta_c(1S))$ at each center-of-mass energy. The first error is statistical and the second is systematic. Upper limits (at 90% confidence level) are calculated by scanning the likelihood function to account for statistical errors and then convolving it with the systematic error described by a Gaussian ($\mathcal{N}(\mu, \sigma)$) centered at 0 and a width of $\sigma_{\text{syst.}}$, where $\sigma_{\text{syst.}}$ is the total systematic error.

8.2 Combined energy fits

Because there is little evidence for the $e^+e^- \to \gamma\eta_c(1S)$ process at any individual energy, we combine all six energies under various assumptions for the energy-dependence of the cross section. In this case, we perform a simultaneous fit to 6×12 recoil-mass distribution of the transition photon. At each energy, the $\gamma\eta_c(1S)$ cross section is constrained to be the same, as before. But between energies, the cross section is now constrained to follow the σ_{FLAT}, σ_{BELLE}, $\sigma_{\mathrm{Y(4260)}}$, or $\sigma_{\mathrm{Y(4360)}}$ cross section assumptions. Table 8.2 lists the final peak cross sections using this method, where the peak is measured at 4.26 GeV for the $\sigma_{\mathrm{Y(4260)}}$ and σ_{BELLE} assumptions; and 4.36 GeV for the $\sigma_{\mathrm{Y(4360)}}$ assumption. Figure 8.2(g-h) shows no observable difference in the fit projections for the $\sigma_{\mathrm{Y(4260)}}$ and σ_{FLAT} assumptions; and the solid lines in Fig. 8.3 show the resulting cross sections as a function of energy. The statistical significance of the $\gamma\eta_c(1S)$ process is at least 3.6σ, regardless of our input cross section assumption.

While we find evidence for $e^+e^- \to \gamma\eta_c(1S)$ in our combined fits, we are unable to distinguish among the different assumptions for the energy dependence of the cross section. To test the significance of the $\sigma_{\mathrm{Y(4260)}}$ shape, we compare the likelihood of a fit assuming a combination of $\sigma_{\mathrm{Y(4260)}}$ and σ_{FLAT} (where the sizes of both components are free parameters in the fit) to the likelihood of the fit assuming σ_{FLAT}. In this test, we find the significance of the $\sigma_{\mathrm{Y(4260)}}$ component to be only 1.5σ.

Assumptions	$\sigma_{\text{peak}}(e^+e^- \to \gamma\eta_c(1S))$ (pb)	Significance (σ)	$UL_{\text{stat}} \oplus \mathcal{N}(0, \sigma_{\text{syst.}})$ (pb)
σ_{FLAT}	$1.16 \pm 0.27 \pm 0.18$	4.1	1.6
σ_{BELLE}	$2.27 \pm 0.49 \pm 0.35$	4.5	3.0
$\sigma_{\Upsilon(4260)}$	$2.11 \pm 0.49 \pm 0.33$	4.2	2.9
$\sigma_{\Upsilon(4360)}$	$2.72 \pm 0.71 \pm 0.42$	3.6	3.9

Table 8.2: The results for the combined-energy fits. The Born cross section is given at the peak center-of-mass energy under various assumptions for the energy dependence of the cross section. The first error is statistical and the second is systematic. Upper limits (at 90% confidence level) are calculated by scanning the likelihood function to account for statistical errors and then convolving it with the systematic error described by a Gaussian ($\mathcal{N}(\mu, \sigma)$) centered at 0 and a width of $\sigma_{\text{syst.}}$, where $\sigma_{\text{syst.}}$ is the total systematic error.

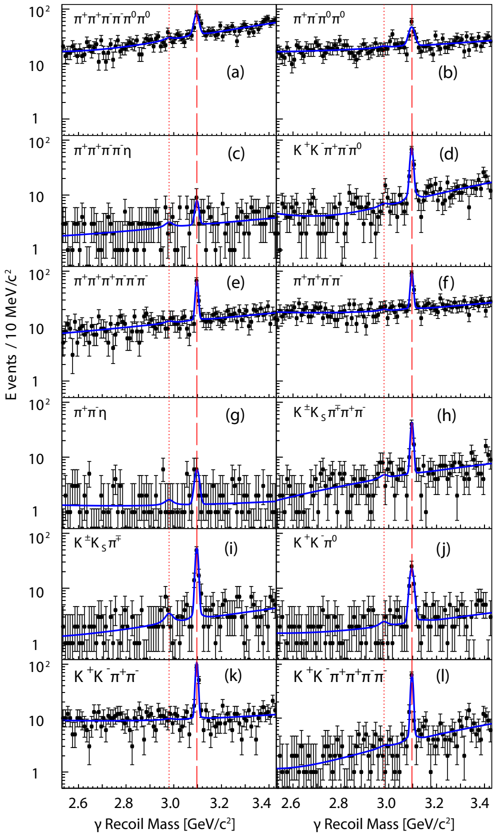

Figure 8.1: The recoil-mass distribution of the transition photon for each $\eta_c(1S)$ decay channel at center-of-mass energy 4.23 GeV. Projections from the simultaneous fit are overlaid. A dotted line indicates the $\eta_c(1S)$ mass; a dashed line indicates the J/ψ mass.

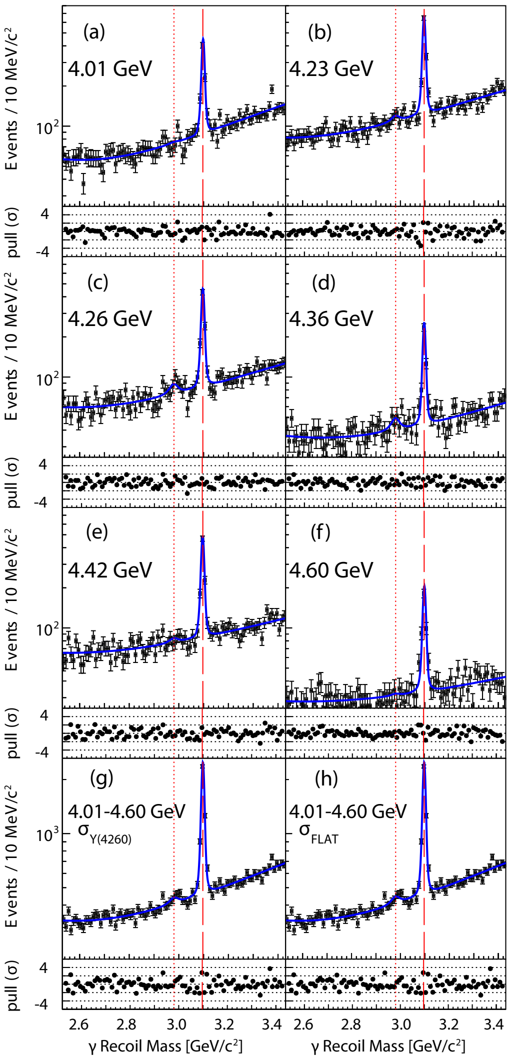

Figure 8.2: The transition photon recoil mass distributions summed over all $\eta_c(1S)$ decay channels. Results from the simultaneous fits are overlaid. In (a-f) the fits are performed separately at each energy; in (g) the data is combined using the $\sigma_{\Upsilon(4260)}$ assumption; in (h) the data is combined using σ_{FLAT}. Pull distributions, derived by comparing the fit projections and the data, are shown below each plot. A dotted line indicates the $\eta_c(1S)$ mass; a dashed line indicates the J/ψ mass.

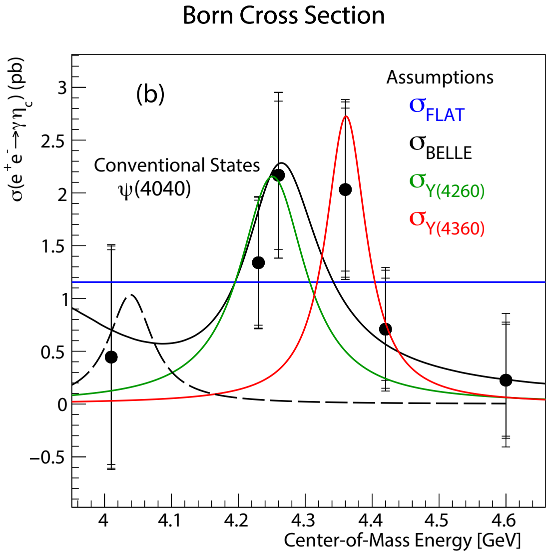

Figure 8.3: The $e^+e^- \to \gamma\eta_c(1S)$ Born cross section measured at each center-of-mass energy (points) and measured using the sum of all the data under various assumptions about the energy-dependence of the cross section (lines). The first tick marks are due to the statistical error, the intermediate tick marks sum in quadrature the statistical and the systematic errors correlated in energy (see, Table 9.12), and the outermost tick marks sum in quadrature both the statistical and total systematic errors. The predicted $e^+e^- \to \psi(4040) \to \gamma\eta_c(1S)$ cross section [27] is shown as the dashed line.

Chapter 9

Systematics

The $e^+e^- \to \gamma\eta_c(1S)$ Born cross section measured is the last chapter is susceptible to statistical fluctuations due to the limited number of $\eta_c(1S)$ we were able to reconstruct. In addition, there are systematic effects that can effect the measured Born cross section. In this analysis this includes measurements used to derive the cross section such as the uncertainty in the $\eta_c(1S)$ branching fractions (9.1) and the uncertainties in our reconstruction efficiencies due to producing limited MC statistics (9.2). In addition, the $\eta_c(1S)$ substructure is not modeled by our MC so this introduces a systematic error. This is discussed in section 9.3.

In the measurement of the beam energy there is an uncertainty of 1 MeV which causes a systematic error, see section 9.4. Other systematic uncertainties include the reconstruction algorithms ability to accurately track charged particles, measure photon energy, or reconstruct a K_S, see section 9.5. In section 9.6 we estimate the systematic error from the kinematic fit at each center-of-mass energy.

If we compare the detector resolutions between data and MC we find differences which will introduce a systematic error in our measurement, see section 9.7. We would also expect changes in the number of $\eta_c(1S)$ due to variations in the fit shape such as varying the $\eta_c(1S)$ mass and width parameters according to their error (9.8). In addition, section 9.9 describes the systematic error from describing the $\eta_c(1S)$ signal shape with a parameterization that account for distortions in $\eta_c(1S)$ lineshape due to the photon energy-dependence of electromagnetic transitions [55, 18]. Furthermore, the J/ψ ISR distribution can be fit in two ways that can effect this measurement, they are: a simultaneous fit of the J/ψ in final states with the most number of J/ψ ISR background or by fitting the J/ψ independently for each final state. The difference cause changes in our measured $e^+e^- \to \gamma\eta_c(1S)$ Born cross section. This systematic effect is further discussed in section 9.10. Lastly, changing the background shape that describes the continuum will introduce a systematic error that is discussed in section 9.11.

The section ends with a summary of the systematic uncertainties.

9.1 $\mathcal{B}(\eta_c(1S) \to X)$

One of the largest systematic errors comes from uncertainty in the branching fractions of the $\eta_c(1S)$ decays. We estimate this error by performing many trials of our simultaneous fitting procedure using different input $\eta_c(1S)$ branching fractions, which are randomly generated according to their errors. When available, we use the branching fractions measured by BESIII in Ref. [10]. Since those measurements were performed by taking the ratio of $\mathcal{B}(\psi(2S) \to \pi^0 h_c(1P)) \times \mathcal{B}(h_c(1P) \to \gamma\eta_c(1S)) \times \mathcal{B}(\eta_c(1S) \to X_i))$ with $\mathcal{B}(\psi' \to \pi^0 h_c(1P)) \times \mathcal{B}(h_c(1P) \to \gamma\eta_c(1S))$, we account for correlated errors by randomly varying the numerator and denominator separately according to their errors. The RMS of the resulting $e^+e^- \to \gamma\eta_c(1S)$ cross sections are taken as the systematic error. The minimum significance of measuring $\sigma_E(e^+e^- \to \gamma\eta_c(1S))$ after all these variations of the input branching fractions is given below in Table 9.1.

Energy	Avg N$_{signal}$	Rms N$_{signal}$	Minimum significance	Rms significance	Systematic
4010 MeV	143	59	-0.154	0.313	41 %
4230 MeV	1020	92	1.74	0.126	10 %
4260 MeV	1278	152	2.26	0.221	12 %
4360 MeV	806	92	1.98	0.189	12 %
4420 MeV	570	101	0.714	0.225	18 %
4600 MeV	89	34	-0.0587	0.155	39 %
Combined Energies	2.03 pb	0.146 pb	3.75	0.175	8 %

Table 9.1: Study of the systematic error due to the uncertainty in the measured $\eta_c(1S) \to X_i$ branching fraction. The average and root-mean square cross section of the trials is reported. In addition, the minimum significance of $\sigma_E(e^+e^- \to \gamma\eta_c(1S))$, the root-mean square of the significance, and the systematic error are also reported.

9.2 $\epsilon(\eta_c(1S) \to X_i)$

A small systematic error (from 1% to 3%) is introduced by the statistical uncertainty of the reconstruction efficiency due to generating a limited number of MC statistics.

We estimate the error using the same procedure introduced in Chapter 9.1. That is, we perform many trials of the fits while randomly varying the efficiencies according to their errors. The RMS of the resulting $e^+e^- \to \gamma\eta_c(1S)$ cross sections are taken as the systematic error.

Energy	Avg N_{signal}	Rms N_{signal}	Minimum significance	Rms significance	Systematic
4010 MeV	156	3	0.365	0.00628	2 %
4230 MeV	1071	6	2.18	0.00747	1 %
4260 MeV	1344	6	3.02	0.00937	1 %
4360 MeV	850	4	2.63	0.00887	1 %
4420 MeV	591	5	1.40	0.0125	1 %
4600 MeV	94	2	0.372	0.00866	3 %
Combined Energies	2.11 pb	0.00693 pb	4.28	0.00898	1 %

Table 9.2: Study of the systematic error due to the uncertainty in the $\eta_c(1S) \to X_i$ reconstruction efficiency. The average and root-mean square cross section of the trials is reported. In addition, the minimum significance, the root-mean square of the significance, and the systematic error are also reported.

9.3 $\eta_c(1S)$ substructure

In our modeling of the $\eta_c(1S)$ decays we did not account for substructure. We could compare MC with and without substructure and take the difference in efficiency to estimate a systematic error as was done in the BESIII measurements of the $\eta_c(1S)$ branching fraction from $\psi(2S) \to \pi^0 h_c, h_c \to \gamma\eta_c(1S)$ [10]. Instead, since the final state channels in this analysis only differ from those in Ref [10] by a π^0, the $\eta_c(1S)$ substructures is the same. This means that the systematic error we measure in section 9.1 includes the systematic error due to modeling the $\eta_c(1S)$ decays without substructure.

9.4 e^+e^- beam energy

The 1 MeV beam energy uncertainty causes a 2 MeV shift in the center of mass. The systematic is estimated by varying the $\eta_c(1S)$ mass by ± 2 MeV.

Energy (MeV)	Minimum Significance (σ)	Systematic (%)
4010	0.32	18
4230	2.13	2
4260	3.04	2
4360	2.61	5
4420	1.42	2
4600	0.37	6
Combined Energies	5.00	1

Table 9.3: Study of the systematic error due to the uncertainty in the e^+e^- beam energy. The minimum significance and largest systematic error are shown for each center-of-mass energy.

9.5 Uncertainty in track, photon, and luminosity measurements

We assign an error of 1% per charged pion and kaon to account for uncertainty in the track reconstruction efficiency (including particle ID) [8, 9]. The error due to uncertainty in photon reconstruction efficiencies is taken as 1% per photon (including photons from π^0 and η) [13]. The total error attributed to the K_S reconstruction efficiency (arising from a combination of geometric acceptance, tracking efficiency, and selection efficiency) is 4% per K_S [11]. To account for correlations in reconstruction of the twelve X_i modes the efficiency is varied and refit. The largest difference with respect to the nominal measurement is taken as a system error.

To estimate the systematic error due to tracking, K_S, or photon we vary scale the efficiency in each final state by either $(1+\delta_{i,j})$ or $(1-\delta_{i,j})$, where δ is the systematic error for final state i and j is the systematic error under investigation. The data is refit to derive two new cross section: σ_j^+ and σ_j^-; and the largest difference with the nominal cross section is taken as a systematic error, see Table 9.4.

energy	Tracking	Photon	K_s	Luminosity
4010	8%	2%	2%	1%
4230	3%	3%	1%	1%
4260	5%	4%	2%	1%
4360	4%	3%	1%	1%
4420	4%	4%	1%	1%
4600	6%	4%	3%	1%
Combined Energies	4%	3%	4%	1%

Table 9.4: Study of the systematic error due uncertainties in tracking, photon energy, and luminosity

9.6 Kinematic fit

Uncertainties in the kinematic fitting efficiencies are evaluated by comparing the cross sections extracted with and without tracking corrections [4]. The correction factors are determined from the control sample $J/\psi \to \phi f_0(980)$.

Energy (MeV)	Systematic
4010	5 %
4230	1 %
4260	1 %
4360	3 %
4420	2 %
4600	2 %
Combined Energies	2 %

Table 9.5: Study of the systematic error due uncertainties in the kinematic fitting efficiencies.

9.7 Mass resolution

In our baseline fits to the $\eta_c(1S)$ mass spectrum, we use a resolution derived from MC for both the $\eta_c(1S)$ signal and for the ISR J/ψ peaks. Recall that for the $\eta_c(1S)$ peak, a histogram is used to parametrize the resolution, while for the ISR J/ψ peak a double Gaussian is used. Since the resolution in the data has been shown to be wider than that in the MC, this introduces a systematic error. To estimate this systematic error, we first use the J/ψ ISR peak in several channels to determine the ratio of resolutions between data and MC. We then smear the resolution of both the $\eta_c(1S)$ and J/ψ by this ratio and redo the fits. We take the largest differences as the systematic errors.

In order to determine the difference in resolution between data and MC, we fit the six largest ISR J/ψ peaks in data and MC with a Gaussian. The ratios of the J/ψ widths in data to the J/ψ widths in MC are shown in Table 9.6. The error weighted mean of this ratio is approximately 1.2. This ratio determines how much the MC resolution must increase to match data.

To increase the $\eta_c(1S)$ MC resolution, the $\eta_c(1S)$ resolution histogram is convolved with a Gaussian with a width that increases the MC width by a factor of 1.2. For the J/ψ, the width of each of the Gaussians in the baseline fit is increased by a factor of 1.2. After this smearing, the fits are redone and the resulting systematic uncertainties are shown in Table 9.7.

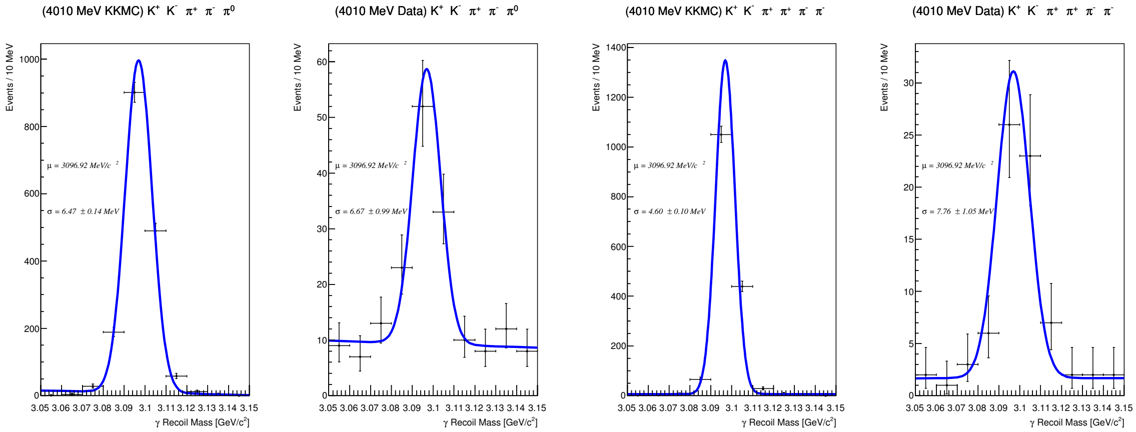

Figure 9.1: Comparison of the J/ψ resolution in data and MC for $J/\psi \to K^+K^-\pi^+\pi^-\pi^0$ and $K^+K^-\pi^+\pi^+\pi^-\pi^-$ at 4.01 GeV. The mass of the J/ψ is allowed to float in these fits.

$\eta_c(1S)$ Mode	MC Resolution (MeV)	Data Resolution (MeV)	Data/MC Resolution
$\pi^+\pi^+\pi^-\pi^-\pi^0\pi^0$	9.22 ± 0.17	9.46 ± 2.04	1.03 ± 0.22
$K^+K^-\pi^+\pi^-\pi^0$	6.47 ± 0.14	6.67 ± 0.99	1.03 ± 0.16
$\pi^+\pi^+\pi^+\pi^-\pi^-\pi^-$	5.32 ± 0.09	5.53 ± 1.30	1.04 ± 0.24
$\pi^+\pi^+\pi^-\pi^-$	5.35 ± 0.07	5.03 ± 1.88	0.94 ± 0.35
$K^+K^-\pi^+\pi^-$	4.75 ± 0.05	4.56 ± 0.62	0.96 ± 0.13
$K^+K^-\pi^+\pi^+\pi^-\pi^-$	4.60 ± 0.10	7.76 ± 1.05	1.69 ± 0.23

Table 9.6: Comparison of the J/ψ resolution in data and MC for the six final state channels with a large J/ψ signal at 4.01 GeV.

Energy (MeV)	Cross section	Significance	Systematic
4010	0.462 ± 0.861 pb	0.55 σ	44 %
4230	1.042 ± 0.473 pb	2.35 σ	7 %
4260	1.757 ± 0.552 pb	3.28 σ	8 %
4360	1.668 ± 0.633 pb	2.81 σ	6 %
4420	0.643 ± 0.401 pb	1.69 σ	18 %
4600	0.238 ± 0.433 pb	0.57 σ	42 %
Combined Energies	2.352 ± 0.516 pb	5.45 σ	8 %

Table 9.7: Study of the systematic error due to the uncertainty in the data and MC resolution differences. The $\eta_c(1S)$ and J/ψ components of the fit are independently smeared by a factor of 1.2. The largest difference in the cross section from the nominal fit at each center-of-mass energy is used to estimate the systematic error.

9.8 $\eta_c(1S)$ mass and width

The uncertainty due to the mass and width of the $\eta_c(1S)$ is estimated by varying the PDG mass and width by 1 σ.

Energy (MeV)	Minimum Significance (σ)	Systematic (%)
4010	0.35	10
4230	2.17	1
4260	3.04	2
4360	2.62	3
4420	1.43	3
4600	0.38	3
Combined Energies	5.00	1

Table 9.8: Study of the systematic error due to the uncertainty in the $\eta_c(1S)$ mass and width measurements. The minimum significance and largest systematic error are shown for each center-of-mass energy.

9.9 $\eta_c(1S)$ lineshape

The nominal $\eta_c(1S)$ signal shape in this analysis uses a non-relativistic Breit-Wigner, which ignore distortions in the lineshape due to the effect of phase space. In allowed E1/M1 transitions a cubic photon energy term is introduced to the signal shape, which accounts for the transition matrix element and phase space factor but requires a damping term at higher energies [55, 18]. The difference between fitting with a nominal signal shape and that used by the KEDR collaboration is taken as a systematic, see the equation below.

$$(E_\gamma^3 \times BW(m) \times f_d(E_\gamma) \bigotimes R_{i,j}(m)) \tag{9.1}$$

where $BW(m)$ is the Breit-Wigner function for $\eta_c(1S)$, $E_\gamma(m) = \frac{s-m^2}{2\sqrt{(s)}}$ is the energy of the transition photon (s is the center of mass energy squared), $R_{i,j}(m)$ is the resolution for mode i at energy j, and $f_d(E_\gamma)$ is the damping factor used by the KEDR collaboration.

$$f_d(E_\gamma) = \frac{E_0^2}{E_\gamma E_0 + (E_\gamma - E_0)^2} \tag{9.2}$$

where $E_0 = E_\gamma(m_{\eta_c(1S)})$ is the transition-photon energy peak.

Energy (MeV)	KEDR cross section	Significance	Systematic
4010	0.308 ± 0.849 pb	0.37 σ	5 %
4230	0.911 ± 0.464 pb	2.06 σ	8 %
4260	1.614 ± 0.546 pb	3.05 σ	1 %
4360	1.493 ± 0.624 pb	2.53 σ	6 %
4420	0.716 ± 0.401 pb	2.16 σ	31 %
4600	0.116 ± 0.427 pb	0.27 σ	31 %
Combined Energies	2.172 ± 0.511 pb	4.38 σ	1 %

Table 9.9: Study of the systematic error due to distortions in the $\eta_c(1S)$ lineshape. The $\eta_c(1S)$ component of the fit is altered by introducing a cubic transition photon energy term and an associated damping factor. The resulting cross section, significance, and systematic error are shown at each center-of-mass energy.

9.10 Uncertainty in fitting the J/ψ peak

There is an uncertainty when measuring the $\gamma\eta_c(1S)$ production cross section due to different ways of fitting the prominent J/ψ peak in the photon recoil distribution. The nominal fit in this analysis independently floats the number of J/ψ in each channel. Another method is to constrain the number of J/ψ by the branching fraction and efficiency using KKMC where $e^+e^- \to \gamma_{ISR}J/\psi, J/\psi \to X$, where X are the $\eta_c(1S)$ decay modes studied in this analysis.

Since only 8 of the 12 $\eta_c(1S)$ decay modes also decay from J/ψ these are the only modes constrained in the fit and the other modes are allowed to float. The J/ψ ISR production cross section in data is measured mode-by-mode and shown in Figure 9.2. The dashed green line in Figure 9.2 represents the J/ψ cross section when simultaneously fitting the J/ψ peak in data with a single parameter that is scaled by each modes branching fraction to J/ψ and efficiency, calculated with KKMC where $e^+e^- \to \gamma_{ISR}J/\psi, J/\psi \to X$. As Figure 9.2 shows there is good agreement between each mode, the constrained fit, and the theoretical calculation, see Appendix E for more on the measurement of the J/ψ production cross section.

The systematic due to constraining the J/ψ ISR is shown in Table 9.10.

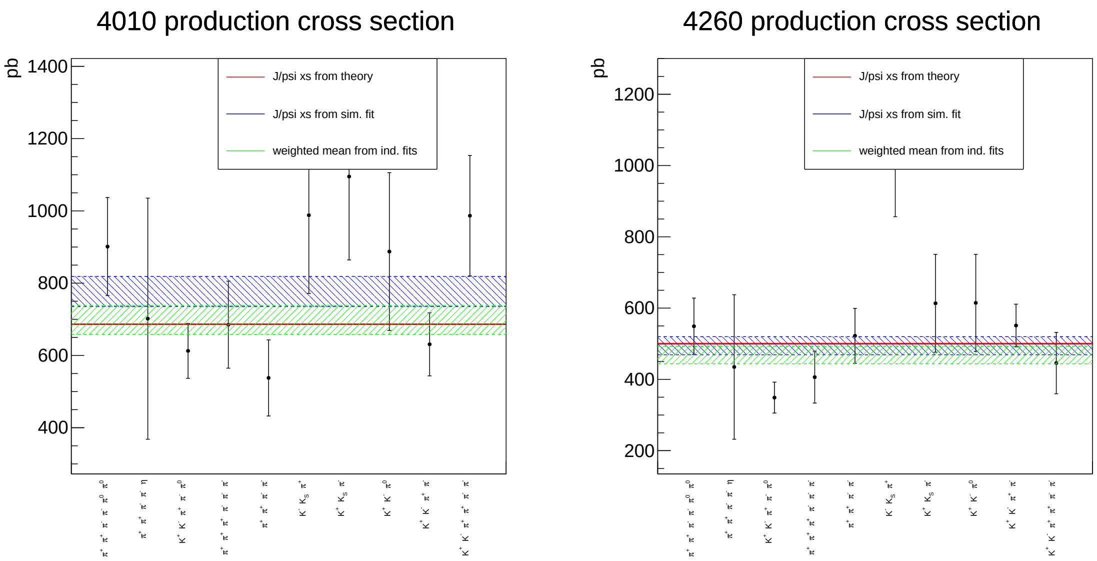

Figure 9.2: The J/ψ cross section at center-of-mass energy 4.01 and 4.26 GeV as a function of decay channel. The weighted mean of the individual measurements of the cross section is shown shaded in green. The cross section and its error extracted from the simultaneous fit is shown in blue. These measurements are consistent with the theoretical cross section (red) calculated by integrating the radiator function (W) with the J/ψ cross section, Eqn 7.4.

Energy (MeV)	Nominal (float ISR)	Constrain ISR	Systematic
4010	0.322 pb	0.257 pb	21 %
4230	0.980 pb	0.944 pb	4 %
4260	1.627 pb	1.604 pb	2 %
4360	1.574 pb	1.556 pb	2 %
4420	0.549 pb	0.512 pb	7 %
4600	0.168 pb	0.063 pb	63 %
Combined Energies	2.180 pb	2.060 pb	6 %

Table 9.10: Study of the systematic error due to fitting the different ways to fit the J/ψ peak. The difference in the $\eta_c(1S)$ cross section for the different ways of fitting the J/ψ are taken as a systematic error and shown for each energy.

9.11 Background shape

The nominal fit in this analysis uses a 2nd order Chebyshev polynomial to fit the continuum background. The systematic uncertainty due to the background shape is investigated by fitting the background with a 3rd order Chebyshev polynomial and taking the difference with the nominal fit. The resulting systematic is shown in Table 9.11.

9.12 Total

The total systematic error is obtained by adding the individual systematic errors in quadrature.

Energy (MeV)	Cross section	Significance	Systematic
4010 MeV	0.228 ± 0.850 pb	0.27 σ	30 %
4230 MeV	1.024 ± 0.469 pb	2.16 σ	5 %
4260 MeV	1.597 ± 0.546 pb	2.90 σ	2 %
4360 MeV	1.462 ± 0.626 pb	2.36 σ	8 %
4420 MeV	0.674 ± 0.399 pb	1.63 σ	23 %
4600 MeV	-0.038 ± 0.422 pb	0.00 σ	117 events
Combined Energies	2.209 ± 0.510 pb	4.36 σ	2 %

Table 9.11: Study of the systematic error due to uncertainties in the parameterization of background shape. The resulting $\eta_c(1S)$ cross section, significance, and systematic error when replacing the 2nd order Chebyshev polynomial with a 3rd order one are shown.

	4010 MeV	4230 MeV	4260 MeV	4360 MeV	4420 MeV	4600 MeV	Combined Energies
* $\mathcal{B}(\eta_c(1S) \to X_i)$ branching fraction	41 %	9 %	12 %	11 %	18 %	38 %	7 %
MC statistics	2 %	1 %	1 %	1 %	1 %	2 %	1 %
* Mass resolution	43 %	6 %	8 %	6 %	17 %	42 %	10 %
* $\eta_c(1S)$ mass and width	10 %	1 %	2 %	3 %	3 %	3 %	1 %
e^+e^- beam energy	7 %	1 %	1 %	2 %	1 %	3 %	1 %
* $\eta_c(1S)$ lineshape	4 %	7 %	1 %	5 %	30 %	31 %	3 %
* Tracking efficiency	8 %	3 %	5 %	4 %	4 %	6 %	4 %
* Photon efficiency	2 %	3 %	4 %	3 %	4 %	4 %	3 %
* K_S efficiency	2 %	1 %	2 %	1 %	1 %	3 %	4 %
* Kinematic fitting	5 %	1 %	1 %	3 %	2 %	2 %	2 %
Background Shape	29 %	4 %	2 %	7 %	23 %	123 %	5 %
Luminosity	1 %	1 %	1 %	1 %	1 %	1 %	1 %
J/ψ peak	20 %	4 %	1 %	1 %	7 %	62 %	2 %
Total	73 %	16 %	16 %	18 %	46 %	153 %	15 %

Table 9.12: Summary of systematic errors at $\sqrt{s} = 4.01$, 4.23, 4.26, 4.36, 4.42, 4.60 GeV and at all energies combined. Errors with an asterisks (*) are correlated in energy.

Chapter 10

Conclusion

In summary, we search for the process $e^+e^- \to \gamma\eta_c(1S)$ at six center-of-mass energies between 4.01 and 4.60 GeV. While we do not find evidence for this process at any individual energy, the significance is consistently above 3σ when we combine all of our datasets according to the four assumptions listed above. With our current statistics, we cannot make firm conclusions about the energy-dependence of the cross section. However, we note that the cross section is better explained by $\sigma_{\mathrm{Y}(4260)}$ than by conventional charmonium states: $\psi(4040)$, $\psi(4160)$, and $\psi(4415)$, where the states are described by a Breit-Wigner with a mass and width fixed to the world average values given in the PDG [56]. The expected rate of $e^+e^- \to \psi(4040) \to \gamma\eta_c(1S)$, shown as the dashed line in Fig. 8.3(b), is estimated using the calculated partial width $\Gamma(\psi(4040) \to \gamma\eta_c(1S))$ [27]. If we assume the energy-dependence on the cross section follows the $\psi(4040)$ and fit our combined datasets, then the significance of $e^+e^- \to \gamma\eta_c(1S)$ is 1.9σ. Calculations are lacking of $\psi(4160)$ or $\psi(4415)$ to $\gamma\eta_c(1S)$, so their rate is allowed to float in fits to our combined datasets. The significance of $e^+e^- \to \gamma\eta_c(1S)$ assuming the $\psi(4415)$ is 1.9σ. In the case of the $\psi(4160)$ we are missing crucial data at energies near 4.16 GeV to constrain this assumption. Nevertheless, we measure the significance of $e^+e^- \to \gamma\eta_c(1S)$ assuming $\psi(4160)$ production to be 3.5σ, which is still less significant than our weakest nonconventional assumption of the $\gamma\eta_c(1S)$ production mechanism, namely: $\sigma_{\mathrm{Y(4360)}}$. Although we are unable to unambiguously determine the production mechanism of $\gamma\eta_c(1S)$, the enhancement in $e^+e^- \to \gamma\eta_c(1S)$ between 4.23-4.36 GeV may suggest production via a hybrid charmonium state.

If we assume the process $e^+e^- \to \gamma\eta_c(1S)$ proceeds through a $Y(4260)$, we measure $\sigma_{4.26}(e^+e^- \to \gamma\eta_c(1S)) = 2.11 \pm 0.49(\mathrm{stat.}) \pm 0.32(\mathrm{syst.})$ pb. Combining this with a previous BESIII measurement of $\sigma_{4.26}(e^+e^- \to \pi^+\pi^- J/\psi)$ [12], we estimate the ratio $\mathcal{B}(Y(4260) \to \gamma\eta_c(1S))/\mathcal{B}(Y(4260) \to \pi^+\pi^- J/\psi) = 0.034 \pm 0.005$, where the statistical and systematic errors have been combined.

To test the significance of the $\sigma_{\mathrm{Y(4260)}}$ shape, we compare the likelihood of a fit assuming a combination of $\sigma_{\mathrm{Y(4260)}}$ and σ_{FLAT} (where the sizes of both components are free parameters in the fit) to the likelihood of the fit assuming σ_{FLAT}. In this test, we find the significance of the $\sigma_{\mathrm{Y(4260)}}$ component to be only 1.5σ.

Chapter A

Input-Output Study

A study was performed to test the correctness of the simultaneous fitting procedure. This was done by generating toy MC distributions that closely resemble the backgrounds in data with a 10 pb input Born cross section. The Born cross section is extracted from each simultaneous fit with a variable number of $\eta_c(1S)$ decay channels included. The modes used in each fit are randomized and range from 1 to 14. The fit for a given number of included $\eta_c(1S)$ decay channels is repeated 100 times. The mean and root-mean error are shown in Figure A.1.

The toy MC was generated by uniformly sampling from the probability density function of the signal and background. This type of MC is known as the acceptance-rejection method. One drawback of the acceptance-rejection method is that the method tends to favor concentrated areas that spike in certain regions of the pdf. This is avoided by generating the continuum, J/ψ ISR and $\eta_c(1S)$ distributions separately. The shape of the continuum background is determined by fitting the distribution in data and extracting the 2nd order Chebychev piece from the fit. This component of the background is generated by uniformly sampling from the probability density function of the continuum background. The size of the background in MC is equal to the size in data. To investigate the $\eta_c(1S) \to X_i$ and $J/\psi \to X_i$ efficiencies we generated large sets of data with KKMC for each final state channel, see Chapter 7.1. By sampling uniformly for these distributions we generate the respective toy MC. Each toy MC distribution is equivalent to 500 pb^{-1} of data at 4.01 GeV.

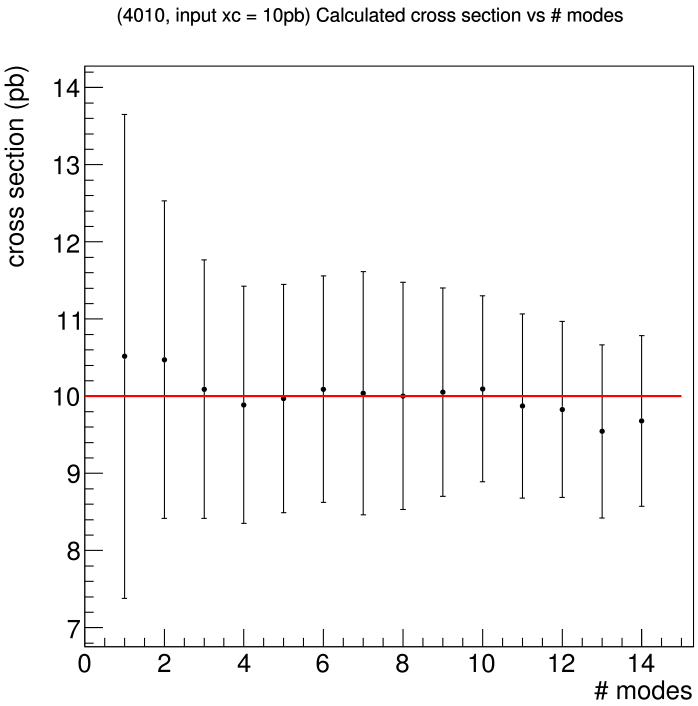

Figure A.1: Validation of fit procedure using data driven MC where the number of $\eta_c(1S)$ decay modes are varied and randomized. Each point represents the average and root mean square of 100 fits. The input $\eta_c(1S)$ production cross section is 10 pb and the input luminosity is 500 pb^{-1}.

Chapter B

Summary of event selection optimizations

In this analysis we rely on a figure of merit to characterize the significance of an event selection. The selection criteria's investigated included the kinematic χ^2/dof, the angle between the transition photon and a charged track (ShDang), the pull of the transition photon forming a π^0 with any other shower in the event (ShPi0Pull), and the decay length of a K_S divided by its error. Two type of background and signal yields were used to construct the figure of merit yielding a total of four combinations. The maximum figure of merit averaged between the four combinations of the figure of merit are shown as an arrow in the plots below. If a plot does not contain an arrow then this event selection was not used in the final event selection. In blue is the corresponding detector efficiency. The plots are meant to be read from left to right, where each subsequent event selection includes the best figure of merit from the event selection that precedes it.

B.1 $\eta_c(1S) \rightarrow \pi^+\pi^+\pi^-\pi^-\pi^0\pi^0$

Final Event Selection: $\chi^2/d.o.f$ <4.7 and π^0 Pull of monoenergetic photon>2.25σ

branching fraction = 17.2%

Energy (MeV)	eff	eff*(1+δ)	eff*(1+δ)	eff*(1+δ)	eff*(1+δ)
	No ISR	Flat	Belle Y(4260)	Breit-Wignet Y(4260)	Y(4360) ISR
4010	9.478±0.058%	7.199±0.050%	6.190±0.045%	7.030±0.045%	6.988±0.045%
4230	9.558±0.059%	7.315±0.051%	6.984±0.041%	7.056±0.044%	6.903±0.044%
4260	9.607±0.059%	7.335±0.050%	7.315±0.043%	7.329±0.046%	6.961±0.044%
4360	9.672±0.059%	7.389±0.051%	7.705±0.049%	7.760±0.057%	7.136±0.045%
4420	9.651±0.059%	7.259±0.050%	7.606±0.051%	7.657±0.062%	8.068±0.056%
4600	9.811±0.059%	7.457±0.052%	6.303±0.056%	7.618±0.073%	6.751±0.068%

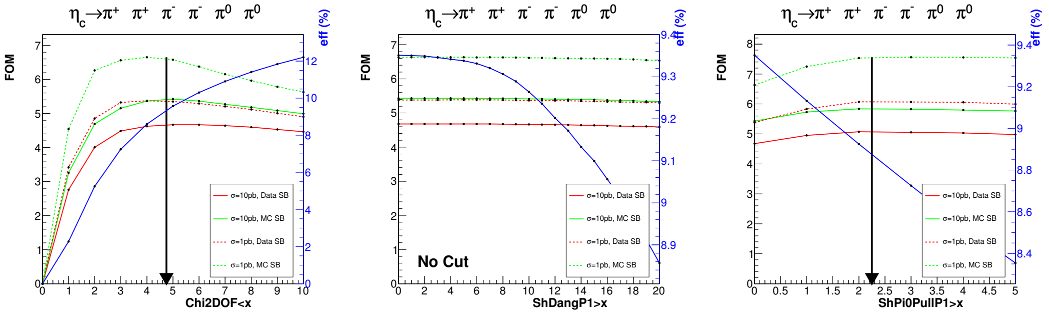

Figure B.1: (a) Optimization of $\chi^2/d.o.f$, (b) Optimization of angle between shower and closest charged track, (c) Optimization of rejecting the monoenergetic shower's π^0 pull

B.2 $\eta_c(1S) \to \pi^+\pi^-\pi^0\pi^0$

Final Event Selection: $\chi^2/d.o.f$ <4.0 and π^0 Pull of monoenergetic photon>3.25σ

branching fraction = 4.66%

Energy (MeV)	eff	eff*(1+δ)	eff*(1+δ)	eff*(1+δ)	eff*(1+δ)
	No ISR	Flat	Belle Y(4260)	Breit-Wignet Y(4260)	Y(4360) ISR
4010	17.860±0.155%	13.772±0.134%	11.584±0.122%	13.612±0.123%	13.391±0.122%
4230	18.156±0.157%	13.988±0.137%	12.224±0.112%	13.651±0.120%	13.095±0.119%
4260	18.273±0.157%	13.688±0.135%	12.820±0.113%	13.768±0.125%	13.174±0.117%
4360	18.146±0.156%	13.913±0.137%	13.390±0.133%	14.983±0.154%	13.535±0.120%
4420	18.103±0.157%	13.897±0.137%	13.340±0.142%	14.340±0.165%	15.758±0.153%
4600	18.324±0.157%	14.107±0.137%	12.026±0.151%	14.432±0.196%	12.900±0.184%

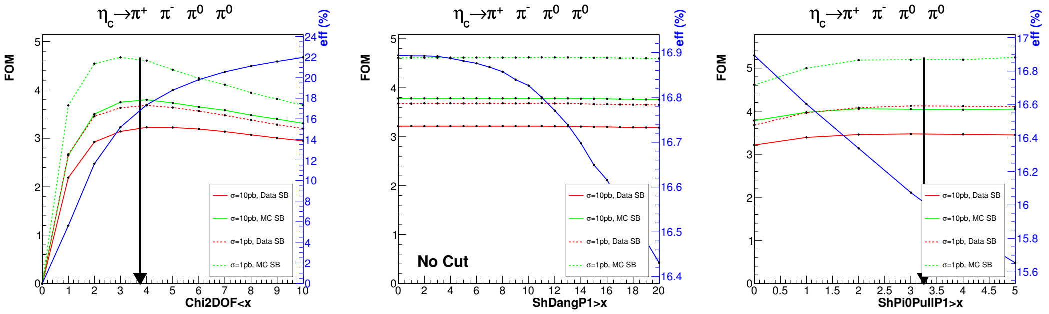

Figure B.2: (a) Optimization of χ^2/d.o.f, (b) Optimization of angle between shower and closest charged track, (c) Optimization of rejecting the monoenergetic shower's π^0 pull

B.3 $\eta_c(1S) \to \pi^+\pi^+\pi^-\pi^-\eta$

Final Event Selection: $\chi^2/d.o.f$ <3.5 and π^0 Pull of monoenergetic photon>3.50σ

branching fraction = 4.40%

Energy (MeV)	eff	eff*(1+δ)	eff*(1+δ)	eff*(1+δ)	eff*(1+δ)
	No ISR	Flat	Belle Y(4260)	Breit-Wignet Y(4260)	Y(4360) ISR
4010	17.976±0.157%	13.638±0.133%	12.594±0.125%	13.189±0.122%	12.832±0.120%
4230	18.184±0.158%	13.870±0.135%	13.429±0.115%	13.341±0.118%	13.241±0.118%
4260	18.204±0.158%	13.524±0.133%	13.618±0.118%	13.651±0.124%	13.107±0.117%
4360	18.492±0.157%	13.687±0.136%	14.315±0.136%	14.445±0.150%	13.576±0.121%
4420	18.586±0.159%	13.613±0.134%	14.105±0.143%	14.043±0.161%	15.131±0.148%
4600	18.924±0.161%	14.038±0.137%	12.897±0.155%	14.338±0.194%	12.786±0.180%

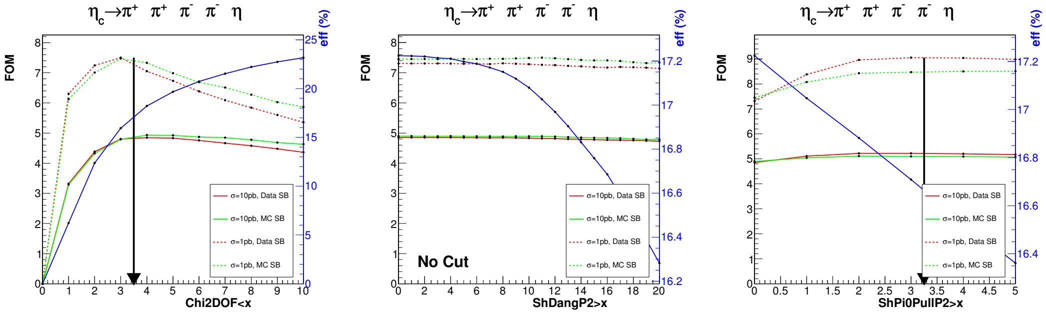

Figure B.3: (a) Optimization of $\chi^2/d.o.f$, (b) Optimization of angle between shower and closest charged track, (c) Optimization of rejecting the monoenergetic shower's π^0 pull

B.4 $\eta_c(1S) \to K^+K^-\pi^+\pi^-\pi^0$

Final Event Selection: $\chi^2/d.o.f$ <3.2 and π^0 Pull of monoenergetic photon>2.50σ and Prob(K$^+$)>Prob(π^+) and Prob(K$^-$)>Prob(π^-)

branching fraction = 3.50%

Energy (MeV)	eff	eff*(1+δ)	eff*(1+δ)	eff*(1+δ)	eff*(1+δ)
	No ISR	Flat	Belle Y(4260)	Breit-Wignet Y(4260)	Y(4360) ISR
4010	11.688±0.140%	8.754±0.120%	7.958±0.110%	8.740±0.109%	8.344±0.108%
4230	12.135±0.143%	9.074±0.121%	8.943±0.103%	8.881±0.108%	8.523±0.106%
4260	11.985±0.142%	8.982±0.122%	9.321±0.106%	9.083±0.112%	8.475±0.106%
4360	12.239±0.143%	9.224±0.122%	9.668±0.123%	9.533±0.136%	8.965±0.108%
4420	12.122±0.144%	9.208±0.123%	9.347±0.126%	9.211±0.147%	9.865±0.132%
4600	12.337±0.145%	9.272±0.123%	8.361±0.139%	9.286±0.175%	8.542±0.164%

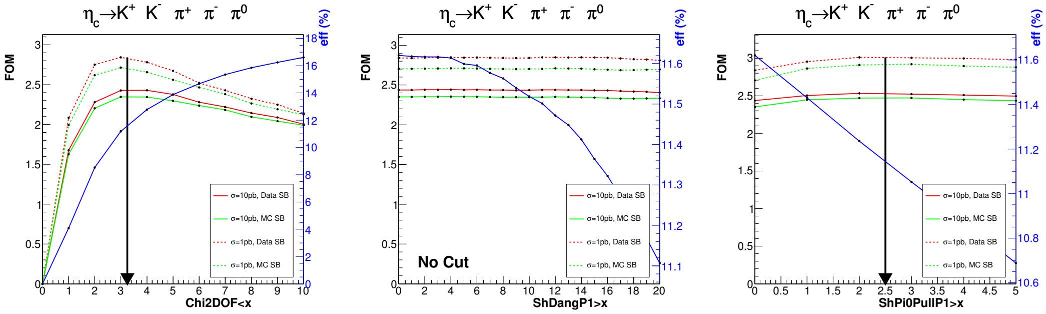

Figure B.4: (a) Optimization of $\chi^2/d.o.f$, (b) Optimization of angle between shower and closest charged track , (c) Optimization of rejecting the monoenergetic shower's π^0 pull

B.5 $\eta_c(1S) \to \pi^+\pi^+\pi^+\pi^-\pi^-\pi^-$

Final Event Selection: $\chi^2/d.o.f$ <5.2 and π^0 Pull of monoenergetic photon>1.50σ

branching fraction = 2.02%

Energy (MeV)	eff	eff*(1+δ)	eff*(1+δ)	eff*(1+δ)	eff*(1+δ)
	No ISR	Flat	Belle Y(4260)	Breit-Wignet Y(4260)	Y(4360) ISR
4010	24.541±0.269%	18.221±0.226%	18.120±0.220%	18.199±0.207%	17.674±0.204%
4230	25.533±0.271%	18.100±0.227%	18.538±0.205%	17.898±0.203%	17.896±0.201%
4260	25.301±0.270%	18.810±0.230%	19.661±0.209%	18.539±0.210%	17.898±0.202%
4360	25.475±0.274%	19.101±0.232%	20.588±0.244%	19.877±0.256%	18.640±0.205%
4420	24.996±0.271%	19.078±0.234%	20.028±0.252%	18.780±0.272%	20.204±0.252%
4600	25.405±0.275%	19.333±0.236%	18.252±0.267%	19.084±0.329%	17.163±0.305%

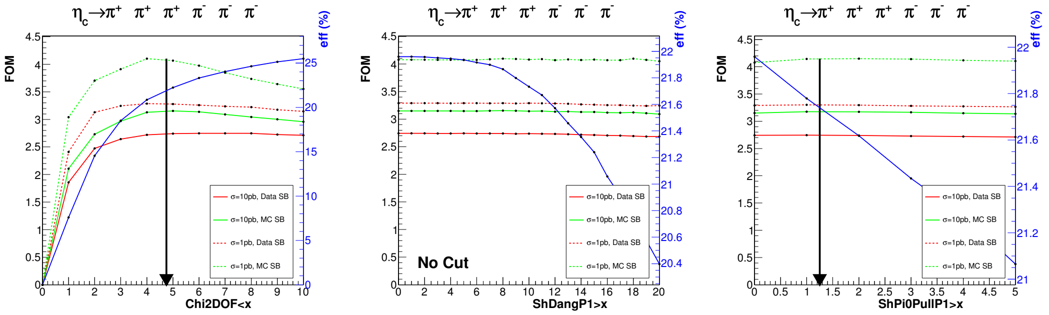

Figure B.5: (a) Optimization of $\chi^2/d.o.f$, (b) Optimization of angle between shower and closest charged track , (c) Optimization of rejecting the monoenergetic shower's π^0 pull

B.6 $\eta_c(1S) \to \pi^+\pi^+\pi^-\pi^-$

Final Event Selection: $\chi^2/d.o.f$ <3.5 and π^0 Pull of monoenergetic photon>1.75σ

branching fraction = 1.72%

Energy (MeV)	eff	eff*(1+δ)	eff*(1+δ)	eff*(1+δ)	eff*(1+δ)
	No ISR	Flat	Belle Y(4260)	Breit-Wignet Y(4260)	Y(4360) ISR
4010	37.191±0.356%	27.294±0.301%	26.963±0.292%	26.541±0.273%	26.466±0.271%
4230	37.216±0.360%	27.193±0.302%	27.031±0.268%	27.073±0.270%	26.631±0.269%
4260	37.887±0.362%	27.294±0.302%	28.201±0.276%	27.282±0.276%	26.354±0.265%
4360	37.674±0.363%	27.928±0.308%	29.059±0.315%	28.140±0.334%	27.538±0.274%
4420	37.691±0.360%	27.401±0.308%	28.349±0.330%	28.493±0.366%	29.482±0.329%
4600	38.143±0.367%	27.305±0.307%	27.599±0.357%	28.602±0.439%	25.758±0.410%

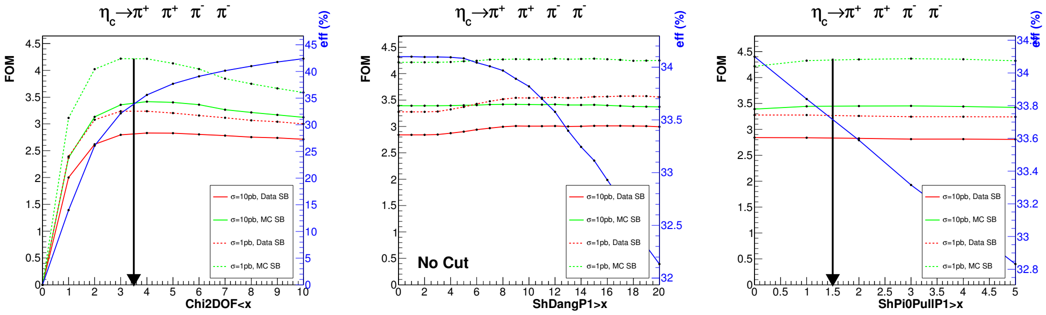

Figure B.6: (a) Optimization of $\chi^2/d.o.f$, (b) Optimization of angle between shower and closest charged track , (c) Optimization of rejecting the monoenergetic shower's π^0 pull

B.7 $\eta_c(1S) \rightarrow \pi^+\pi^-\eta$

Final Event Selection: $\chi^2/d.o.f$ <3.00 and θ(monoenergetic photon and closest charged track)>17.5$\circ$ and π^0 Pull of monoenergetic photon>4.00σ

branching fraction = 1.66%

Energy (MeV)	eff	eff*(1+δ)	eff*(1+δ)	eff*(1+δ)	eff*(1+δ)
	No ISR	Flat	Belle Y(4260)	Breit-Wignet Y(4260)	Y(4360) ISR
4010	27.793±0.318%	21.000±0.270%	18.535±0.252%	20.487±0.250%	19.918±0.245%
4230	27.815±0.318%	20.859±0.272%	19.040±0.232%	20.263±0.242%	19.902±0.239%
4260	27.948±0.316%	21.443±0.274%	20.209±0.237%	21.199±0.250%	19.913±0.238%
4360	28.103±0.319%	21.192±0.277%	20.909±0.271%	21.979±0.305%	21.021±0.244%
4420	28.177±0.320%	20.817±0.273%	20.346±0.288%	21.646±0.329%	23.073±0.303%
4600	28.237±0.322%	21.583±0.278%	19.480±0.309%	20.969±0.389%	19.519±0.366%

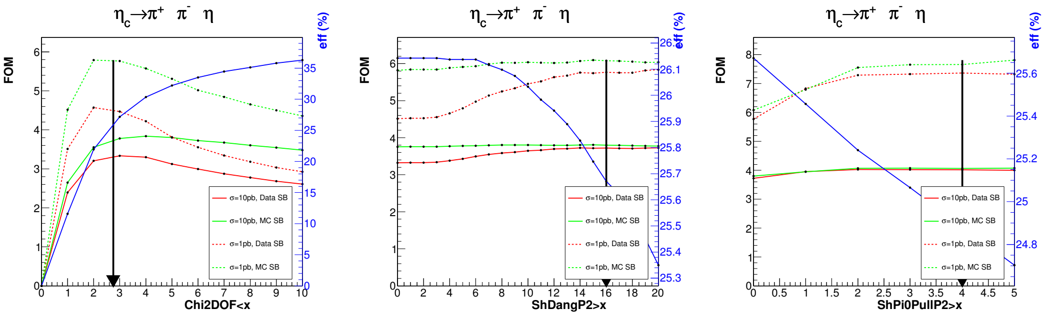

Figure B.7: (a) Optimization of $\chi^2/d.o.f$, (b) Optimization of angle between shower and closest charged track , (c) Optimization of rejecting the monoenergetic shower's π^0 pull

B.8 $\eta_c(1S) \rightarrow K^- K_S \pi^+ \pi^+ \pi^-$

Final Event Selection: $\chi^2/d.o.f$ <4.25, π^0 Pull of monoenergetic photon>1.75σ, Prob(K$^-$)>Prob(π^-) and $L/\sigma > 2$

branching fraction = 1.38%

Energy (MeV)	eff	eff*(1+δ)	eff*(1+δ)	eff*(1+δ)	eff*(1+δ)
	No ISR	Flat	Belle Y(4260)	Breit-Wignet Y(4260)	Y(4360) ISR
4010	18.388±0.279%	13.522±0.234%	13.877±0.232%	13.553±0.215%	12.965±0.214%
4230	18.958±0.282%	13.738±0.239%	14.591±0.216%	13.345±0.211%	13.379±0.212%
4260	18.884±0.283%	13.498±0.241%	15.233±0.218%	13.597±0.218%	12.866±0.206%
4360	19.706±0.288%	14.388±0.244%	15.278±0.248%	14.705±0.266%	14.092±0.214%
4420	18.889±0.285%	13.773±0.241%	14.853±0.259%	14.204±0.285%	14.707±0.261%
4600	19.438±0.287%	14.098±0.243%	13.859±0.279%	14.443±0.344%	12.512±0.316%

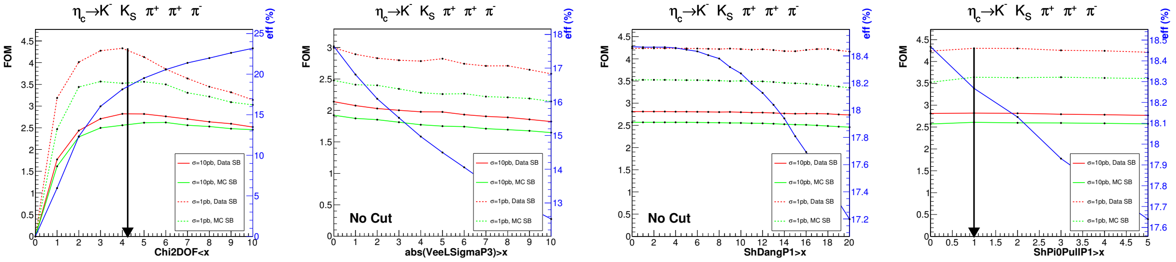

Figure B.8: (a) Optimization of $\chi^2/d.o.f$, (b) Optimization of decay length over error , (c) Optimization of angle between shower and closest charged track , (d) Optimization of rejecting the monoenergetic shower's π^0 pull

B.9 $\eta_c(1S) \to K^+ K_S \pi^+ \pi^- \pi^-$

Final Event Selection: $\chi^2/d.o.f$ <4.00, π^0 Pull of monoenergetic photon>2.00σ, Prob(K$^+$)>Prob(π^+) and $L/\sigma > 2$

branching fraction = 1.38%

Energy (MeV)	eff	eff*(1+δ)	eff*(1+δ)	eff*(1+δ)	eff*(1+δ)
	No ISR	Flat	Belle Y(4260)	Breit-Wignet Y(4260)	Y(4360) ISR
4010	17.856±0.274%	13.493±0.234%	13.504±0.230%	12.921±0.212%	13.106±0.213%
4230	18.546±0.278%	13.885±0.238%	13.813±0.211%	13.427±0.213%	13.135±0.210%
4260	18.681±0.282%	14.095±0.239%	15.020±0.216%	13.853±0.218%	13.481±0.209%
4360	18.956±0.285%	13.986±0.239%	15.547±0.248%	14.376±0.263%	14.070±0.215%
4420	18.729±0.282%	13.346±0.235%	14.677±0.258%	14.150±0.284%	15.017±0.260%
4600	18.838±0.283%	14.313±0.245%	13.545±0.275%	14.551±0.342%	12.560±0.314%

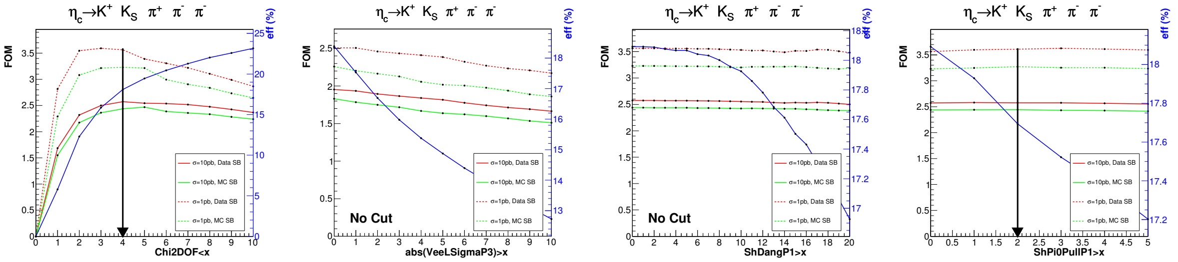

Figure B.9: (a) Optimization of $\chi^2/d.o.f$, (b) Optimization of decay length over error , (c) Optimization of angle between shower and closest charged track , (d) Optimization of rejecting the monoenergetic shower's π^0 pull

B.10 $\eta_c(1S) \to K^- K_S \pi^+$

Final Event Selection: $\chi^2/d.o.f$ <3.75 and π^0 Pull of monoenergetic photon>3.25σ and Prob(K$^-$)>Prob(π^-)

branching fraction = 1.30%

Energy (MeV)	eff	eff*(1+δ)	eff*(1+δ)	eff*(1+δ)	eff*(1+δ)
	No ISR	Flat	Belle Y(4260)	Breit-Wignet Y(4260)	Y(4360) ISR
4010	31.513±0.375%	23.830±0.325%	22.969±0.311%	23.286±0.292%	23.077±0.291%
4230	31.695±0.376%	23.250±0.321%	23.563±0.289%	23.091±0.284%	22.428±0.280%
4260	31.482±0.374%	23.968±0.325%	24.582±0.293%	23.438±0.295%	22.669±0.283%
4360	32.357±0.379%	23.947±0.325%	24.832±0.334%	24.815±0.358%	23.142±0.287%
4420	31.594±0.377%	23.131±0.321%	24.065±0.351%	23.190±0.381%	25.449±0.350%
4600	31.847±0.378%	23.875±0.326%	23.954±0.378%	23.718±0.458%	21.697±0.430%

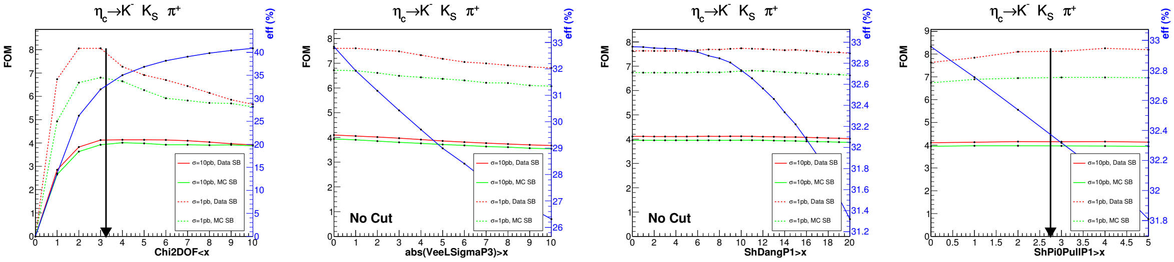

Figure B.10: (a) Optimization of $\chi^2/d.o.f$, (b) Optimization of decay length over error , (c) Optimization of angle between shower and closest charged track , (d) Optimization of rejecting the monoenergetic shower's π^0 pull

B.11 $\eta_c(1S) \to K^+ K_S \pi^-$

Final Event Selection: $\chi^2/d.o.f$ <4.25 and π^0 Pull of monoenergetic photon>3.00σ

and Prob(K$^+$)>Prob(π^+)

branching fraction = 1.30%

Energy (MeV)	eff	eff*(1+δ)	eff*(1+δ)	eff*(1+δ)	eff*(1+δ)
	No ISR	Flat	Belle Y(4260)	Breit-Wignet Y(4260)	Y(4360) ISR
4010	32.232±0.381%	24.698±0.327%	24.581±0.323%	24.143±0.301%	23.537±0.294%
4230	32.912±0.386%	24.301±0.325%	24.582±0.294%	24.251±0.292%	23.909±0.291%
4260	33.376±0.387%	24.849±0.329%	25.253±0.301%	24.784±0.302%	23.133±0.286%
4360	33.499±0.386%	25.299±0.332%	26.547±0.346%	26.073±0.365%	24.525±0.291%
4420	33.323±0.386%	24.393±0.327%	25.559±0.358%	25.318±0.390%	27.189±0.360%
4600	33.194±0.387%	24.824±0.334%	24.019±0.382%	24.774±0.466%	21.927±0.436%

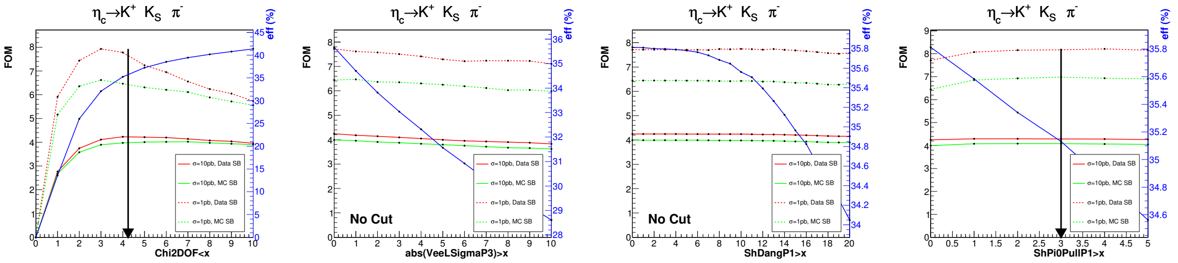

Figure B.11: (a) Optimization of $\chi^2/d.o.f$, (b) Optimization of decay length over error , (c) Optimization of angle between shower and closest charged track , (d) Optimization of rejecting the monoenergetic shower's π^0 pull

B.12 $\eta_c(1S) \to K^+K^-\pi^0$

Final Event Selection: $\chi^2/d.o.f$ <2.75 and π^0 Pull of monoenergetic photon>2.75σ and Prob(K$^+$)>Prob(π^+) and Prob(K$^-$)>Prob(π^-)

branching fraction = 1.04%

Energy (MeV)	eff	eff*(1+δ)	eff*(1+δ)	eff*(1+δ)	eff*(1+δ)
	No ISR	Flat	Belle Y(4260)	Breit-Wignet Y(4260)	Y(4360) ISR
4010	21.659±0.352%	16.337±0.302%	14.539±0.275%	16.263±0.277%	16.459±0.277%
4230	22.976±0.361%	16.744±0.306%	14.718±0.253%	16.508±0.273%	15.740±0.267%
4260	22.910±0.362%	16.727±0.305%	15.642±0.260%	16.276±0.277%	15.553±0.263%
4360	22.077±0.358%	16.458±0.304%	16.189±0.298%	17.434±0.340%	16.416±0.269%
4420	21.633±0.353%	16.271±0.302%	16.070±0.318%	16.693±0.359%	18.001±0.338%
4600	22.311±0.360%	16.691±0.304%	14.802±0.333%	16.637±0.427%	14.896±0.395%

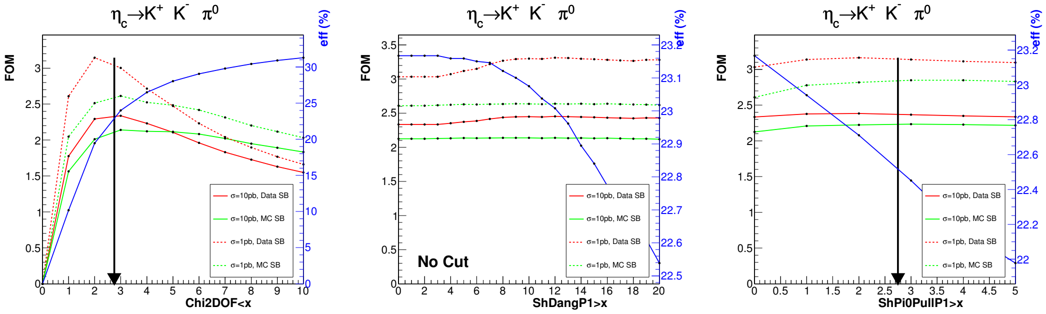

Figure B.12: (a) Optimization of $\chi^2/d.o.f$, (b) Optimization of angle between shower and closest charged track , (c) Optimization of rejecting the monoenergetic shower's π^0 pull

B.13 $\eta_c(1S) \to K^+K^-\pi^+\pi^-$

Final Event Selection: $\chi^2/d.o.f$ <3.00 and π^0 Pull of monoenergetic photon>1.50σ and Prob(K$^+$)>Prob(π^+) and Prob(K$^-$)>Prob(π^-)

branching fraction = 0.950%

Energy (MeV)	eff	eff*(1+δ)	eff*(1+δ)	eff*(1+δ)	eff*(1+δ)
	No ISR	Flat	Belle Y(4260)	Breit-Wignet Y(4260)	Y(4360) ISR
4010	25.837±0.397%	19.171±0.334%	18.991±0.324%	18.878±0.310%	17.846±0.300%
4230	26.367±0.403%	18.484±0.336%	19.083±0.298%	18.640±0.296%	18.084±0.294%
4260	26.755±0.402%	19.241±0.336%	19.739±0.302%	19.254±0.310%	18.822±0.297%
4360	26.941±0.407%	18.926±0.340%	20.381±0.349%	20.196±0.374%	19.167±0.301%
4420	26.969±0.405%	18.772±0.337%	19.452±0.362%	19.860±0.410%	20.387±0.367%
4600	26.964±0.407%	19.667±0.344%	19.141±0.393%	19.182±0.492%	17.324±0.450%

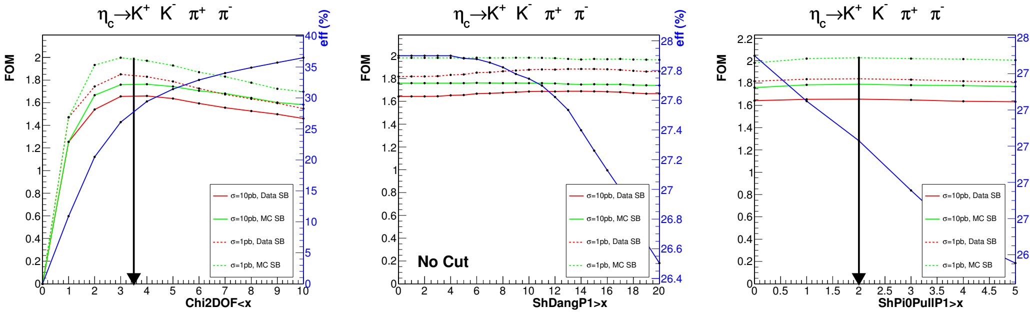

Figure B.13: (a) Optimization of $\chi^2/d.o.f$, (b) Optimization of angle between shower and closest charged track , (c) Optimization of rejecting the monoenergetic shower's π^0 pull

B.14 $\eta_c(1S) \to K^+K^-\pi^+\pi^+\pi^-\pi^-$

Final Event Selection: $\chi^2/d.o.f$ <4.00 and π^0 Pull of monoenergetic photon>2.50σ

and Prob(K$^+$)>Prob(π^+) and Prob(K$^-$)>Prob(π^-)

branching fraction = 0.830%

Energy (MeV)	eff	eff*(1+δ)	eff*(1+δ)	eff*(1+δ)	eff*(1+δ)
	No ISR	Flat	Belle Y(4260)	Breit-Wignet Y(4260)	Y(4360) ISR
4010	13.956±0.309%	9.663±0.258%	10.173±0.255%	10.039±0.238%	9.677±0.235%
4230	14.443±0.318%	10.666±0.270%	11.279±0.239%	10.490±0.239%	9.940±0.237%
4260	14.962±0.318%	10.169±0.266%	11.764±0.245%	10.344±0.245%	10.577±0.234%
4360	14.619±0.321%	10.460±0.266%	11.781±0.276%	10.891±0.295%	10.933±0.244%
4420	14.870±0.324%	10.788±0.273%	11.403±0.294%	10.803±0.323%	11.559±0.289%
4600	14.758±0.322%	11.227±0.278%	11.553±0.328%	11.285±0.392%	9.950±0.360%

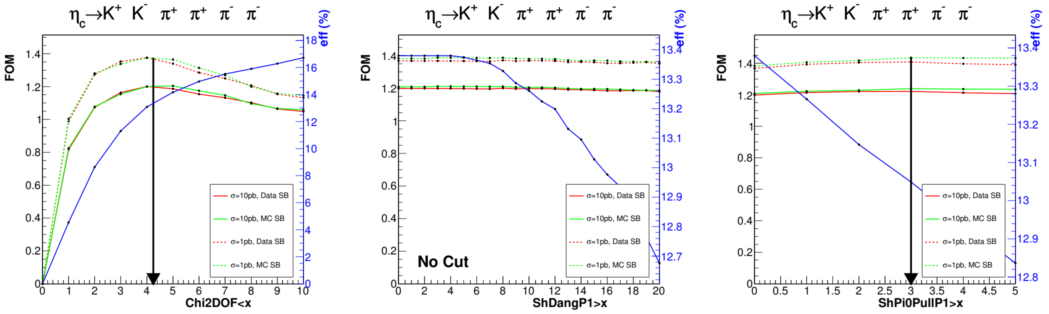

Figure B.14: (a) Optimization of $\chi^2/d.o.f$, (b) Optimization of angle between shower and closest charged track , (c) Optimization of rejecting the monoenergetic shower's π^0 pull

Chapter C

Simultaneous fit results

The plots below are the resulting fits to each $\eta_c(1S)$ decay channel at center of mass energies: 4.01, 4.23, 4.26, 4.36, 4.42, and 4.60 GeV. Since at any energy the difference between any of the ISR assumptions or observed cross section fits shape are indistinguishable we show only the lineshape for the BW Y(4260) assumption.

Energy (MeV)	$N_{observed}(e^+e^- \to \gamma\eta_c)$	$\sigma_{observed}(e^+e^- \to \gamma\eta_c)$	Significance (σ)	χ^2/bin
4010	60 ± 368	0.12 ± 0.76 pb	0.15 σ	73.22 / 90
4230	1373 ± 496	1.26 ± 0.45 pb	2.66 σ	80.11 / 90
4260	1191 ± 438	1.44 ± 0.53 pb	2.81 σ	101.49 / 90
4360	966 ± 336	1.79 ± 0.62 pb	3.19 σ	71.77 / 90
4420	264 ± 386	0.25 ± 0.36 pb	0.64 σ	103.64 / 90
4600	-75 ± 230	-0.13 ± 0.40 pb	0.00 σ	64.35 / 90

Table C.1: The observed cross section, significance, and χ^2/bin when fitting each energy independently. The errors shown are statistical only.

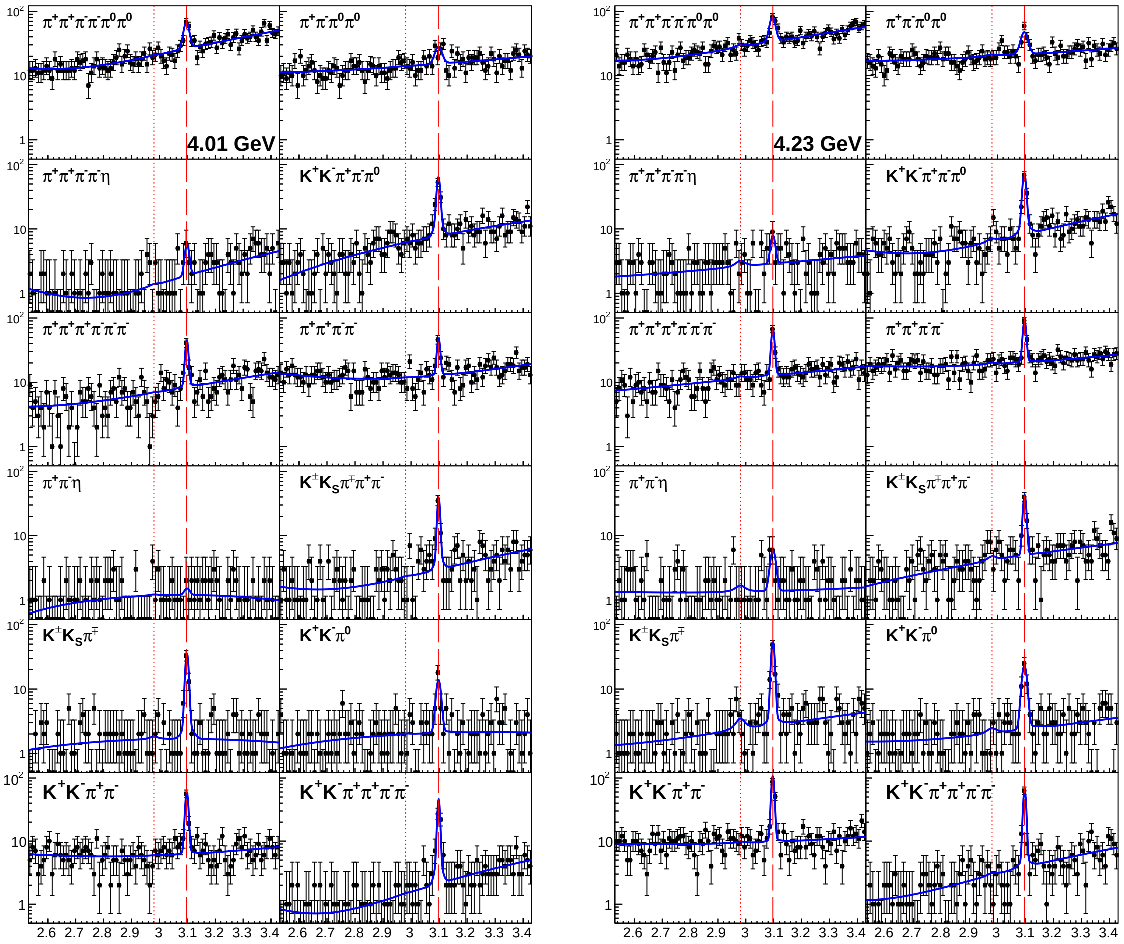

Figure C.1: The recoil-mass distribution of the transition photon for each $\eta_c(1S)$ decay channel at center-of-mass energy 4.01 GeV (left) and 4.26 GeV (right). Projections from the simultaneous fit are overlaid. A dotted line indicates the $\eta_c(1S)$ mass; a dashed line indicates the J/ψ mass.

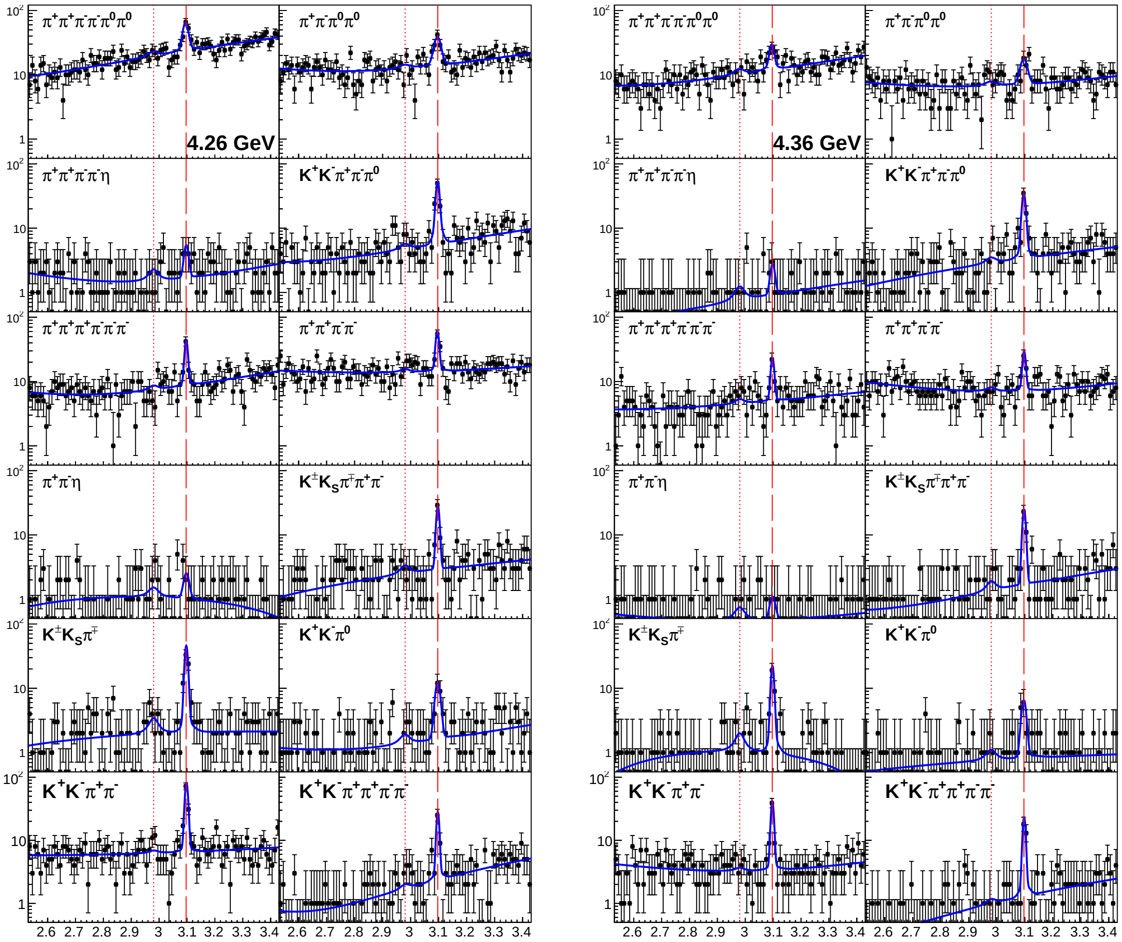

Figure C.2: The recoil-mass distribution of the transition photon for each $\eta_c(1S)$ decay channel at center-of-mass energy 4.26 GeV (left) and 4.36 GeV (right). Projections from the simultaneous fit are overlaid. A dotted line indicates the $\eta_c(1S)$ mass; a dashed line indicates the J/ψ mass.

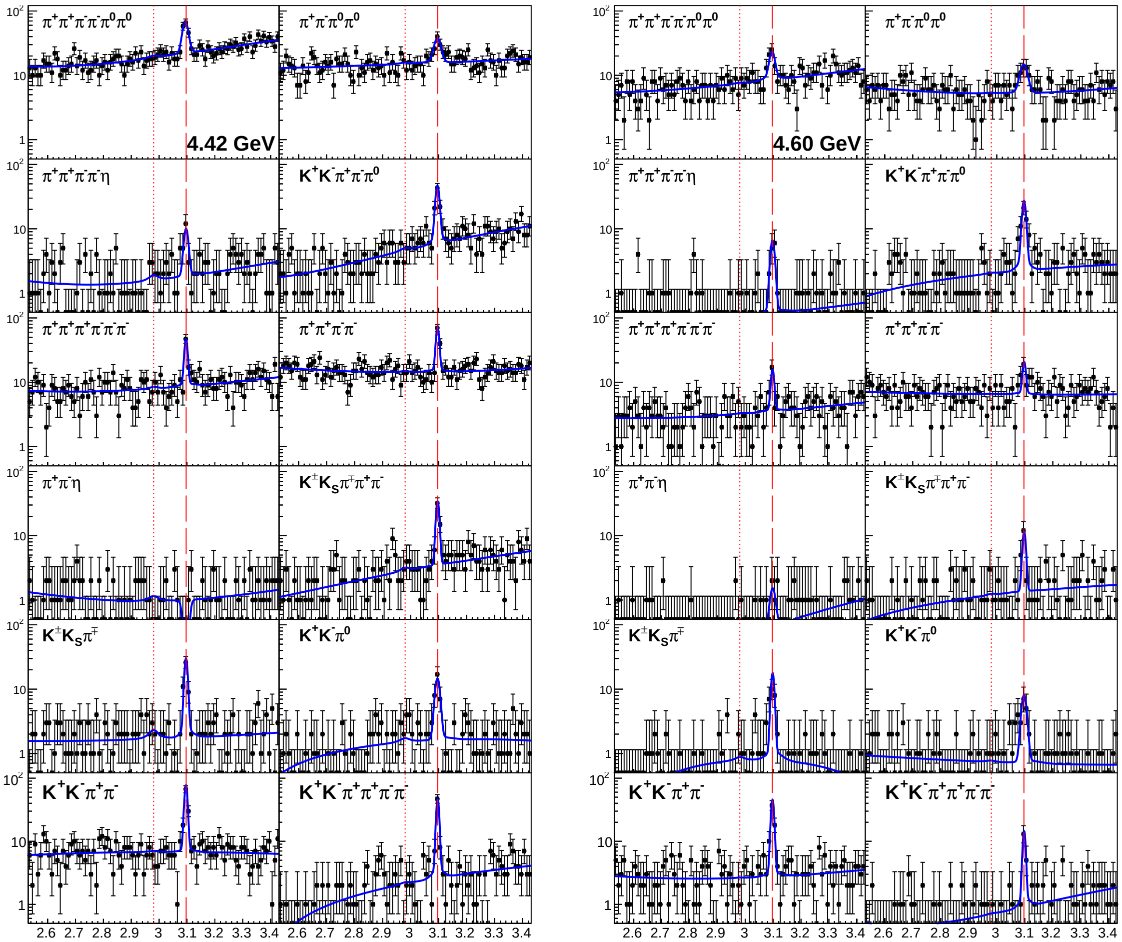

Figure C.3: The recoil-mass distribution of the transition photon for each $\eta_c(1S)$ decay channel at center-of-mass energy 4.42 GeV (left) and 4.60 GeV (right). Projections from the simultaneous fit are overlaid. A dotted line indicates the $\eta_c(1S)$ mass; a dashed line indicates the J/ψ mass.

Bibliography

[1] http://annwm.lbl.gov/g4/g4.cgi.

[2] Georges Aad et al. Observation of a new particle in the search for the Standard Model Higgs boson with the ATLAS detector at the LHC. *Phys. Lett.*, B716:1–29, 2012.

[3] M. Ablikim. Observation of a Charged Charmoniumlike Structure $Z_c(4020)$ and Search for the $Z_c(3900)$ in $e^+e^- \to {}^{+-}h_c$. *Phys. Rev. Lett.*, 111(24):242001, 2013.

[4] M. Ablikim. Search for hadronic transition ${}_{cJ}{}_{c}{}^{+-}$ and observation of ${}_{cJ}K\overline{K}$. *Phys. Rev.*, D87(1):012002, 2013.

[5] M. Ablikim. Precision measurement of the integrated luminosity of the data taken by BESIII at center of mass energies between 3.810 GeV and 4.600 GeV. *Chin. Phys.*, C39(9):093001, 2015.

[6] M. Ablikim et al. Determination of the psi(3770), psi(4040), psi(4160) and psi(4415) resonance parameters. *eConf*, C070805:02, 2007. [Phys. Lett.B660,315(2008)].

[7] M. Ablikim et al. Design and Construction of the BESIII Detector. *Nucl. Instrum. Meth.*, A614:345–399, 2010.

[8] M. Ablikim et al. Observation of χ_{c1} decays into vector meson pairs $\phi\phi$, $\omega\omega$, and $\omega\phi$. *Phys. Rev. Lett.*, 107:092001, 2011.

[9] M. Ablikim et al. Study of χ_{cJ} radiative decays into a vector meson. *Phys. Rev. D*, 83:112005, 2011.

[10] M. Ablikim et al. Study of $\psi(3686) \to \pi^0 h_c, h_c \to \gamma\eta_c$ via η_c exclusive decays. *Phys. Rev.*, D86:092009, 2012.

[11] M. Ablikim et al. Evidence for c(2S) in (3686)KS0K+-. *Phys. Rev. D*, 87(5):no. 5, 052005, 2013.

[12] M. Ablikim et al. Observation of a Charged Charmoniumlike Structure in e^+e^- $^{+-}$ J/ at $\sqrt{s}$ =4.26GeV. *Phys. Rev. Lett.*, 110:252001, 2013.

[13] M. Ablikim et al. Amplitude analysis of the ^{00} system produced in radiative J/ decays. *Phys. Rev. D*, 92(5):052003, 2015. [Erratum: Phys. Rev.D **93**, no.3, 039906 (2016)].

[14] M. Ablikim et al. Evidence for $e^+e^- \to \gamma\chi_{c1,2}$ at center-of-mass energies from 4.009 to 4.360 GeV. *Chin. Phys.*, C39(4):041001, 2015.

[15] S. Actis et al. Quest for precision in hadronic cross sections at low energy: Monte Carlo tools vs. experimental data. *Eur. Phys. J.*, C66:585–686, 2010.

[16] G. S. Adams. Measurement of Gamma(ee)(J/psi), Gamma(tot)(J/psi), and Gamma(ee)[psi(2S)]/Gamma(ee)(J/psi). *Phys. Rev.*, D73:051103, 2006.

[17] S. Agostinelli et al. GEANT4: A Simulation toolkit. *Nucl. Instrum. Meth.*, A506:250–303, 2003.

[18] V. V. Anashin. Measurement of $\mathcal{B}(J/\psi \to \eta_c\gamma)$ at KEDR. *Int. J. Mod. Phys. Conf. Ser.*, 02:188–192, 2011.

[19] D. M. Asner et al. Physics at BES-III. *Int. J. Mod. Phys.*, A24:S1–794, 2009.

[20] Bernard Aubert et al. Observation of a broad structure in the $\pi^+\pi^-J/\psi$ mass spectrum around 4.26-GeV/c^2. *Phys. Rev. Lett.*, 95:142001, 2005.

[21] Bernard Aubert et al. Evidence of a broad structure at an invariant mass of 4.32- GeV/c^2 in the reaction $e^+e^- \to \pi^+\pi^-\psi_{2S}$ measured at BaBar. *Phys. Rev. Lett.*, 98:212001, 2007.

[22] Bernard Aubert et al. Evidence of a broad structure at an invariant mass of 4.32- GeV/c^2 in the reaction $e^+e^- \to \pi^+\pi^-\psi_{2S}$ measured at BaBar. *Phys. Rev. Lett.*, 98:212001, 2007.

[23] J. J. Aubert et al. Experimental Observation of a Heavy Particle J. *Phys. Rev. Lett.*, 33:1404–1406, 1974.

[24] J. E. Augustin et al. Discovery of a Narrow Resonance in e+ e- Annihilation. *Phys. Rev. Lett.*, 33:1406–1408, 1974. [Adv. Exp. Phys.5,141(1976)].

[25] Paul Avery. Applied fitting theory vi: Formulas for kinematic fitting. *CLEO Note CBX*, pages 98–37, 1998.

[26] T. Barnes, F. E. Close, and E. S. Swanson. Hybrid and conventional mesons in the flux tube model: Numerical studies and their phenomenological implications. *Phys. Rev. D*, 52:5242–5256, Nov 1995.

[27] T. Barnes, S. Godfrey, and E. S. Swanson. Higher charmonia. *Phys. Rev.*, D72:054026, 2005.

[28] G Barrand et al. Gaudia software architecture and framework for building hep data processing applications. *Computer Physics Communications*, 140(1):45–55, 2001.

[29] N. Brambilla et al. Heavy quarkonium: progress, puzzles, and opportunities. *Eur. Phys. J.*, C71:1534, 2011.

[30] Nora Brambilla, Yu Jia, and Antonio Vairo. Model-independent study of magnetic dipole transitions in quarkonium. *Phys. Rev.*, D73:054005, 2006.

[31] Nora Brambilla, Antonio Pineda, Joan Soto, and Antonio Vairo. Effective field theories for heavy quarkonium. *Rev. Mod. Phys.*, 77:1423, 2005.

[32] Serguei Chatrchyan et al. Observation of a new boson at a mass of 125 GeV with the CMS experiment at the LHC. *Phys. Lett.*, B716:30–61, 2012.

[33] Wikimedia Commons. Magnetic field of an idealized quadrupole with forces, 2012.

[34] D. Cronin-Hennessy et al. Measurement of Charm Production Cross Sections in e+e- Annihilation at Energies between 3.97 and 4.26-GeV. *Phys. Rev.*, D80:072001, 2009.

[35] Gui-Jun Ding, Jie-Jie Zhu, and Mu-Lin Yan. Canonical Charmonium Interpretation for Y(4360) and Y(4660). *Phys. Rev.*, D77:014033, 2008.

[36] V. Druzhinin. ISR physics at BABAR. In *Particle physics at the year of 250th anniversary of Moscow University. Proceedings, 12th Lomonosov Conference on elementary particle physics, Moscow, Russia, August 25-31*, pages 303–307, 2006.

[37] V. P. Druzhinin, S. I. Eidelman, S. I. Serednyakov, and E. P. Solodov. Hadron Production via e+e- Collisions with Initial State Radiation. *Rev. Mod. Phys.*, 83:1545, 2011.

[38] Jozef J. Dudek, Robert Edwards, and Christopher E. Thomas. Exotic and excited-state radiative transitions in charmonium from lattice QCD. *Phys. Rev.*, D79:094504, 2009.

[39] Estia Eichten, Stephen Godfrey, Hanna Mahlke, and Jonathan L. Rosner. Quarkonia and their transitions. *Rev. Mod. Phys.*, 80:1161–1193, 2008.

[40] Shou-Xian Fang and Sen-Yu Chen. The Beijing Electron Positron Collider. *Part. Accel.*, 26:51–61, 1990.

[41] F. Halzen and Alan D. Martin. *Quarks and Leptons: An Introductory Course in Modern Particle Physics*. 1984.

[42] Kotoyo Hoshina, Keisuke Fujii, and Osamu Nitoh. Development of a geant4 solid for stereo mini-jet cells in a cylindrical drift chamber. *arXiv preprint hep-ex/0303014*, 2003.

[43] F. Iddir and L. Semlala. Theoretical investigations on the Y(4260) being an hybrid meson. 2006.

[44] S. Jadach, B. F. L. Ward, and Z. Was. The Precision Monte Carlo event generator K K for two fermion final states in e+ e- collisions. *Comput. Phys. Commun.*, 130:260–325, 2000.

[45] Fred James et al. Minuit. *CERN program library long writeup D*, 506:1993, 1994.

[46] B. Z. Kopeliovich and A. H. Rezaeian. Applied High Energy QCD. *Int. J. Mod. Phys.*, E18:1629–1696, 2009. [,51(2008)].

[47] D. J. Lange. The EvtGen particle decay simulation package. *Nucl. Instrum. Meth.*, A462:152–155, 2001.

[48] Shyh-Yuan Lee. *Accelerator physics*. World scientific, 2004.

[49] Bo Liu, Mengping Gu, Chuang Zhang, and Yunlong Chi. New Electron Gun System for BEPCII . In *Particle Accelerator Conference, Knoxville, Tennessee*, 2005.

[50] Z. Q. Liu et al. Study of $e^+e^- \to \pi^+\pi^- J/\psi$ and Observation of a Charged Charmoniumlike State at Belle. *Phys. Rev. Lett.*, 110:252002, 2013.

[51] Z. Q. Liu, X. S. Qin, and C. Z. Yuan. Combined fit to BaBar and Belle data on $e^+e^- \to \pi^+\pi^-\psi(2S)$. *Phys. Rev.*, D78:014032, 2008.

[52] Michel Loève. *Probability Theory, Vol 1.* New York: D. Van Nostrand Company, 1955.

[53] L. Maiani, V. Riquer, F. Piccinini, and A. D. Polosa. Four quark interpretation of Y(4260). *Phys. Rev.*, D72:031502, 2005.

[54] Johan Messchendorp. Physics with Charmonium – A few recent highlights of BESIII. *PoS*, Bormio2013:043, 2013.

[55] R. E. Mitchell. J/psi and psi(2S) Radiative Decays to eta(c). *Phys. Rev. Lett.*, 102:011801, 2009. [Erratum: Phys. Rev. Lett.106,159903(2011)].

[56] K. A. Olive et al. Review of Particle Physics. *Chin. Phys.*, C38:090001, 2014.

[57] Xin Ouyang. Survey and Alignment for the BEPCII Storage Ring. *eConf*, C0211115:043, 2002.

[58] Donald H. Perkins. *Introduction to High Energy Physics.* Cambridge University Press, 2000.

[59] Qian Wang, Christoph Hanhart, and Qiang Zhao. Decoding the riddle of $Y(4260)$ and $Z_c(3900)$. *Phys. Rev. Lett.*, 111(13):132003, 2013.

[60] X. L. Wang et al. Observation of Two Resonant Structures in e+e- to pi+ pi- psi(2S) via Initial State Radiation at Belle. *Phys. Rev. Lett.*, 99:142002, 2007.

[61] Guang-Zhi Xu, Yi-Jie Li, Kui-Yong Liu, and Yu-Jie Zhang. $\alpha_s v^2$ corrections to η_c and χ_{cJ} production recoiled with a photon at e^+e^- colliders. *JHEP*, 10:71, 2014.

[62] C. Zhang. Status of BEPC and plan of BEPCII. In *High luminosity e+e- colliders. Proceedings, 23rd Advanced ICFA Beam Dynamics Workshop, Factories 2001, Ithaca, USA, October 15-19, 2001*, 2001.

[63] Chuang Zhang, Li Ma, Guoxi Pei, and Jiuqing Wang. Construction and Commissioning of BEPCII. In *Particle accelerator. Proceedings, 23rd Conference, PAC'09, Vancouver, Canada, May 4-8, 2009*, page MO3RAI03, 2010.

Manuel Lara

Indiana University, Department of Physics
727 E. Third St. Swain Hall West, Bloomington, IN 47405-7105
812-250-1337 | manlara@gmail.com

Education

July 2016	Ph.D in Physics, **Indiana University**, Bloomington Thesis: "Evidence for $e^+e^- \to \gamma\eta_c(1S)$ at center of mass energies between 4.01 and 4.60 GeV at BESIII" Advisors: Dr. Ryan Mitchell and Dr. Matthew Shepherd
Dec 2012	Master of Science in Physics, **Indiana University**, Bloomington
Aug 2009	Bachelor of Science in Mathematics and Physics, **University of Texas-Pan American**, Edinburg

Employment

Research Experience

Jan 2011- July 2016	Graduate Research Assistant *Indiana University* Worked on two distinct high energy physics experiments, they were: GlueX (at Thomas Jefferson National Lab in Virginia) and BESIII (at the Institute of High Energy Physics in Beijing). Helped build, maintain, and operate an electromagnetic calorimeter for the GlueX experiment. For the BESIII experiment, performed calibration studies of the BESIII Time-of-Flight system and studied the process $e^+e^- \to \gamma\eta_c(1S)$ for thesis.
2006-2009	Undergraduate Research Assistant *University of Texas-Pan American* Worked in computational physics studying periodicity in a certain class of differential equations. Worked in a signal processing lab studying synthetic aperture radar systems.

Teaching Experience

JUNE 2012	Instructor *Foundations in Science and Mathematics* Taught Physics in two-week program to high school students.
FALL 2010	Graduate Teaching Assistant *Indiana University* Taught basic science concepts to education majors.
FALL 2009-SPRING 2010	Graduate Teaching Assistant *University of Texas-Pan American* Taught Calculus based Physics to engineering majors.
FALL 2006-SPRING 2009	Mathematics and Physics Tutor *Learning Center, University of Texas-Pan American* Tutored university students in all levels of mathematics, physics, and mechanical engineering.

HONORS/AWARDS

2012-2016	Alliance for Graduate Education and Professoriate Scholar (AGEP)
2011	IU Physics Department Konopinski Award for Outstanding Teaching
2007-2009	Dean's List
2007, 2008	Undergraduate Research Initiative Summer Grant

SELECTED PUBLICATIONS

M. Bhatti, M. Lara, and P. Bracken, "Periodic Solutions of the Duffing Equation", *International Journal of Mathematics*, Vol. 2, 2008, no. 8, 365 - 372,

TALKS

Radiative Transitions of the Y(4260) at BES. *April APS Nuclear Physics Meeting* (April 2014 and 2015)

Radiative Transitions to $\gamma\eta_c(1S)$ at 4.01-4.60 GeV *BESIII Physics and Software Workshop*, Beijing, P.R. China (September 2014)

FCAL Update *GlueX Collaboration Meeting*, Jefferson Lab, Newport News, VA (October 2014)

Full Publication List

M. Ablikim *et al.* [BESIII Collaboration], Eur. Phys. J. C **76** (2016) no.7, 369 [arXiv:1605.00068 [hep-ex]].

M. Ablikim *et al.* [BESIII Collaboration], Phys. Rev. Lett. **116** (2016) no.25, 251802 [arXiv:1603.04936 [hep-ex]].

M. Ablikim *et al.* [BESIII Collaboration], Phys. Rev. D **93** (2016) no.7, 072008 [arXiv:1602.07405 [hep-ex]].

M. Ablikim *et al.* [BESIII Collaboration], Phys. Rev. D **93** (2016) no.7, 072003 [arXiv:1602.06754 [hep-ex]].

M. Ablikim *et al.* [BESIII Collaboration], Phys. Rev. D **93** (2016) no.11, 112011 [arXiv:1602.01523 [hep-ex]].

M. Ablikim *et al.* [BESIII Collaboration], Phys. Rev. D **93** (2016) no.5, 052010 [arXiv:1512.08197 [hep-ex]].

M. Ablikim *et al.* [BESIII Collaboration], Phys. Rev. Lett. **116** (2016) no.8, 082001 [arXiv:1512.06998 [hep-ex]].

M. Ablikim *et al.* [BESIII Collaboration], Phys. Rev. D **93** (2016) no.1, 011102 [arXiv:1511.08564 [hep-ex]].

M. Ablikim *et al.* [BESIII Collaboration], Phys. Rev. Lett. **116** (2016) no.5, 052001 [arXiv:1511.08380 [hep-ex]].

M. Ablikim *et al.* [BESIII Collaboration], Phys. Lett. B **753** (2016) 103 [arXiv: 1511.01203 [hep-ex]].

M. Ablikim *et al.* [BESIII Collaboration], Chin. Phys. C **40** (2016) no.6, 063001 [arXiv:1510.08654 [hep-ex]].

M. Ablikim *et al.* [BESIII Collaboration], Phys. Rev. Lett. **115** (2015) no.22, 221805 [arXiv:1510.02610 [hep-ex]].

M. Ablikim *et al.* [BESIII Collaboration], Phys. Rev. D **92** (2015) no.11, 112008 [arXiv:1510.00308 [hep-ex]].

M. Ablikim *et al.* [BESIII Collaboration], Phys. Rev. Lett. **115** (2015) no.22, 222002 [arXiv:1509.05620 [hep-ex]].

M. Ablikim *et al.* [BESIII Collaboration], Phys. Rev. D **92** (2015) no.9, 092006 [arXiv:1509.01398 [hep-ex]].

M. Ablikim *et al.* [BESIII Collaboration], Phys. Rev. D **92** (2015) no.7, 072012 [arXiv:1508.07560 [hep-ex]].

M. Ablikim *et al.* [BESIII Collaboration], Phys. Rev. D **92** (2015) no.7, 071101 [arXiv:1508.00151 [hep-ex]].

M. Ablikim *et al.* [BESIII Collaboration], Phys. Lett. B **753** (2016) 629 [arXiv: 1507.08188 [hep-ex]].

M. Ablikim *et al.* [BESIII Collaboration], Phys. Rev. Lett. **116** (2016) no.4, 042001 [arXiv:1507.06824 [hep-ex]].

M. Ablikim *et al.* [BESIII Collaboration], Phys. Rev. D **92** (2015) no.5, 051101 [arXiv:1507.06734 [hep-ex]].

M. Ablikim *et al.* [BESIII Collaboration], Phys. Rev. Lett. **115** (2015) no.18, 182002 [arXiv:1507.02404 [hep-ex]].

M. Ablikim *et al.* [BESIII Collaboration], Phys. Rev. D **92** (2015) no.3, 032009 [arXiv:1507.02068 [hep-ex]].

M. Ablikim *et al.* [BESIII Collaboration], Phys. Lett. B **750** (2015) 466 [arXiv: 1506.08952 [hep-ex]].

M. Ablikim *et al.* [BESIII Collaboration], Phys. Rev. Lett. **115** (2015) no.11, 112003 [arXiv:1506.06018 [hep-ex]].

M. Ablikim *et al.* [BESIII Collaboration], Phys. Rev. D **92** (2015) 012014 [arXiv: 1506.05360 [hep-ex]].

M. Ablikim *et al.* [BESIII Collaboration], Phys. Rev. Lett. **115** (2015) no.9, 091803 [arXiv:1506.04807 [hep-ex]].

M. Ablikim *et al.* [BESIII Collaboration], Phys. Rev. D **92** (2015) no.5, 052003 Erratum: [Phys. Rev. D **93** (2016) no.3, 039906] [arXiv:1506.00546 [hep-ex]].

M. Ablikim *et al.* [BESIII Collaboration], Phys. Rev. D **92** (2015) no.1, 012007 [arXiv:1505.06283 [hep-ex]].

M. Ablikim *et al.* [BESIII Collaboration], Phys. Rev. D **91** (2015) no.11, 112015 [arXiv:1505.03087 [hep-ex]].

M. Ablikim *et al.* [BESIII Collaboration], Phys. Lett. B **749** (2015) 414 [arXiv: 1505.02559 [hep-ex]].

M. Ablikim *et al.* [BESIII Collaboration], Phys. Rev. D **92** (2015) no.1, 012008 [arXiv:1505.00539 [hep-ex]].

M. Ablikim *et al.* [BESIII Collaboration], Phys. Rev. D **91** (2015) no.9, 092009 [arXiv:1504.07450 [hep-ex]].

M. Ablikim *et al.* [BESIII Collaboration], Phys. Rev. D **92** (2015) no.1, 012001 [arXiv:1504.06016 [hep-ex]].

M. Ablikim *et al.* [BESIII Collaboration], Phys. Rev. D **91** (2015) no.11, 112004 [arXiv:1504.02680 [hep-ex]].

M. Ablikim *et al.* [BESIII Collaboration], Phys. Rev. D **91** (2015) no.11, 112001 [arXiv:1504.03194 [hep-ex]].

M. Ablikim *et al.* [BESIII Collaboration], Phys. Rev. D **91** (2015) no.9, 092006 [arXiv:1504.02025 [hep-ex]].

M. Ablikim *et al.* [BESIII Collaboration], Phys. Rev. Lett. **115** (2015) no.1, 011803 [arXiv:1503.08203 [hep-ex]].

M. Ablikim *et al.* [BESIII Collaboration], Phys. Rev. D **91** (2015) no.11, 112005 [arXiv:1503.06644 [hep-ex]].

M. Ablikim *et al.* [BESIII Collaboration], Phys. Rev. D **91** (2015) no.11, 112008 [arXiv:1503.04699 [hep-ex]].

M. Ablikim *et al.* [BESIII Collaboration], Chin. Phys. C **39** (2015) no.9, 093001 [arXiv:1503.03408 [hep-ex]].

M. Ablikim *et al.* [BESIII Collaboration], Phys. Rev. D **91** (2015) no.11, 112018 [arXiv:1502.02641 [hep-ex]].

M. Ablikim *et al.* [BESIII Collaboration], Phys. Lett. B **744** (2015) 339 [arXiv: 1501.01378 [hep-ex]].

M. Ablikim *et al.* [BESIII Collaboration], Phys. Rev. D **91** (2015) no.5, 052017 [arXiv:1412.5258 [hep-ex]].

M. Ablikim *et al.* [BESIII Collaboration], Phys. Rev. D **91** (2015) no.3, 031101 [arXiv:1412.4566 [hep-ex]].

M. Ablikim *et al.* [BESIII Collaboration], Phys. Rev. D **91** (2015) no.3, 032002 [arXiv:1412.1867 [hep-ex]].

M. Ablikim *et al.* [BESIII Collaboration], Chin. Phys. C **39** (2015) no.4, 041001 [arXiv:1411.6336 [hep-ex]].

M. Ablikim *et al.* [BESIII Collaboration], Phys. Rev. D **90** (2014) no.11, 112014 [arXiv:1410.8426 [hep-ex]].

M. Ablikim *et al.* [BESIII Collaboration], Phys. Rev. Lett. **114** (2015) no.9, 092003 [arXiv:1410.6538 [hep-ex]].

M. Ablikim *et al.* [BESIII Collaboration], Phys. Rev. Lett. **113** (2014) no.21, 212002 [arXiv:1409.6577 [hep-ex]].

M. Ablikim *et al.* [BESIII Collaboration], Phys. Rev. D **90** (2014) no.9, 092002 [arXiv:1409.4040 [hep-ex]].

M. Ablikim *et al.* [BESIII Collaboration], Phys. Rev. D **90** (2014) no.5, 052009 Addendum: [Phys. Rev. D **91** (2015) no.3, 039901] [arXiv:1408.3938 [hep-ex]].

M. Ablikim *et al.* [BESIII Collaboration], Phys. Rev. D **90** (2014) no.3, 032007 [arXiv:1406.2486 [hep-ex]].

M. Ablikim *et al.* [BESIII Collaboration], Phys. Rev. D **89** (2014) no.11, 112005 [arXiv:1405.3190 [hep-ex]].

M. Ablikim *et al.* [BESIII Collaboration], Phys. Rev. D **89** (2014) no.11, 112006 [arXiv:1405.1571 [hep-ex]].

M. Ablikim *et al.* [BESIII Collaboration], Phys. Rev. D **90** (2014) no.1, 012001 [arXiv:1405.1076 [hep-ex]].

M. Ablikim *et al.* [BESIII Collaboration], Phys. Lett. B **734** (2014) 227 [arXiv: 1404.4691 [hep-ex]].

M. Ablikim *et al.* [BESIII Collaboration], Phys. Rev. Lett. **112** (2014) 251801 Addendum: [Phys. Rev. Lett. **113** (2014) no.3, 039903] [arXiv:1404.0096 [hep-ex]].

M. Ablikim *et al.* [BESIII Collaboration], Phys. Rev. D **89** (2014) no.9, 092008 [arXiv:1403.7042 [hep-ex]].

M. Ablikim *et al.* [BESIII Collaboration], Phys. Lett. B **735** (2014) 101 [arXiv: 1403.6011 [hep-ex]].

M. Ablikim *et al.* [BESIII Collaboration], Phys. Rev. D **89** (2014) no.7, 071101 [arXiv:1402.4025 [hep-ex]].

M. Ablikim *et al.* [BESIII Collaboration], Phys. Rev. D **89** (2014) no.7, 074030 [arXiv:1402.2023 [hep-ex]].

M. Ablikim *et al.* [BESIII Collaboration], Phys. Rev. D **89** (2014) no.5, 052001 [arXiv:1401.3083 [hep-ex]].

M. Ablikim *et al.* [BESIII Collaboration], Phys. Rev. D **89** (2014) no.5, 051104 [arXiv:1312.0374 [hep-ex]].

M. Ablikim *et al.* [BESIII Collaboration], Phys. Rev. D **88** (2013) no.11, 112001 [arXiv:1310.6099 [hep-ex]].

M. Ablikim *et al.* [BESIII Collaboration], Phys. Rev. D **88** (2013) no.11, 112007 [arXiv:1310.5826 [hep-ex]].

M. Ablikim *et al.* [BESIII Collaboration], Phys. Rev. Lett. **112** (2014) no.9, 092001 [arXiv:1310.4101 [hep-ex]].

M. Ablikim *et al.* [BESIII Collaboration], Phys. Rev. Lett. **112** (2014) no.2, 022001 [arXiv:1310.1163 [hep-ex]].

M. Ablikim *et al.* [BESIII Collaboration], Phys. Rev. Lett. **111** (2013) no.24, 242001 [arXiv:1309.1896 [hep-ex]].

M. Ablikim *et al.* [BESIII Collaboration], Phys. Rev. Lett. **112** (2014) no.13, 132001 [arXiv:1308.2760 [hep-ex]].

M. Ablikim *et al.* [BESIII Collaboration], Phys. Rev. D **88** (2013) no.3, 032007 [arXiv:1307.1189].

M. Ablikim *et al.* [BESIII Collaboration], Phys. Rev. D **88** (2013) no.9, 091502 [arXiv:1305.5333 [hep-ex]].

M. Ablikim *et al.* [BESIII Collaboration], Phys. Rev. Lett. **110** (2013) 252001 [arXiv:1303.5949 [hep-ex]].

M. Bhatti, M. Lara, and P. Bracken, “Periodic Solutions of the Duffing Equation”, *International Journal of Mathematics*, Vol. 2, 2008, no. 8, 365 - 372,